university of groningen

Cortical synchrony across cognitive processing stages:

Dynamics & coordinating mechanisms

PhD thesis

to obtain the degree of PhD at the
University of Groningen
on the authority of the
Rector Magnificus Prof. C. Wijmenga
and in accordance with
the decision by the College of Deans.

This thesis will be defended in public on

Friday 15th October 2021 at 11.00 hours

By

Oscar Portolés Marín

born on 7 September 1985
in Alcañiz, Spain

Supervisor
Prof. M. Cao

Co-supervisor
Dr. J.P. Borst
Dr. M.K. van Vugt

Assessment Committee
Prof. N.M. Maurits
Prof. B. Forstmann
Prof. G. Deco

To my family

Acknowledgments

The contributions of many people to this thesis should be credited, because otherwise I would not be writing these lines. First of all I would like to thank my Promoters for the time spent with me, their guidance, and their interest in developing my skills. Specially, I thank them for the facilities to reconcile my family with my work. At an individual level, I give thanks to Marieke van Vugt for her efforts to connect me with researchers that could help me. I would like to thank Ming Cao for improving my reasoning, argumentation, and communication skills, as well as for integrating me in a nice collaborative group, motivating us, and providing us with inspiring literature. Ultimately, I must express my gratitude to Jelmer Borst for supporting me in the worst moment when I considered dropping out of this PhD. I really appreciate the trust that he put on me, and the confidence that he gave me. Furthermore, I am grateful for his willingness to educate me, his disposition to learn, for counting on me for other projects, for making me feel at home, and for our nice discussions inside and outside of RUG among many other things. It was gratifying to work together.

Very important contributions to this thesis are due to the collaboration with Yuzhen Qin. I thank Yuzhen for his kindness, his work, his explanations, and all the fruitful discussions. Another important contribution came from Jonathan Hadida who had the right knowledge and the best personality to have insightful discussions, and to push the project forward. Furthermore, I am grateful to Joana Cabral and Mark Woolricht for connecting me with Jonathan, as well as for their advice and comments. Lastly, I thank Mauel Blesa for his help and his contributions.

I am very grateful to Elina Sietsema, Remco Wouts, and the Peregrine team for their professionality, readiness for helping, and kindness. All of them created the best conditions for working efficiently and without worries. From the times before this PhD, I want to thank Estefania Dominguez, Vincent Reid, and Montserrat Vallverdu for encouraging me to pursue a PhD. Among all the interesting and kind people that I met during my PhD, I am especially grateful for the friendship with my Paranymphs Faik and Yuri. They made me feel at home and gave me extra energy with many gratifying, fulfilling, and funny moments.

To conclude, I am most thankful to my partner Elli for supporting me in pursuing a PhD and coming with me to Groningen. I am very grateful for her help, her company, her comprehension, and all these days that she had to take extra duties because I needed more time. In addition, I would like to thank my daughters Maya and Estela for their loving and restorative smiles, the fast course on working efficiency, and the time to think and read while we were in parks, walking, or just looking through the window. Finally, I am grateful to my parents for all the sacrifices that they made for me, and their support.

Table of Contents

1 Introduction & Background....9

1.1 Introduction....10

1.2 Background....12

1.3 Thesis Outline....18

2 Characterizing synchrony patterns across cognitive task stages of associative recognition memory....25

2.1 Introduction....26

2.2 Materials and Methods....29

2.3 Results....37

2.4 Discussion....43

3 Modulations of local synchrony over time lead to resting-state functional connectivity in a parsimonious large-scale brain model....53

3.1 Introduction....54

3.2 Results....56

3.3 Discussion....65

3.4 Methods and Model....72

3.5 Supplementary Information....78

4 Thalamic bursts modulate cortical synchrony locally to switch between states of global functional connectivity in a cognitive task....93

4.1 Introduction....94

4.2 Results....95

4.3 Discussion....103

4.4 Methods....105

4.5 Supplementary Figures....113

5 *Conclusion & Outlook*....120

5.1 Conclusion....121

5.2 Outlook....124

Summary....130

1 Introduction & Background

1.1 Introduction

1.1.1 Fundamental Stages of Cognition

One assumption often found implicitly or explicitly in cognitive science is that information is processed in the brain in sequences of discrete stages that include the encoding of information, retrieval of memories, decision-making, and motor response. The first time that this view on information processing appeared dates back to the work of Donders in the XIX th century [1]. Donders developed a series of experiments in which a cognitive stage was isolated and quantified by its processing time. This isolation was done by comparing the response time of a baseline task with that of the baseline task plus another processing stage. For example, in one task the participants had to respond to whether a light was white or red by responding with their right or left hand, respectively. The response times (RT) of this task were compared with the RTs of a similar task in which participants had to withhold the response if there was a red light. This experiment led Donders to the conclusion that an experiment where the participant could use both hands for responding required a 154 ms process of selection and preparation of the correct hand.

By now the notion of sequential elementary cognitive stages has been extended to explain how the brain processes information (although these processes do not need to be strictly sequential, e.g., [2]). The assumptions underlying the idea that tasks consist of sequences of discrete cognitive stages have been thoroughly tested [3–5]. Elaborate mathematical models have been developed around the concept of discrete processing stages and their effect on RTs to explain, for example, decision making [6]. Moreover, cognitive architectures that provide a formal definition of these processing stages and their interactions are able to reproduce human behavior in complex cognitive tasks as well as the neural activation produced by each of these cognitive stages [7].

Although there is strong evidence for the sequential nature of information processing in the brain, a limited number of studies has measured the neural activity at each cognitive stage by itself. One reason is that the temporal resolution of fMRI is lower than the duration of cognitive stages. Therefore, fMRI cannot measure single cognitive stages accurately, leaving only the possibility to use MEG and EEG studies. Another reason is the temporal variability of cognitive stages, as each cognitive stage has a different duration and on top of that, a given stage also varies in duration across experimental trials of the same task.

In this thesis, I will use electroencephalography (EEG) and magnetoencephalography (MEG) recordings to better characterize processing stages as the M/EEG has the temporal resolution required to capture the neural activity of cognitive stages.

1.1.2 Transition between cognitive stages

If information is processed in the brain in discrete sequences of fundamental cognitive stages, there should be mechanisms for selecting the next cognitive stage and for recruiting the neural elements that will perform the operations associated with the desired cognitive function. The selection of a cognitive stage is thought to occur in the basal ganglia, a brain structure that is known to be able to learn the utility of triggering a particular cognitive stage given the informational state of the cortex. The current informational state of the cortex is compared by the basal ganglia to previous states to assess the utility of starting a particular cognitive stage. When a cognitive stage is selected, a signal from the basal ganglia is sent to the thalamus. Then the thalamus modulates cortical activity in such a way that the computations associated with the chosen cognitive stage can be performed [8–15].

Although there is extensive literature around how the basal ganglia learn and compute the utility of a cognitive stage [8,16,17], as well as how the selection for a cognitive stage is made[9–11], little is known about how the thalamus modulates cortical activity to actually start the selected stage. Challenges similar to those encountered in the measurement of the neural activity of cognitive stages are found in measuring the transitions between stages. One limitation is the the uncertainty in the temporal location of the transition between stages. This uncertainty results from the large temporal variability of cognitive stages within a trial, and across trials and subjects [5,18,19]. In addition, the thalamus is located underneath the cortex which hinders the measurement of thalamic activity non-invasively. M/EEG have limited possibilities for recording deep sources, and, even if that is possible, separating cortical and subcortical activity is an as-of-yet unsolved problem [20]. fMRI does not provide high enough temporal resolution. Invasive recordings of thalamic and cortical activities are scarce and limited to only a few locations determined by medical rather than scientific needs. As a result, most recordings of thalamic and cortical activities come from animal studies, but they are also limited to a few locations.

In this thesis, I made use of a machine-learning method to identify the onset of cognitive stages in M/EEG signals, and then characterize the patterns of M/EEG activity associated with each cognitive stage. Then, I developed a generative model of large-scale whole-brain activity (GWBM) to explain these findings by simulating cortical and thalamocortical activity, which can shed light on how the thalamus modulates cortical activity to trigger a new cognitive stage. The model unifies whole-brain neural dynamics, anatomy, and thalamic modulations of cortical activity to explain the patterns of neural activity of each cognitive stage that were previously observed. The next sections present background information about measurement of M/EEG data, the identification of cognitive stages in M/EEG data, and generative large-scale whole-brain activity models.

1.2 Background

1.2.1 Electroencephalography and Magnetoencephalography as measurements of neural activity

Electroencephalography (EEG) and magnetoencephalography (MEG) are two technologies to measure the macroscopic neural activity in the cortex non-invasively and with high temporal resolution. Macroscopic neural activity refers to the aggregated activity of ensembles of millions of adjacent neurons firing simultaneously. Active neurons in the ensemble produce electrical activity in the form of trans-membrane currents and membrane potentials. Both contribute to an extracellular electric field that can be measurable on the scalp as an electric potential or magnetic field by EEG or MEG, respectively. The strength of the observable electric potential depends on the alignment of neurons, as well as the temporal synchrony of the dipole moments generated by the extracellular fields. The neurons that contribute the most to EEG and MEG recordings are parallel to each other and orthogonal or parallel to the surface, respectively. Therefore, the strength of the electric potential in the ensemble is proportional to the number of synchronized dipole moments. In other words, the more neurons synchronize their firing, the higher the resulting amplitudes of EEG and MEG measurements [21,22].

Although EEG and MEG have the temporal resolution required to measure the neural activity of brief (i.e., < 100 ms) cognitive stages, the temporal variability of cognitive stages has hampered the analysis of their neural activity. The different cognitive stages involved in a task can have an duration from less than 100 ms to more than 500 ms [11]. Moreover, the duration of a given stage also varies across trials of the same task and across subjects. The temporal variability of cognitive stages prevents knowing the time of a transition between two stages and therefore parsing the M/EEG signals of a task into a sequence of cognitive stages. For example, the first stage can last 80 ms in one trial and 150 ms in the next trial, while the second stage might last 90 ms in the first trial 70 ms in the next trial.

Moreover, the activity recorded by M/EEG consists of a mixture of task-related and non-task-related activity as well as biological and external noise [23]. To unmask patterns of task-related activity, M/EEG signals are usually time-locked to time points common to all trials in the experiment. These reference points are typically experimental events located either at the onset of a stimulus, or at the responses of the participants. The reference points serve to align all trials such that patterns of neural activity common to all trials stand out against non-task-related activity and noise. However, as a metric of a task-related activity moves away from the reference point, this metric becomes blurred as task-related activity cannot be aligned due to the temporal variability of cognitive stages as explained in the previous paragraph.

Figure 1 shows an example of how such a blurring of task-related activity occurs with the help of synthetic data. The measurement of activity in the example is an *event-related potential (ERP)* [23,24], the most widely used measure of neural activity. To obtain an ERP, first, all trials are time-locked to the onset of the stimulus (time *zero* in the panels), and then the average across trials is computed. The left column in Figure 1 shows a subset of artificially generated EEG trials (blue signals) that contain traces reflecting task-related activity (orange signals), and traces reflecting noise plus non-task-related activity (the activity in the blue signal that is not explained by the orange signal). Like in real EEG trials, noise and non-task-related activity obscure events of task-related activity that occur at different times. The middle column shows ERPs (blue signals) computed with 5, 20, 50, 100, and 200 synthetic EEG trials like those in the left column. The more trials are used to compute the ERP, the more the ERPs resemble the averaged task-related activity (orange signal). However, averaged task-related activity becomes less and less representative of the true task-related activity as the number of EEG trials increases and the events of task-related activity are more distant from the onset of the trial. Events of task-related activity located far away from the onset of the trial merge into broad peaks and single events of task-related activity become indistinguishable. The task-related activity in this example signifies the onset of cognitive stages. Therefore, the onset of a cognitive stage is not decipherable from the ERPs or the EEG trials, so a trial cannot be easily parsed into cognitive stages.

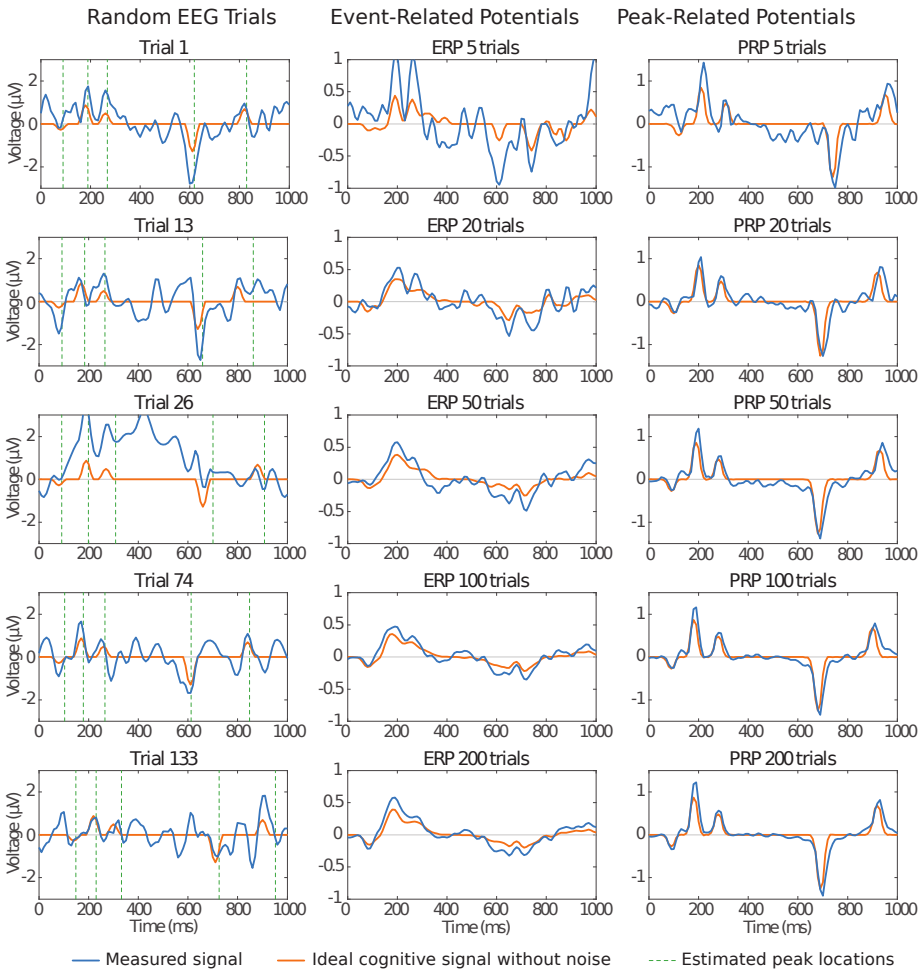

Figure 1. *Left:* Simulated task-related activity and non-task-related activity. *Center:* Event-related potentials, ERPs. *Right:* Event-related potentials time-locked to the onset of cognitive stages as estimated by the HSMM-MVPA. Reprinted with permission from [25]

To overcome this problem, in this thesis I applied a recent machine-learning method – to be explained in more detail in the next section – that aims at finding the transition between cognitive stages on a trial-by-trial basis from observable changes in the neural signals that characterize these transitions. Then, the transitions between the stages sets the time-locking points for various metrics of neural activity across trials. As a result of this procedure, these metrics will not be blurred by the temporal variability of cognitive stages, and task-related activity can be unmasked along each cognitive stage.

While the machine learning method was applied to broadband M/EEG signals, task-related metrics were applied to narrow-band M/EEG signals. The M/EEG signals can be decomposed into narrow-band frequencies that are related to neural functions [21]. The narrow-band signals are characterized by their frequency band, phase, and amplitude. The most relevant frequency bands for cognition are defined roughly in the ranges: *delta* (from 0.2 to 4 Hz), *theta* (from 4 to 8 Hz), *alpha* and *mu* (from 8 to 15 Hz), *beta* (from 15 to 30 Hz), and *gamma* (from 30 Hz and above) oscillations [21,23]. Single narrow-band metrics of particular interest to this thesis are local modulations of amplitude or power known as an event-related synchronization or desynchronization, local inter-trial phase coherence, as well as statistical relationships of amplitude and phase between pairs of locations known as functional connectivity. These metrics allow for characterizing the amount of neural synchrony with a brain region, the consistency of the timing of local activity as well as timing of the synchrony between pairs of brain regions. Moreover, changes of local synchrony are related to changes in synchrony between brain regions [26]. In this thesis, these metrics have been applied to several frequency bands to characterize the evolution of neural activity along the cognitive stages of a task as well as during the resting state. Resting sates reflects ongoing neural activity that is not modulated by external stimuli.

1.2.2 Finding cognitive stages in EEG and MEG

The first attempts at identifying cognitive stages in M/EEG signals used machine learning methods to search trial-by-trial for stable patterns of activity throughout cognitive stages [27,28]. This approach is related to research on M/EEG *microstates* and their connection to cognitive processes [29]. Microstates are a limited set of quasi-stable cortex-wide topological patterns that last for periods of 80 to 120 milliseconds, although their computation neglects the temporal variability of cognitive stages across trials. Another, more recent, approach that will be used in this thesis aims at finding the transition between stages instead of stable patterns of activity throughout the stages.

This method combines a hidden semi-Markov model with multivariate pattern analysis (HSMM-MVPA) to find the transitions between cognitive stages on a trial-by-trial basis [30].The HSMM-MVPA method has two components. One component defines the sequence of cognitive stages in the task. Each stage in this sequence is modeled by a parsimonious representation of the M/EEG signal and a probability distribution that constrain the duration of the stage. The second component is the machine learning method that fits the parsimonious model of the M/EEG signals to M/EEG data compressed by means of principal component analysis in order to identify the onset of cognitive stages on a trial-by-trial basis. The fitting is accomplished by the expectation maximization algorithm for hidden semi-Markov models [31].

The parsimonious representation of the M/EEG signals was derived by postulating a linking assumption between the mechanisms that modulate neural activity at cognitive stages and the resulting M/EEG signals. The parsimonious model of M/EEG signals consists of 50-millisecond long *bumps* that model the onset of cognitive stages, and *flat* intervals with zero mean amplitude that span from the end of the bumps to the end of each cognitive stage. The bump of one cognitive stage is assumed to have the same cortex-wide topology in all trials, while the duration of a cognitive stage is assumed to follow a gamma probability distribution. All stages in a sequence are assumed to follow this bump-flat structure except for the first stage which does not have a bump. To find the onset of cognitive stages, the expectation maximization algorithm of HSMMs estimates the topology of bumps, the temporal location of the bumps, and the parameters of the gamma distributions. Figure 2 depicts this parsimonious model of the signals in a task consisting of six cognitive stages – 5 bumps and six flats that were estimated with the HSMM algorithm. The results of fitting the HSMM-MVPA to the synthetic data in Figure 1 are depicted with green dashed lines in the first column of Figure 1. Each green dashed line represents the estimated location of a bump – the onset of a cognitive stage (orange line). Once the onset of cognitive stages is known, it can be used to time-lock across trials metrics neural activity. For example, the right column in Figure 1 shows ERPs time locked to the onset of cognitive stages with the interval between onset either compressed or expanded to mean duration of the stage. In this way, non-task-related activity is removed and only the waveform of the onsets remains.

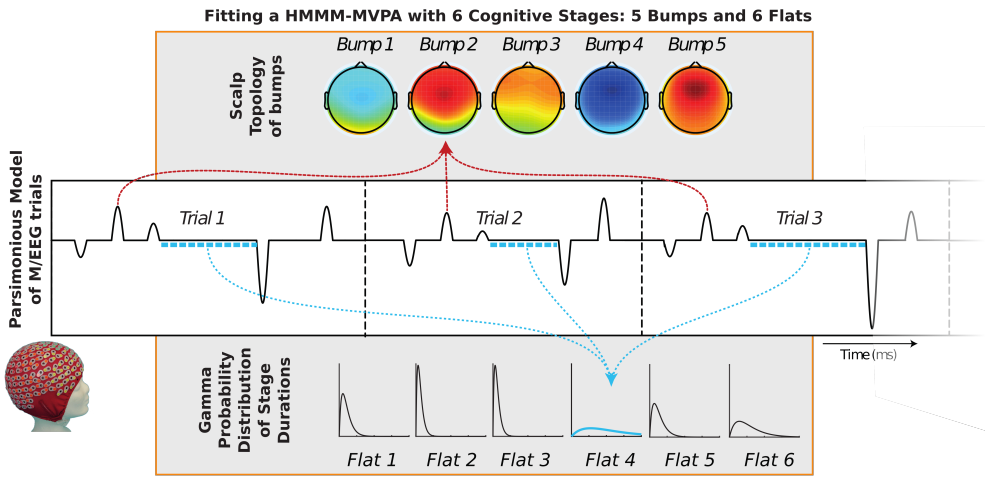

***Figure 2**, Parsimonious model of single trials (center). Estimated scalp topologies at the onset of cognitive stages (top). Estimated probability distribution of stage durations (right). Modified with permission from [32].*

1.2.3 Generative Biophysical Mode of Large-Scale Neural Activity

To understand the mechanisms that generate the patterns of neural activity recorded during the cognitive stages, as well as the neural mechanisms that modulate cortical activity to effectuate switches between cognitive stages, a generative biophysical model of large-scale whole-brain neural activity (GWBM) was used [33]. GWBMs unify the electrophysiological properties of elementary dynamical units ranging from single neurons to ensembles of neurons, to brain regions. These models also incorporate the anatomical interactions among these dynamical units and use all together to explain large-scale patterns in whole-brain neuroimaging data. Moreover, GWBMs allow for evaluating how changes to the dynamics or the interactions between units affect the neuroimaging data produced.

Currently GWBMs that include all neurons and synapses in the brain are not only computationally unfeasible but also very difficult to interpret. Therefore, GWBMs pool adjacent neurons into an ensemble – a dynamical unit – and use different mathematical tools to describe the aggregated dynamics in the pool of neurons with macroscopic variables. Each dynamical unit is represented as a node in a network. The links of this network are supposed to be large bundles of myelinated neural fibers that connect regions of the brain. The density and distance of these anatomical links are computed by tractography from diffusion magnetic resonance imaging. Therefore, the macroscopic dynamics of an ensemble of neurons – a nodal dynamical unit – depend on the properties of the same ensemble as well as the density of coupling with other ensembles and the time-delays caused by the spike-propagation velocity through the neural fibers. Previously, such biophysical networks have been used to explain the statistical relationships that appear between brain regions in neuroimaging recordings (i.e. functional connectivity) during the resting state [34,35].

Although GWBMs are a valuable tool in neuroscience and medicine [36], they have until now not been applied to cognitive tasks. One of the reasons for this omission is related to the complexity and computational cost of GWBMs. On the one hand, biologically detailed GWBMs have complex dynamics and many parameters. While phenomenological GWBMs (non-biologically informed) have simpler dynamics and fewer parameters, their interpretation in biological terms is less clear. Both families of GWBMs require a large amount of computational resources which hinders exploring many parameterizations of the models. To reduce the number of free parameters, most GWBM assume that all dynamical units have identical and constant parameters. However, this assumption cannot be extended to modeling a sequence of cognitive stages because the literature suggests that the local properties of the dynamical units are modulated by the thalamus at the onset of each cognitive stage.

Another reason that hinders the use of GWBMs in modeling cognitive tasks is related to the practice of reducing the activity in an ensemble of neurons to macroscopic variables. The

macroscopic variables fail to capture modulation of neural synchrony within the ensemble, and it is precisely these modulations of local synchrony that happen at the moment of significant cognitive events (thereby resulting in event-related synchronization or desynchronization) [37,38]. Moreover, these local modulations in synchrony are also related to changes in functional connectivity patterns[26].

In this thesis, I used a GWBM to bridge the gap between M/EEG recordings and the neural mechanisms that generate these observations – and ultimately behavior. To remedy the limitations of GWBMs outlined above, a parsimonious GWBM was developed in this thesis and applied to simulate resting-state and task-related M/EEG data. This GWBM simulates a macroscopic variable of aggregated neural activity with the same temporal and spatial resolution as M/EEG signals; the dynamics of the macroscopic variable follow a relatively simple equation to minimize the computational cost of the model; the regional dynamics depend mostly in a single parameter to ease the exploration of parameters; the macroscopic variable is postulated in terms of regional and between regions neural synchrony; and this variable is able to capture the modulations of local synchrony that are observed on cognitive tasks. Because most GWBMs to date have only been used to simulate resting state activity, the GWBM is applied first to resting state data. Once the performance and benefits of the model had been evaluated following the state-of-the-art approach, thalamic inputs were added to the onset of cognitive stages to simulate task-related MEG data.

1.3 Thesis Outline

1.3.1 Contributions

As mentioned in the previous section, the aim of this thesis is to shed light on how macroscopic neural activity is coordinated throughout the course of a cognitive task. Particularly, it seeks to uncover the neural activity pattens related to each of the fundamental cognitive stages of a task and the mechanisms that coordinate the transitions between consecutive stages. The **second chapter** of the thesis demonstrates that each cognitive stage in an associative memory recognition task is related to a specific pattern of local activity and functional connectivity observed in various EEG frequency bands. This finding was predicted by theories of cognition, but it had not been measured yet due to the technical limitations of M/EEG outlined in the introduction. Given these results, the thesis proceeds to evaluate the mechanism that generates the neural of activity of these observations.

The **third chapter** develops and validates a parsimonious GWBM, and demonstrates that it is able to simulate neural activity patterns during a cognitive task. The GWBM is validated with resting-state data – the current application field of GWBMs. This GWBM indicates

that there is a relationship between modulations of local synchrony – which cannot be captured by state-of-the-art GWBMs and are fundamental to cognitive processes – and time-resolved resting-state functional connectivity. Moreover, this chapter explores the impact of allowing brain regions to have different tendencies to synchronize locally.

The results of the first and second chapters provide the foundation to articulate the mechanism that drive the patterns of neural activity along with the cognitive stages of a task. The **fourth chapter** extends the results of Chapter 1 by showing with high temporal resolution that the pattern of neural activity associated with a cognitive function starts right at the onset of the stage and lasts throughout the cognitive stage. Therefore, neural activity is modulated right at the onset of cognitive stages as cognitive theories had hypothesized. Next, the GWBM developed in Chapter 2 is adapted to simulate these observations. The GWBM in Chapter 4 includes a parsimonious representation of the mechanism that the thalamus – driven by the basal ganglia – is thought to use to modulate neural activity at the onset of cognitive stages. This mechanism is derived from the literature on invasive recordings of thalamic and cortical activity. Such a parsimonious representation allows for the optimization of all parameters in the model in a relatively short period of time. This GWBM shows that thalamic bursts of activity targeted to increase or decrease the synaptic connectivity strength briefly at the onset of cognitive stages modulate cortical amplitude locally which, in turn, induces a change in functional connectivity lasting throughout the cognitive stage. The simulated neural activity is in agreement with the measurements of neural activity along the cognitive stages. Furthermore, the GWBM is use to explain which cortical regions are the most important for switching between different patterns of neural activity at the onset of cognitive stages.

1.3.2 List of Publications

Chapter Two
Portoles, O., Borst, J.P., & Van Vugt, M.. "*Characterizing synchrony patterns across cognitive task stages of associative recognition memory*". *European Journal of Neuroscience 48*, 2018.

Chapter Three
Portoles, O., Qin, Y., Hadida, J., Woolrich, M., Cao, M., van Vugt, M., "*Modulations of local synchrony over time lead to resting-state functional connectivity in a parsimonious large-scale brain model*", *Under revision*, doi: https://doi.org/10.1101/2021.01.20.427443

Chapter Four
Portoles, O., Van Vugt, M. Cao, Borst, J.P. "*How the Brain Switches between Cognitive Processes: modulations of local coordination lead to switches in cortico-cortical coordination*", *Submitted*

Other contributed publications related to the thesis
van Maanen, L., Portoles, O., Borst, J.P., "*The discovery and interpretation of hidden evidence accumulation stages*", Computational Brain & Behavior, I*n press*

Qin, Y., Kawano, Y., Portoles, O., Cao, M., "*Partial phase cohesiveness in networks of networks of Kuramoto oscillators*", IEEE Transactions on Automatic Control, 2021

References

1. Donders FC. On the speed of mental processes. Acta Psychol (Ams). 1969;30: 412–431. doi:10.1016/0001-6918(69)90065-1
2. Sackur J, Dehaene S. The cognitive architecture for chaining of two mental operations. Cognition. 2009;111: 187–211. doi:10.1016/j.cognition.2009.01.010
3. Ilan AB, Miller J. A violation of pure insertion: mental rotation and choice reaction time. J Exp Psychol Hum Percept Perform. 1994;20: 520–536. doi:10.1037//0096-1523.20.3.520
4. Ulrich R, Mattes S, Miller J. Donders's assumption of pure insertion: an evaluation on the basis of response dynamics. Acta Psychologica. 1999;102: 43–76. doi:10.1016/S0001-6918(99)00019-0
5. Sternberg S. The discovery of processing stages: Extensions of Donders' method. Acta Psychologica. 1969;30: 276–315. doi:10.1016/0001-6918(69)90055-9
6. Ratcliff R, Smith PL, Brown SD, McKoon G. Diffusion Decision Model: Current Issues and History. Trends Cogn Sci. 2016;20: 260–281. doi:10.1016/j.tics.2016.01.007
7. Anderson, J.R. B J P, Taatgen. Using the ACT-R Cognitive Architecture in combination with fMRI data. B. U. Forstmann, E.-J. Wagenmakers. An Introduction to Model-Based Cognitive Neuroscience. B. U. Forstmann, E.-J. Wagenmakers. New York: Springer:;
8. Ceballos JM, Stocco A, Prat CS. The Role of Basal Ganglia Reinforcement Learning in Lexical Ambiguity Resolution. Topics in Cognitive Science. 2020;12: 402–416. doi:https://doi.org/10.1111/tops.12488
9. Stocco A, Lebiere C, Anderson JR. Conditional routing of information to the cortex: A model of the basal ganglia's role in cognitive coordination. Psychol Rev. 2010;117: 541–574. doi:10.1037/a0019077
10. Stocco A. A Biologically Plausible Action Selection System for Cognitive Architectures: Implications of Basal Ganglia Anatomy for Learning and Decision-Making Models. Cogn Sci. 2018;42: 457–490. doi:10.1111/cogs.12506
11. Anderson JR. How can the human mind occur in the physical universe? Oxford ; New York: Oxford University Press; 2007.
12. Saalmann YB, Pinsk MA, Wang L, Li X, Kastner S. The Pulvinar Regulates Information Transmission Between Cortical Areas Based on Attention Demands. Science. 2012;337: 753–756. doi:10.1126/science.1223082
13. Redgrave P, Prescott TJ, Gurney K. The basal ganglia: a vertebrate solution to the selection problem? Neuroscience. 1999;89: 1009–1023. doi:10.1016/s0306-4522(98)00319-4
14. Malekmohammadi M, Elias WJ, Pouratian N. Human Thalamus Regulates Cortical Activity via Spatially Specific and Structurally Constrained Phase-Amplitude Coupling. : 11.
15. Stewart TC, Bekolay T, Eliasmith C. Learning to Select Actions with Spiking Neurons in the Basal Ganglia. Front Neurosci. 2012;6. doi:10.3389/fnins.2012.00002
16. Gurney K, Prescott TJ, Redgrave P. A computational model of action selection in the basal ganglia. I. A new functional anatomy. Biol Cybern. 2001;84: 401–410. doi:10.1007/PL00007984
17. Joel D, Niv Y, Ruppin E. Actor-critic models of the basal ganglia: new anatomical and computational perspectives. Neural Netw. 2002;15: 535–547. doi:10.1016/s0893-6080(02)00047-3
18. Ramchurn A, de Fockert JW, Mason L, Darling S, Bunce D. Intraindividual reaction time variability affects P300 amplitude rather than latency. Front Hum Neurosci. 2014;8. doi:10.3389/fnhum.2014.00557
19. Van Zandt T, Ratcliff R. Statistical mimicking of reaction time data: Single-process models, parameter variability, and mixtures. Psychonomic Bulletin & Review. 1995;2: 20–54. doi:10.3758/BF03214411
20. Krishnaswamy P, Obregon-Henao G, Ahveninen J, Khan S, Babadi B, Iglesias JE. Sparsity enables estimation of both subcortical and cortical activity from MEG and EEG. : 10.
21. Lopes da Silva F. EEG and MEG: Relevance to Neuroscience. Neuron. 2013;80: 1112–1128. doi:10.1016/j.neuron.2013.10.017
22. Buzsáki G, Anastassiou CA, Koch C. The origin of extracellular fields and currents — EEG, ECoG, LFP and spikes. Nat Rev Neurosci. 2012;13: 407–420. doi:10.1038/nrn3241
23. Pablo Laguna LS. Bioelectrical Signal Processing in Cardiac and Neurological Applications. Elsevier; 2005. doi:10.1016/B978-0-12-437552-9.X5000-4
24. Luck SJ. An Introduction to the Event-Related Potential Technique. MIT Press; 2014.

25. Borst J, Anderson JR. Discovering Cognitive Stages in M/EEG Data to inform Cognitive Models. 2nd ed. B Turner (Eds), An Introduction to Model-Based Cognitive Neuroscience. 2nd ed. Springer: New York;
26. Tewarie P, Hunt BAE, O'Neill GC, Byrne A, Aquino K, Bauer M, et al. Relationships Between Neuronal Oscillatory Amplitude and Dynamic Functional Connectivity. Cerebral Cortex. 2019;29: 2668–2681. doi:10.1093/cercor/bhy136
27. Borst JP, Anderson JR. The discovery of processing stages: Analyzing EEG data with hidden semi-Markov models. NeuroImage. 2015;108: 60–73. doi:10.1016/j.neuroimage.2014.12.029
28. Borst JP, Schneider DW, Walsh MM, Anderson JR. Stages of processing in associative recognition: evidence from behavior, EEG, and classification. J Cogn Neurosci. 2013;25: 2151–2166. doi:10.1162/jocn_a_00457
29. Pascual-Marqui RD, Michel CM, Lehmann D. Segmentation of brain electrical activity into microstates: model estimation and validation. IEEE Trans Biomed Eng. 1995;42: 658–665. doi:10.1109/10.391164
30. Anderson JR, Zhang Q, Borst JP, Walsh MM. The discovery of processing stages: Extension of Sternberg's method. Psychol Rev. 2016;123: 481–509. doi:10.1037/rev0000030
31. Yu S-Z. Hidden semi-Markov models. Artificial Intelligence. 2010; 29.
32. Berberyan HS, van Maanen L, van Rijn H, Borst J. EEG-based Identification of Evidence Accumulation Stages in Decision-Making. J Cogn Neurosci. 2020;33: 510–527. doi:10.1162/jocn_a_01663
33. Breakspear M. Dynamic models of large-scale brain activity. Nat Neurosci. 2017;20: 340–352. doi:10.1038/nn.4497
34. Cabral J, Kringelbach ML, Deco G. Functional connectivity dynamically evolves on multiple time-scales over a static structural connectome: Models and mechanisms. NeuroImage. 2017;160: 84–96. doi:10.1016/j.neuroimage.2017.03.045
35. Deco G, Jirsa V, McIntosh AR, Sporns O, Kötter R. Key role of coupling, delay, and noise in resting brain fluctuations. PNAS. 2009;106: 10302–10307. doi:10.1073/pnas.0901831106
36. Jirsa VK, Proix T, Perdikis D, Woodman MM, Wang H, Gonzalez-Martinez J, et al. The Virtual Epileptic Patient: Individualized whole-brain models of epilepsy spread. Neuroimage. 2017;145: 377–388. doi:10.1016/j.neuroimage.2016.04.049
37. Byrne Á, Brookes MJ, Coombes S. A mean field model for movement induced changes in the beta rhythm. J Comput Neurosci. 2017;43: 143–158. doi:10.1007/s10827-017-0655-7
38. Coombes S, Byrne Á. Next generation neural mass models. arXiv:160706251 [q-bio]. 2016 [cited 9 Jul 2019]. Available: http://arxiv.org/abs/1607.06251

2 Characterizing synchrony patterns across cognitive task stages of associative recognition memory

Numerous studies seek to understand the role of oscillatory synchronization in cognition. This problem is particularly challenging in the context of complex cognitive behavior, which consists of a sequence of processing steps with uncertain duration. In this study, we analyzed oscillatory connectivity measures in time windows that previous computational models had associated with a specific sequence of processing steps in an associative memory recognition task (visual encoding, familiarity, memory retrieval, decision making, and motor response). The timing of these processing steps was estimated on a single-trial basis with a novel hidden semi-Markov model multivariate pattern analysis (HSMM-MVPA) method. We show that different processing stages are associated with specific patterns of oscillatory connectivity. Visual encoding is characterized by a dense network connecting frontal, posterior, and temporal areas as well as frontal and occipital phase locking in the 4-9Hz theta band. Familiarity is associated with frontal phase locking in the 9-14Hz alpha band. Decision-making is associated with frontal, and temporo-central interhemispheric connections in the alpha band. During decision making, a second network in the theta band that connects left-temporal, central, and occipital areas bears similarity to the neural signature for preparing a motor response. A similar theta band network is also present during the motor response, with additionally alpha band connectivity between right-temporal and posterior areas. This demonstrates, that the processing stages discovered with the HSMM-MVPA method are indeed linked to distinct synchronization patterns, leading to a closer understanding of the functional role of oscillations in cognition.[1]

1 Published in Portoles, O., Borst, J.P., & Van Vugt, M.. "*Characterizing synchrony patterns across cognitive task stages of associative recognition memory*". *European Journal of Neuroscience 48*, 2018.

2.1 Introduction

Understanding the role of neural oscillations in cognition is a topic attracting growing interest. Neural oscillations are thought to provide a mechanism for the coordination and communication between different brain areas [1,2], which is required for controlled cognition. In addition, oscillations are thought to help to create synchronized time windows for neural computations in functionally specialized brain areas [3,4]. In humans, neural oscillations can be measured non-invasively with electroencephalography (EEG) and magnetoencephalography (MEG). EEG oscillations are mainly characterized in terms of mean power, phase locking across trials, and phase synchrony between pairs of electrodes – we will refer to the latter as connectivity in this paper.

Connectivity analyses are often performed across-trials on a sample-by-sample basis. This is problematic because across-trials measurements (e.g., ERPs, phase locking, phase connectivity) are very sensitive to temporal jitter in the onset of the relevant cognitive events. Trials can typically only be reliably time-locked to either the onsets of the trials or to the response to the stimulus. Consequently, examining time-locked patterns of activity has given us valuable information about cognitive processes around the onset of a trial such as attention or visual perception (e.g., [5]), or the processes involved in generating decisions (e.g., [6]). However, the duration of cognitive processes varies between trials and subjects, which imply that cognitive processes further away from trial onset or response (e.g., memory retrieval) are harder to analyze. If it were possible to estimate the onset of such cognitive processes we could time-lock the data to these onsets and thereby minimize the impact of temporal jitter.

There have been various approaches to decompose the continuous EEG time series into a series of quasi-stable stages. For example, [7] decomposes the EEG into “microstates” with durations of 80 to 120 milliseconds, and some of these microstates have been linked to global mental states such as “abstract thought” and “visual imagery”. Others have used hidden Markov models (HMMs) to identify stable states purely on the basis of the EEG signal during a resting state, not related to a specific cognitive task [8,9]. They showed that the different states had specific connectivity patterns and spectral content, but did not link that to any cognitive process.

Anderson et al. (2016) [10] merged a more detailed understanding of cognitive stages, or processes, with hidden semi-Markov models. Specifically, they proposed a method that identifies the onset of cognitive task stages. Their method combines multivariate pattern analysis with hidden semi-Markov models (HSMM-MVPA) to identify the onset of cognitive stages in EEG data on a trial-by-trial basis by looking for either positive or negative deflections in the EEG signal that signify the onset of each stage. Thus, this allows for parsing each trial into time windows corresponding to specific cognitive stages (e.g.,

visual processing, memory retrieval). Time windows with identical cognitive stages can be time-locked together across trials, such that temporal jitter between trials and subjects is minimized. By examining the connectivity networks in each time window, one can then link that window's cognitive operation to a pattern of synchrony, and thereby improve our understanding of the functional role of connectivity networks in cognition.

In this paper, we demonstrate how the HSMM-MVPA method can be used to relate the cognitive stages of an associative recognition memory task identified in a cognitive model of this task to distinct phase connectivity networks. Next, we introduce the HSMM-MVPA method followed by a focused review of previous literature on connectivity networks associated with cognitive functions, and an outline of our hypothesis.

2.1.1 The HSMM-MVPA method

The HSMM-MVPA method relies on the assumption that onsets of cognitive stages produce localized phasic neuronal activity which adds to the ongoing neural oscillations. This assumption is based on the classical theory of how EEG evoked responses are generated [11]. This phasic neural activity produces a deflection in the EEG if the concentration of neural activity in a brain region is large enough to stand out from the background neural activity. This theory is often contrasted with a second theory that states that the onset of cognitive stages produce a phase reset at a certain frequency band instead of an evoked response [12,13]. Nevertheless, simulation studies have shown that both theories produce similar deflections in the EEG signal [14,15].

Based on this idea, Anderson et al. (2016) [10,16] developed the HSMM-MVPA method for EEG. In contrast to traditional evoked response studies, in which trials are averaged to obtain evoked brain activity, the HSMM-MVPA method uses the topographical properties of all trials and subjects in order to estimate the parameters of a hidden process underlying all trials. This hidden process is supposed to reflect cognitive processing, and is characterized as a succession of deflections in the EEG (either positive or negative), which are separated in time and spatially localized.

HSMM-MVPA uses the expectation maximization algorithm of HSMM [17] to find the most likely locations and amplitudes of the deflections on each trial. The search space is constrained by a few parameters defined beforehand, such as the number of cognitive stages in a trial. In addition to estimating the underlying general process, the HSMM-MVPA produces for each trial a probability distribution for the location of the onset of each cognitive stage.

Anderson et al. (2016) [10] evaluated the HSMM-MVPA method on EEG data from an associative recognition memory task, a Sternberg working memory task, as well as

synthetic EEG data. Importantly, each of the HSMM-MVPA stages was related to specific cognitive functions by means of cognitive models of the tasks for associative recognition memory [18–20], and for the Sternberg working memory task [21–24]. Anderson et al. (2016) [10] observed good agreement between the number of cognitive stages in the cognitive models and the results of their respective HSMM-MVPA analyses. In addition, the duration of the discovered cognitive stages of both tasks varied with experimental condition in the ways predicted by the cognitive models (e.g., a discovered recollection stage was longer for items that were harder to retrieve from memory according to the model).

Although the HSMM-MVPA states were related to specific cognitive functions, the authors did not examine whether they were associated with distinct connectivity networks (of the type that was examined by [9]. In this study, our aim is to examine whether the HSMM-MVPA stages are associated with consistent connectivity patterns, and to assess whether the observed connectivity patterns are consistent with functions ascribed to these networks in the literature.

2.1.2 Cognitive functions associated with specific connectivity networks

The frequency bands that are most relevant to associative recognition memory are 4-9Hz theta and 9-14Hz alpha oscillations. The literature on the functions of alpha and theta connectivity networks in cognition is relatively varied. Fronto-parietal theta synchrony has been associated with learning novel finger movements [25], subtraction [26], maintenance of memories [25,27], as well as memory span [28] and executive functions more generally [29,30]; cf. the fronto-parietal network in fMRI, [31–34].

Longer-range fronto-posterior connectivity in the theta band has been more specifically related to memory retention [29,35], and successful memory encoding [36,37]. In addition, fronto-posterior connectivity after a person has made their response has been associated with adjusting cognitive control [38]. Fronto-parietal-occipital connectivity has been associated with cognitive ability across participants in tasks ranging from semantic grouping to mental rotation [39]. Connectivity of temporal regions with frontal cortex has been associated with binding information between stimulus modalities while connectivity with occipital regions has been related to maintaining relational information[27].

The literature on the role of alpha connectivity in cognition is also quite heterogeneous. Fronto-parietal alpha oscillations have been associated with sustained attention [40], but also with working memory load [3] and with the recognition of words [41]. Even longer-range anterior-posterior alpha connectivity has been associated with manipulating information [42], dealing with conflicting information, and semantic encoding [42]. The gradual construction of a story has also been associated with fronto-posterior alpha

connectivity, but in that case connectivity was restricted to the left hemisphere [43]. In the alpha band, interhemispheric coherence has been associated to functions such as recognition memory [41], and object recognition [44]. When interhemispheric connectivity occurs over sensory-motor areas, it has been well established to play a role in the successful execution of sensory-motor tasks [45–47].

From the amalgamate of findings discussed above, it is clear that a comprehensive theory of the role of oscillatory connectivity in cognition is still lacking. Previous work suggests that the associative recognition memory task consists of six cognitive stages [10,16]. The first and second stages reflect visual perception and encoding the words on the screen. Our literature review suggests that this may be associated with fronto-posterior theta connectivity [35,37]. The third stage was hypothesized to be a combination of encoding the second word and assessing the familiarity of the words, and the fourth stage is associated with memory retrieval. Both stages may manifest as fronto-posterior theta connectivity as well, although no scalp EEG studies have so far specifically focused on memory retrieval-related connectivity to our knowledge. In the fifth task stage, the perceived information from stage two is combined with retrieved information from stage four and this drives a decision-making process. This suggests that this stage may be associated with theta connectivity between fronto-temporal areas [48]. The last stage, stage six, is the response stage, which may be associated with interhemispheric connectivity in the alpha band over motor cortex [45,46].

2.2 Materials and Methods

We examined patterns of phase connectivity, phase locking, and oscillatory power during different events on the stages indicated by the HSMM-MVPA method of an associative recognition memory task. In this task, participants learn a set of 32 pairs of words, and subsequently are asked in a testing session whether a presented pair of words is identical to one of the studied word pairs. These data were collected and first reported in a study by Borst et al. (2013) [49].

2.2.1.1 Participants

Data from twenty subjects reported in the original study [49] were used in the current analysis. The group consisted of 11 women and 9 men, with ages ranging from 18 to 40 years and a mean age of 26 years. All subjects were right handed, and none of them reported a history of cognitive impairment. Written informed consent as approved by the Institutional Review Board at Carnegie Mellon University was obtained before the experiment.

2.2.1.2 Task procedure

A timeline of a trial during the testing session is shown in Figure 1. Each trial in the test period began with a fixation cross for a random time interval between 400 and 600 msec. Next, a probe pair of words appeared on the center of the screen. Subjects were asked to press a key indicating whether they had learned the probe or not. All subjects responded with their right hand, and they were instructed to respond both quickly and accurately. An accuracy feedback indicator was shown for 1000 msec just after the subjects' responses. A blank screen followed for 500 msec, after which the next trial began. Each subject was presented with 416 trials with learned pairs of words, and 416 trials with re-paired pairs of words. Two manipulations in the original experiment – fan and word length – are irrelevant for this study, so they will be ignored. Additionally, in the original study subjects were presented with 208 trials with new pairs of words. Trials with new pairs were not included in our analyses. We refer the reader to the original paper for further details on the experimental procedure.

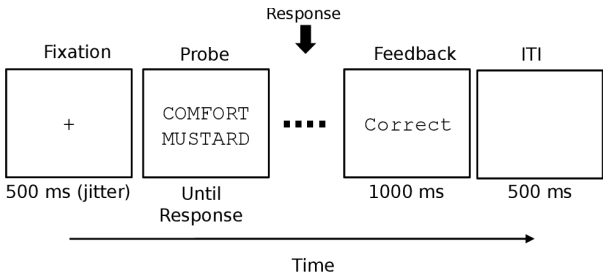

Figure 1*. Timeline of a trial during the test phase of the associative memory recognition task. ITI stands for inter-trial interval.*

2.2.1.3 EEG measurements

EEG measurements took place inside an electromagnetically shielded chamber. Test trials were presented on a CRT monitor situated at 60 cm from the subjects outside of the shielded chamber. EEG data was measured from 32 Ag-AgCl sintered electrodes (10 – 20 system). Reference electrodes were placed over the right and left mastoids. Bi-polar montages were used to record vertical and horizontal eye movements. Scalp EEG recordings were algebraically re-referenced to the average of both mastoid electrodes. All signals were sampled at 250 Hz with a band-pass filter between 0.1 to 70 Hz and amplified by a Neuroscan bioamplification system (Neuroscan, Inc., Sterling, USA). Electrode impedances were kept below 5 kΩ.

2.2.1.4 EEG pre-processing

The initial pre-processing steps were identical to the pre-processing carried out in Borst et al. (2013) [49]. First, visual inspection of EEG data was performed to remove artifacts. Next, EEG was decomposed into independent components with the infomax algorithm implemented in EEGLAB software [50]. Independent components were visually inspected, and those components identified as blinks were removed. Subsequent preprocessing steps were specific to our study. EEG was down-sampled to 100 Hz and band-pass filtered between 1 and 35 Hz. The bandpass filter was designed with the default parameters in the iirfilt plug-in for EEGLAB. The iirfilt plug-in creates by default a causal IIR Elliptic filter. The default settings designed an order ten low-pass filter with transition band of 1 Hz, and an order six high-pass filter with transition band of 0.3 Hz. The amplitude ripple at pass-band frequencies was lower than 0.0025 dB. The amplitude at stop-band frequencies was attenuated at least by a factor of 40 dB. The filter was passed twice in opposite directions to secure zero-phase shift. After band-pass filtering, linear trends were removed on a single-trial basis by fitting an straight line and subtracting it. We downsampled the data to 100 Hz to reduce the amount of data points, so the computation of the HSMM-MVPA was quicker. We filtered out frequencies below 1 Hz and de-trended singles trials to fulfill the assumption of the HSMM-MVPA that the time interval between the onsets of two consecutive cognitive stages has a mean amplitude of zero (see the next subsection for a further explanation). We observed that lower cut-off frequencies compromised this assumption and the output of the HSMM-MVPA. After removal of artefacts and filtering, incomplete trials due to artifact rejection as well as those with amplitudes outside the range between -80 μV to +80 μV were excluded. For the segmentation of EEG into cognitive stages, trials were bounded by stimulus onset and the response. Trials with incorrect responses were removed, as well as those with responses more than three standard deviations away from the mean response time per participant and condition. Following Borst et al. (2013) [49], any remaining trials with responses longer than 3000 msec were excluded. In total 8.25% trials were excluded from the analysis.

For the analysis of EEG oscillations, continuous EEG data were bandpass-filtered in theta, alpha, and beta frequency bands (i.e., θ: 4-9 Hz, α: 9-15 Hz, and β: 15-30 Hz). The filters were designed and applied with the plug-in iirfilt from EEGLAB with default parameters. The three filters have 1-Hz transition band at both cut-off frequencies .The theta band filter has order of seven for the low cut-off frequency and order of nine for the high cut-off frequency. Alpha and beta band filters have order nine and ten for the low cut-off and high cut-off frequencies respectively. These frequency-transformed data were segmented from 300 msec before stimulus onset to the stimulus response. A baseline period before stimulus onset was added to allow us to remove background activity from task activity in subsequent processing steps. EEG processing was done with EEGLAB software as well as custom-written MATLAB scripts.

2.2.1.5 Segmenting EEG into cognitive stages

The segmentation of EEG trials into cognitive stages was carried out by means of the HSMM-MVPA method proposed by Anderson et al. (2016) [10]. Before applying HSMM-MVPA a principal component analysis (PCA) was performed with a unique covariance matrix on the basis of the combined data from all subjects. The covariance matrices of each trial on each subject were averaged together to compute the principal components [51]. Because all subjects are included in the computation of the PCA, the principal components (PCs) match across subjects and a single model for all subjects can be created. Following Anderson et al. (2016) [10], the first ten PCs, which account for more than 95 percent of the variance in the data, were preserved for the HSMM-MVPA analysis. Each of these PCs in a trial was z-scored to ensure that each trial had a mean of zero and a variance of one.

The HSMM-MVPA finds the most likely partition of each trial into a certain number of cognitive stages given an underling model common to all trials. This underlying model is represented schematically in Figure 2. In this model, each cognitive stage is assumed to start with a 50-msec deflection either entirely positive or negative. This deflection is hypothesized by Anderson et al. (2016) [10] to reflect a burst of phasic neural activity at the onset of a cognitive event [11], as described in the Introduction. The amplitude of the deflection is estimated by the HSMM-MVPA. After each deflection, the neural activity is assumed to return to background oscillatory activity with zero mean amplitude until the next onset of a cognitive stage. The time interval between two onsets is variable. Anderson et al. (2016) [10] assumed that this time interval can be modeled with a gamma distribution with shape parameter equal to two and free scale parameter (Fig. 2, below). The scale parameter will be estimated by the HSMM-MVPA. In short, each cognitive stage in the model – except the first stage and the last stage – consists of a 50-msec deflection and a zero mean amplitude interval whose duration is given by a gamma distribution.

The first and the last stage are described by a slightly different model. The first stage does not include a deflection, yet its zero-mean amplitude interval represents the time for the visual stimulus to reach cortical areas. The last stage is bound by the response to the stimulus, although the response does not necessarily represent the end of the ongoing cognitive process. We set the number of cognitive stages in the HSMM-MVPA analysis to six; hence there are five onsets of stages. This choice was based on computational cognitive models of the same cognitive task [10,16]. In this case, the model underlying all trials is a sequence alternating zero mean amplitude intervals with different durations (Si) and 50-msec onsets (Oi) as it follows: S1 + O2 + S2 + O3 + S3 + O4 + S4 + O5 + S5 + O6 + S6 = Trial duration (i.e., time between stimulus onset and response). The same model of a trial is present in all PCs. The duration of each stage on a trial is the same for all PCs on the trial, but the amplitude of the deflections at the onsets may be different for each PC (Fig. 2, topology maps in top row).

HSMMs allow to model systems that have a defined set of hidden states. These systems remain in a hidden state for a certain time, and transitions between hidden states with known probabilities. The hidden states cannot be measured (hence the term "hidden"), however, the probability of an indirect observation given that the system is in a specific hidden state is known. When the transition probabilities and the probability of observations given certain states are unknown (like in our case), a most likely solution can be estimated from the sequence of observations with the expectation-maximization (EM) algorithm associated with HSMM [17].

In our case the observations are the PCs, and the model has six hidden states – the cognitive stages. The unknowns to be found are the stage durations Si, and the amplitude of the onsets' deflection Oi. The EM algorithm estimates iteratively the gamma scale parameter for the stage durations Si and the amplitude of the onsets' deflection Oi so as to maximize with a likelihood function the match between the PCs of all trials and the underlying model (i.e. the sequence of Si and Oi). The intuition for this fitting process is that the EM algorithm moves the onset locations to all possible locations while estimating the onset amplitudes in a way that finds the onset locations and amplitudes that maximize the similarity with the empirical data (i.e., the PCs). We initialized the EM algorithm with uniform random onset amplitudes and gamma distributions with means equal to the longest trial. We performed 500 repetitions of the HSMM-MVPA with different onset amplitudes to make sure that the EM algorithm did not converge to a sub-optimal local maximum. We selected the repetition with the highest likelihood controlling that it was similar to solutions with close likelihoods. We refer the reader to the appendix of [10] for a formal definition of the likelihood function in HSMM-MVPA.

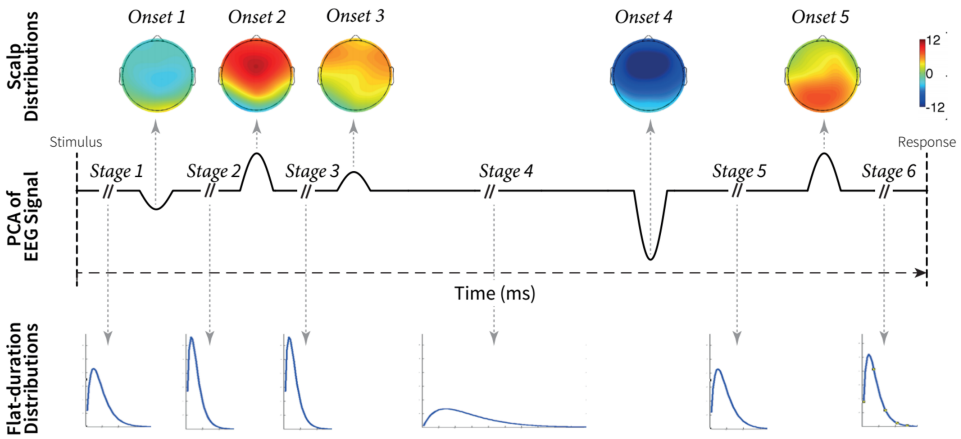

Figure 2. *Schematic representation of the process underlying all trials estimated by the HSMM-MVPA method. The solid black line represents the model of one principal*

component of one EEG trial. This model combines six stages with a mean of zero and five onsets of 50-msec long. The topographical EEG maps on the top are the amplitude of the deflections at the onsets estimated by the HSMM-MVPA. The blue lines at the bottom represent the gamma distributions estimated by the HSMM-MVPA. The gamma distributions determine the duration of the stages. This Figure has been adapted with permission from Anderson et al. (2016) [10]. PCA stands for principal component analysis. EEG stands for electroencephalogram.

2.2.1.6 Localization of relevant cognitive events

The HSMM-MVPA analysis yielded the amplitudes of the multi-dimensional deflections and the scale parameters of the gamma distributions reflecting the length of the stages. In addition, HSMM-MVPA gave the probability distribution of the location of each cognitive stage onset on every trial. These probability distributions were used to estimate the expected location of each onset, as well as the center of each cognitive stage. The center of each cognitive stage was calculated as the middle point between two consecutive stage onsets, or the middle point between the boundary of a trial and its nearest stage onset. In this paper we refer to the onsets and the centers of cognitive stages as relevant 'cognitive events.'

For the characterization of EEG oscillations associated with cognitive functions, we defined relevant cognitive events in a trial as 50-msec windows centered on the onset of each cognitive stage, and 50-msec windows around the center of each cognitive stage. Thus, cognitive events formed a sequence of eleven 50-msec windows alternating the centers of cognitive stages and onsets of cognitive stages. The sequences always began and ended with the center of a cognitive stage. For simplicity, these relevant cognitive events will be abbreviated as – S1 = stage one, onS2 = onset of stage two, S2 = stage two, etc. Figure 3 shows an example of an EEG trial with the probability distributions of the onsets of stages and the 50-msec time windows of analysis.

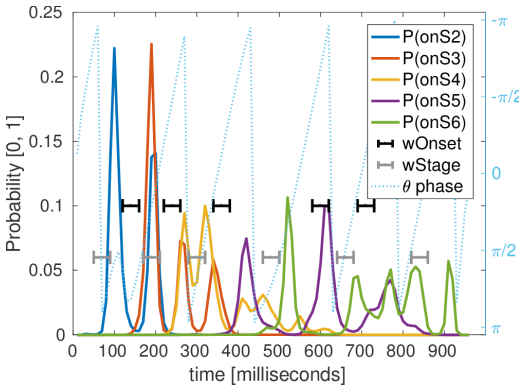

Figure 3. *Example of one trial EEG phase (dotted, light blue), the probability distributions for the location of cognitive stages' onsets (solid lines), and the analysis windows of relevant cognitive events (brackets). The blue-dotted line is the theta band phase during a trial in one electrode. The solid lines are the probability distributions given by the MVPA-HSMM methods regarding the location of the onset of cognitive stages (P(onSX)). Black indicators (wOnset) show the five-sample windows around the expected location of each onset. Similarly, gray indicators show the five-sample windows that define the respective stages (wStage). These time windows are used to compute Power, Inter-trial phase clustering (ITPC), and de-biased weighted phase-lag index (dwPLI).*

Given that some probability distributions of onset locations had a non-stereotypical shape (see Figure 4); we tried to estimate the level of uncertainty about the expected value of these probability distributions. We measured this uncertainty with two different methods. First, we used an statistical test to measure whether the probability distributions were unimodal or multimodal [52]. The test was implemented with the R package diptest (version 0.75-7). Second, we developed a measure of the uncertainty resulting from the probability distributions. We compute this measure of uncertainty in each probability distribution as follows (see Figure 4 right): first, we removed the onset locations (i.e. samples) with the smallest probabilities whose sum represents less than 25 percent. After this step, only the cores of the modes (see faded color area in Figure4 right) remain in the probability distributions. Second, the cores of the modes are normalized to have a total probability of one. Third, the core of the modes whose area accounted for less than 25 percent were removed. We chose a threshold of 25 percent based on the exploration of multiple probability distributions. After the last step only the cores of the most representative modes remain. Finally, we defined uncertainty as the distance between the two most extreme remaining locations (i.e. samples).

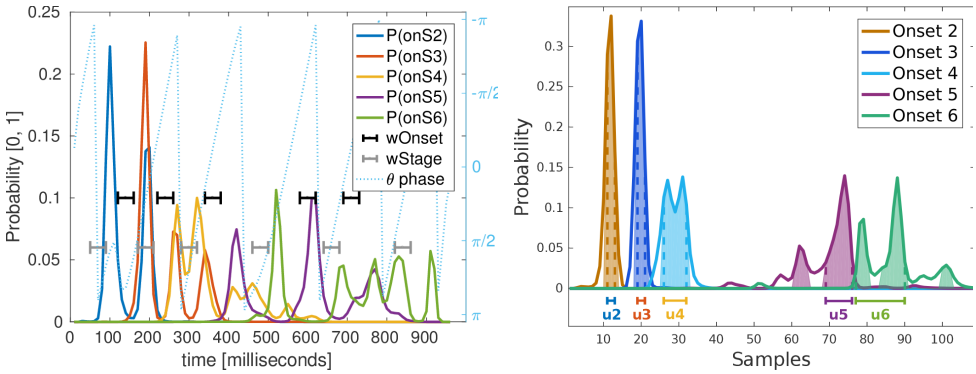

Figure 4. *Left: Example of one trial as in Figure 3, but this trials shows probability distributions of the onsets with multimodal distributions. Estimating these time windows of analysis (wOnset, wStage) may be inaccurate given multimodal probability distributions. Right:Example of the measurement of uncertainty in stage onset locations on one trial. Solid color lines represent the probability of finding the onset of a stage over the trial samples. The semi-transparent area underneath a probability distribution with the same color is the core of the modes in the probability distribution. The core of the modes show the samples that remain after removing the samples that account for the first 25 percent of the probabilities sorted in ascending order. The dashed color lines mark the boundaries of the mode cores that represent at least the most likely 75 percent of the total area under all mode cores in a trial. The uncertainty about the location of an onset is the distance in samples between the two dashed lines of the same color (symbols u2, u3,…,u6).*

2.2.1.7 EEG oscillations

After the EEG was decomposed into the theta, alpha, and beta frequency bands, the analytic signal and the phase of each frequency band were computed with the Hilbert transform. Phase was extracted with the Hilbert transform because it allowed us to precisely define the frequency of interest during bandpass-filtering, and its temporal resolution is the same as the EEG signal. Connectivity between pairs of electrodes across trials was assessed with the de-biased weighted phase-lag index (dwPLI) [53]. dwPLI was chosen because it is robust against volume conductance [54], and it is not biased by the number of trials. dwPLI was computed across trials for each of the five samples of a cognitive event. In order to obtain a robust estimate of connectivity at each relevant cognitive event, the standard deviation of the five-dwPLI measurements in a cognitive event was subtracted from their median. This penalizes connectivity networks that are not stable along the 5 samples window of analysis. Robust dwPLI at each relevant cognitive event was subtracted from baseline dwPLI on

each trial. Baseline dwPLI was computed as the median of the dwPLI across trials over all baseline samples.

The threshold for significant dwPLI between pairs of electrodes was determined on the basis of simulations with surrogate data. We created surrogate data representing the null hypothesis of no connectivity by making a random circular shift of the phase time series in one electrode of each pair of electrodes for each trial. Then, dwPLI was calculated in the same way as for our empirical data. The same process was repeated 200 times. The significance threshold derived from this procedure was Bonferroni-corrected by the number of electrode pairs (i.e., 496 pairs of electrodes). dwPLI measurements from real EEG data below this 95% confidence interval were set to zero.

A global network across subjects was computed for each cognitive event. An edge between two electrodes in the global network was drawn if that edge was present in fifteen or more subjects (i.e., more than 75% of the subjects). The connectivity strength represented on each created edge was computed as the median dwPLI of the contributing subjects.

The power of each frequency band was computed as the squared modulus of the analytic signal. Power was z-scored with respect to the baseline in a single-trial basis. Z-scored power was first averaged across trials and then across subjects. Inter-trial phase clustering (ITPC) (also known as Phase Locking Value) was calculated across trials in order to evaluate phase locking across trials. ITPC at cognitive events was subtracted from baseline ITPC per subject and then averaged across subjects. ITPC was considered significant if it was larger than a critical ITPC of 0.117. Critical ITPC is computed as sqrt(-ln(p)/n) [51], where n is the mean number of trials across subjects and p is a p-value of 0.05 Bonferroni-corrected by the number of electrodes, frequency bands, and cognitive events.

2.3 Results

Synchrony patterns were analyzed in time windows associated with cognitive events derived from the HSMM-MVPA analysis. In total there are eleven time windows of analysis, or cognitive events – the centers of six cognitive stages and the onset of five of these cognitive stages. According to previous works on the same task [16,55], the stages should be interpreted as follows. The first two cognitive stages (i.e. S1, onS2, and S2) are associated with the visual encoding of the stimulus. The third stage is associated with a combination of encoding the second word and judging the familiarity of the encoded words. The fourth stage is the retrieval of memories. The fifth stage is the decision-making process that determines whether the pair of words were studied together or not. Finally, in the sixth stage a motor response is produced.

2.3.1 Location of the onset of cognitive stages

The first analysis step was to estimate the expected location of the onset of cognitive stages from the probability distributions given by the HSMM-MVPA. In Figure 5, the red dots represent the mean expected time when a cognitive stage starts (i.e. the onset) across trials and subjects. Therefore, the distance between two consecutive red dots represents the mean duration of the cognitive stage between the two onsets. The blue bars around red dots (e.g. onS1) show the standard deviation of the time when the onset of the stage occurs. Thus, the variability in stage onset is due to changes on duration of the previous stage. For example, the large standard deviation at the onset of stage five represents the variability in the duration of the stage four. The variability in duration of stage four is in agreement with the results from Anderson et al. (2016) [10], who observed that the mean duration of the fourth stage for different manipulations differed approximately 300ms, while the other stages varied no more than 50ms. Similarly, the computational cognitive model of the same task implemented by Anderson et al. (2016) [10] predicts that stage four durations are sensitive to task manipulations such as word fan and re-pairing of word pairs. As was mentioned above, task manipulations in the original study were not studied separately in our study, so task manipulations are expressed as larger variability in stage four.

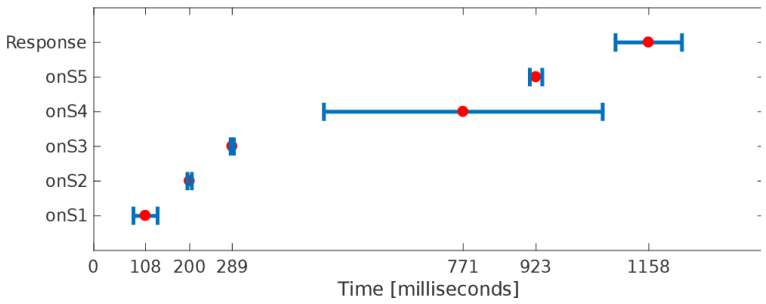

Figure 5. *Temporal location of stage onsets in a trial. The red dot represents the mean onset location across trials and subjects. The blue bars represent the standard deviation on the location of the onset. Y-axis labels the onset to which the red dot and standard deviation belong (onS1: onset of stage one).*

2.3.2 Power, ITPC and connectivity associated with cognitive stages

Next, we examined the connectivity networks in each of the cognitive stages. To do so, we used the windows defined by the HSMM-MVPA to time-lock trials and compute dwPLI, power and ITPC. Figures 6, 7, and 8 show the scalp profiles of grand-averaged power, ITPC, and dwPLI. The scales are consistent across figures for each measurement. Note that the dwPLI connectivity is the same in the power and ITPC plots.

2.3.2.1 Theta band

Theta power is larger during cognitive events than at the baseline period (Figure 6). Right after the stimuli are presented on the screen, processing of visual information starts. The first stage of visual processing shows the weakest increase in power relative to pre-stimulus baseline. However, even though power is relatively low, ITPC is already above significance level in occipital, frontal and central areas.

At the onset of the second stage the encoding of visual information starts. Additionally, a connectivity network emerges connecting occipital with frontal areas and parietal with central areas. This change is accompanied by an increase in power, as well as ITPC, at occipital areas and a broad fronto-central region. Then, during stage two (visual encoding) a dense network arises with connections between posterior, frontal, and temporal regions. ITPC and power increase again in central, pre-frontal, and occipital regions.

At the onset of the third stage a cognitive process of memory familiarity begins, and the previous network of visual encoding disappears (in contrast to the interpretation of Anderson et al., 2016, who assumed that stage 3 included encoding the second word). ITPC in the occipital and fronto-central regions is reduced slightly with respect to the level of the previous event, but it is still above the critical level. Power is also reduced slightly across the whole scalp. During stage four (memory retrieval) ITPC disappears abruptly. Power is also reduced but not as abruptly as ITPC.

Theta activity remains almost unchanged until the onset of stage five (decision making), when a connectivity network emerges. This network connects occipital with left-temporal areas, and midline electrodes with left temporal electrodes, as well as a small network in frontal and right-frontal areas. Power increases globally at the onset of stage five, however ITPC remains low over the whole scalp. During the decision-making stage itself, connectivity between temporal and occipital areas increases further, as well as between midline electrodes and the left-temporal region. In addition, a frontal network appears. Power increases slightly in the frontal area, however ITPC is still low, just like at the onset of the same stage.

At the onset of the last stage a motor response process is initiated. At this onset, the frontal network disappears, but a network between pre-frontal and occipital areas appears. At the same time the connections between occipital and temporal areas increase. Power remains high over the whole scalp. During the motor response stage itself the connectivity network between pre-frontal and occipital areas disappears. Only the connections between occipital, left-temporal and central areas remain, while power and ITPC diminish.

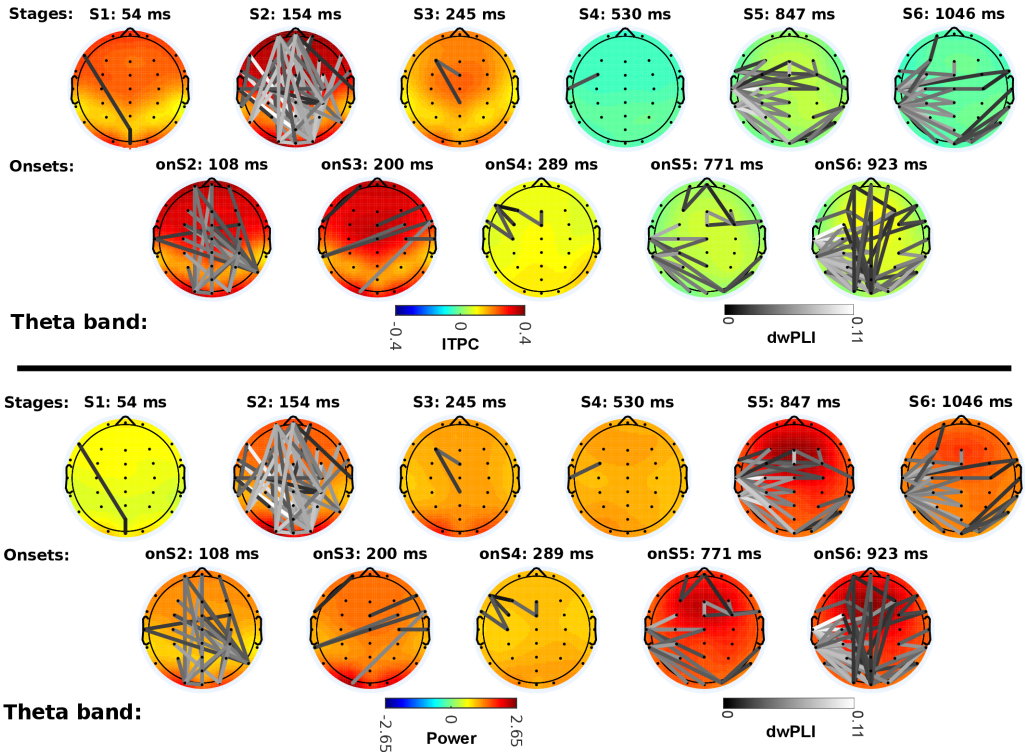

Figure 6. *Theta band power, phase locking (ITPC: inter-trial phase clustering), and phase connectivity (dwPLI: de-biased weighted phase-lag index). Upper panel shows the scalp profiles of grand-averaged ITPC values subtracted from baseline values. Lower panel shows the scalp profiles of grand-averaged power across trials and subjects z-scored with respect to baseline. dwPLI connectivity edges are superimposed on the scalp profiles in gray color scale. The color of edges depicts connectivity strength. Black color represents the lowest connectivity strength above the connectivity significance threshold; white color is the highest observed connectivity strength. dwPLI edges are the same in both panels. The mean temporal location of each scalp map is denoted above of the map (e.g., S1: 54 ms: The stage one starts 54 millisecond after the onset of the trial on average).*

In summary, two large connectivity networks appear in theta band – one fronto-posterior network during the visual encoding, and a left-hemisphere-central and occipital network for the decision-making process during which perceptual and retrieved information are integrated for the motor response. This network expands to motor response as well. ITPC is significant during the three first stages across almost the whole scalp, but it disappears in later stages. Power increases during all cognitive events with respect to baseline, with higher levels in posterior areas during visual encoding, and in frontal areas during decision-making and at the onset of the motor response.

2.3.2.2 *Alpha band*

In the alpha band the change of power and ITPC with respect to baseline is weaker than in the theta band. In stage one power is close to baseline levels, and ITPC increases slightly above critical ITPC. Power increases in the rest of the stages above baseline, but it does not reach a z-score of two in any stage. ITPC increases in frontal and occipital areas during visual encoding, like in the theta band. The largest values of ITPC are observed during stage three. At the onset of the retrieval of memories (stage four) ITPC decreases, but it is still above critical ITPC; as the stage continues it decreases below critical ITPC. During the fourth stage, power in the right frontal area increases. The difference in power between hemispheres is maximal during the decision-making stage (stage five).

At the onset of the decision-making stage, the first connectivity network appears between temporal, frontal and central areas. During the stage itself more edges are incorporated to this network. At the onset of the motor response, the connections between frontal and central areas are lost, and only the network between temporal and central areas remains. During the stage of the motor response a dense network connecting the occipital, parietal, and right temporal areas appears.

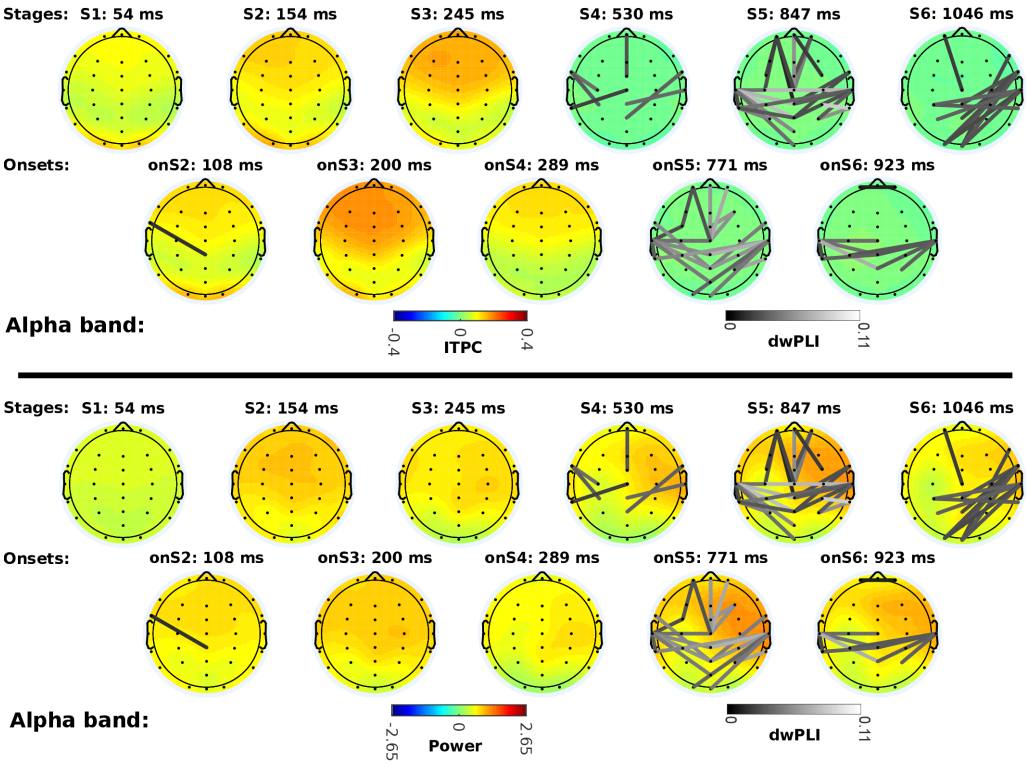

Figure 7. *Alpha band power, phase locking (ITPC: inter-trial phase clustering), and phase connectivity (dwPLI: de-biased weighted phase-lag index). Scalp maps and connectivity follow the same distribution as Figure 6. In order to aid visual comparison, power, ITPC and dwPLI scales are consistent in all scalps maps in Figures 6, 7, and 8.*

In summary, power increases slightly with visual encoding in frontal areas and in later events it is lateralized to the right-frontal area, although the amount of power is less than in theta band. ITPC increases with the onset of visual encoding and becomes maximal during memory retrieval in frontal areas. Connectivity networks do not emerge until the onset of decision-making, at which time an inter-hemispheric network between predominantly temporal and parietal areas evolves along with a fronto-central network. During motor response a new network between right-temporal, parietal, and occipital areas appears.

2.3.2.3 Beta band

We analyzed power, ITPC, and connectivity in the beta band in the same way as with theta and alpha bands (Figure 8). Beta band power fluctuations with respect to baseline were negligible in comparison with theta or alpha power fluctuations. Moreover, ITPC was non-existent, and the same was true for connectivity. For this reason, beta band activity is not reported here in detail. The relative absence of activity in the beta band could be related to the sensitivity of ITPC and dwPLI to time jitters across trials in combination with the short period of beta oscillations, which makes it difficult to have reliable measurements of phase. Temporal jitter issues are even more acute in the gamma frequency band, which is the reason for leaving it out of this study entirely.

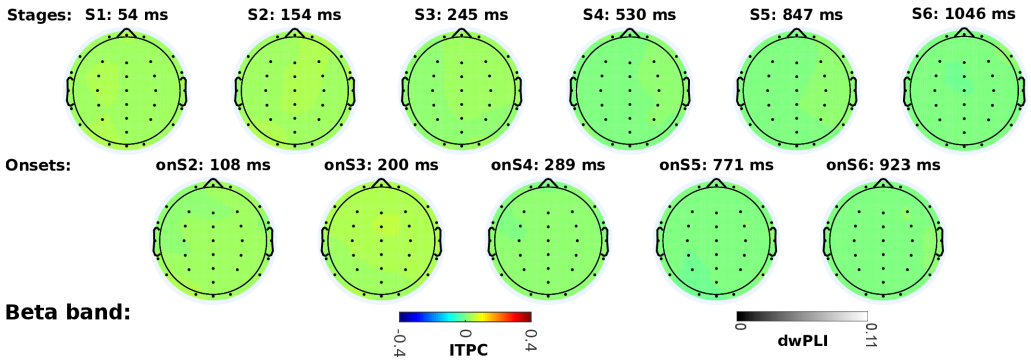

Figure 8. *Beta band phase locking (ITPC: inter-trial phase clustering), and phase connectivity (dwPLI: de-biased weighted phase-lag index). It shows scalp profiles of grand-averaged ITPC values subtracted from baseline values. The row above has the centers of stages, and the row below the onset of stages. ITPC has the same color scale as*

Figures 6, 7, and 8. There is not any phase connectivity edge that is consistent across a minimum of subjects (i.e. 75 percent of the subjects). The mean temporal location of each scalp map is depicted above them (e.g. S1: 54 ms: The stage one start 54 millisecond after the onset of the trial on average).

2.4 Discussion

Our aim was to relate synchrony networks to different functional cognitive stages, identified by previous modeling work in an associative recognition memory task. We used the HSMM-MVPA method to discover cognitive events on a trial-by-trial basis, which allowed us to find the onsets of a series of task stages. We demonstrated that particular patterns of phase locking, phase connectivity and power in the theta and alpha bands arise at each cognitive stage. The next section discusses the evolution of phase locking and phase connectivity along the cognitive stages involved in associative recognition memory – visual encoding, familiarity, memory retrieval, decision-making, and motor response. It is important to note here that typically, it is assumed that even in the case of foils a memory is retrieved, which is then compared to the stimuli on the screen, and being different leads to a negative decision (recall-to-reject; see e.g.,[18,20,56–58]). As a result, all trials in the current dataset involve the same cognitive processes, which in the case of targets leads to a positive decision and in the case of foils to a negative decision.

2.4.1 Functional Interpretation of Synchrony Patterns

The analysis of EEG synchrony presented here sheds light on the dynamics of phase locking and connectivity networks and their role in cognition. Our results suggest that connectivity networks change gradually across cognitive stages, rather than sharply when a new cognitive stage starts.

Visual encoding seems to involve theta ITPC throughout all visual encoding stages including the onset of the memory retrieval. Connectivity emerges at the onset of the second visual encoding stage with long-rage frontal and posterior connections which substantially increase in number during the second stage of visual encoding. This finding is in agreement with the fronto-posterior network observed by [35] during encoding of visual information, as well as a top-down control activation [30]. These connections, including the occipital-temporal connections are probably related to storing the concepts related to the stimuli on the screen in a short-term visual memory store. These networks disappear with the onset of the third stage. Anderson et al. (2016) [10] hypothesize that the third stage is related to the visual encoding of the second word while judging the familiarity of the first word (see also Borst & Anderson, 2015, for a similar interpretation). Because the fronto-occipital networks associated with visual encoding are present during the second stage but disappear in the third stage, our results suggest that the third stages reflects a relatively pure

familiarity process that follows the encoding of both words in stage two. This is in agreement with earlier EEG correlates of the dual-process theory of associative recognition (e.g., [59]), and shows how these connectivity analyses improve our understanding of the discovered stages.

A slow change in connectivity networks is observed during the processes of decision-making and motor response. Interestingly, the alpha and theta band show completely different topologies. On the one hand, alpha band connectivity emerges with the onset of decision making between temporal, parietal, and frontal areas. These results are in line with several previous studies. Based on a different EEG experiment, [60] hypothesized that in this stage the words that are on the screen are compared to a pair (or triplet in this experiment) retrieved from memory, word by word. Additionally, MEG data has shown that word pairs were retrieved from temporal regions and subsequently represented pre-frontally, while the comparison itself was associated with activation in the parietal cortex [55]. The process to identify pairs of words learned also seem to be in agreement with the network found by Mima et al. (2001) [44] for object recognition. Finally, during the motor response the inter-hemispheric and frontal networks are reduced to connections between the right-temporal area with parietal and occipital areas.

On the other hand, theta band connections do not appear until the onset of the decision-making stage. At the onset of decision making an isolated network appears in the pre-frontal area. This network may be related with the frontal network observed in the alpha band as well. Additionally, a network between left-temporal, central, and occipital areas becomes visible. This network may indicate the preparation of the hand for a posterior response with the finger once the decision is taken, and perhaps a reactivation of the word pair based on the visual percepts of the words. During the stage of decision making, the pre-frontal network disappears and more connections appear within the left hemisphere – except the pre-frontal area – and between the occipital and the right-temporal areas. At the onset of motor response long-range connections between pre-frontal and occipital areas appear in addition to the network observed during decision making. Later, during the motor response, only the long-range connections between frontal and posterior areas disappear. As suggested by Wu et al. (2007) [48] the temporal-parietal networks may support the process of binding of information, while fronto-posterior networks control the access to information in posterior areas.

In general terms, according to our review of literature on connectivity, the dense fronto-posterior network that we observed during visual encoding may be related with top-down control and encoding of information. The inter-hemispheric network and the occipito-temporal network during decision making could be associated with the comparison of information retrieved from memory with the visual information on the screen. The long-

range connections between frontal, central and posterior areas may indicate executive control function during the binding of information.

2.4.2 The HSMM-MVPA method

We based our selection of time-windows of analysis on the results of the HSMM-MVPA method. This method assumes that at the onset of the cognitive stages there is a deflection of the EEG signal across multiple electrodes, which should also be manifest in larger power at the onset of each event relative to the period between different events. Indeed, onsets showed higher median power than stages in alpha and theta bands with a confidence interval of 95 percent (see Figure 9) Moreover, a Wilcoxon rank-sum test indicates that these differences on power are significant (p-value >> 0.01) for alpha and theta bands. In addition, the median power at onsets is higher in the theta band than in the alpha band with a 95 percent confidence interval and significant according to a Wilcoxon rank-sum test. Power level can be compared across frequency bands because power was z-scored with respect to the power at the baseline. Following the assumption made by HSMM-MVPA, the baseline should contain only background oscillatory activity.

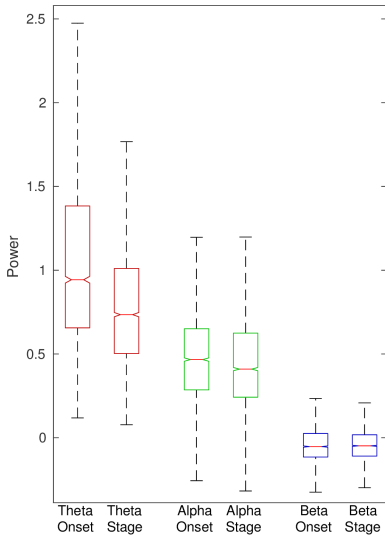

Figure 9 *Box plot comparing the power in the onset (Onset) of the stages and the power in the interval between onsets or trial edges (Stage). Red color boxes represent the theta band power. Green color boxes represent the alpha band power. Blue color boxes represent the beta band power. The box plot was drawn with the boxplot function in Matlab.*

Since the onsets are modeled as 50-msec deflections, it would logically follow that power at the onsets in alpha band should be higher than power in theta band. Nonetheless,

Anderson et al. (2016) [10] showed on synthetic data that HSMM-MVPA was able to recover with high accuracy onsets modeled as half-sinus deflection lasting from 30 to 110-msec. This means that the onsets found by HSMM-MVPA can produce increased power in theta and alpha bands. Furthermore, we use a 50-msec window to analyze the power. The center of this time window is estimated as the expected value of the probability distribution of the onset location. As we discussed before, the uncertainty of the HSMM-MVPA is higher than the 50-msec analysis window. Therefore, the peak of power at the onset might not match the center of the 50-msec analysis window. This will introduce a bias in estimating power at the onsets – power at onsets shorter than 55-msec (i.e. alpha band) might be underestimated because the 50-msec analysis window captures background ongoing oscillations and not the full deflection; Onsets longer than 55-msec (i.e. theta band) are more likely to stay within the 50-msec window of analysis, so the power inside the window of analysis is higher.

Applying the HSMM-MVPA to real data produced more uncertainty about the onset locations than the 140-msec previously reported on synthetic data [10]. We tested it first by applying a test of unimodality [52] to the probability distributions of the onset locations. The test of unimodality reported that 66.2 percent of the probability distributions were not unimodal. In addition, we created a measure of uncertainty about the location of an onset (see Methods, see Figure 4). We concluded that 85.5 percent of the probability distributions (i.e., all trials times the five onsets on each trial) are within the140-msec uncertainty reported by Anderson et al. (2016) [10] in synthetic data, while the remaining 14.5% of the trials present more than 140-msec uncertainty.

Despite this uncertainty, we still observe phase connectivity and phase consistency at several cognitive events that are consistent across many subjects, suggesting that our analysis is robust enough to deal with this uncertainty. Nevertheless, uncertainty could compromise the detection of synchrony in studies with fewer trials than the current study, or in higher frequency bands – providing a potential explanation for the lack of findings in the beta band in our study. A further argument for the robustness of this method to temporal uncertainty are the clear differences in connectivity patterns that we observed between the identified stages. As such, the current analysis lends additional credibility to the idea that the HSMM-MVPA method identifies functionally distinct cognitive stages.

2.4.3 Conclusion

We have identified patterns of EEG synchrony related with specific cognitive stages in an associative recognition memory task. We have shown that combining HSMM-MVPA with oscillatory connectivity analysis increases the capacity to characterize cognitive functions, considerably extending the applicability of this connectivity analysis. Our principled model-based approach gives us detailed information about the cognitive operations

associated with each stage, which we can then relate to the relevant connectivity pattern. This approach has shown that there is a familiarity stage between the encoding of visual information and the retrial of memories. Future studies should validate these mappings between cognitive operations and connectivity patterns in different cognitive tasks. Together, this method opens a new window to understand the dynamical interactions between brain regions in the service of complex cognitive behavior.

Institutional acknowledgment

This work was funded by European Research Council Starting Grant MULTITASK 283597, a Netherlands Organization for Scientific Research Veni grant 451-15-040 awarded to JPB, and the Data Science and Systems Complexity Center, University of Groningen. We would like to thank the Center for Information Technology of the University of Groningen for their support and for providing access to the Peregrine high-performance computing cluster.

Data accessibility statement

No original data was reported in this paper, we refer to Borst and Anderson, 2015, who released the data analyzed in this paper, for more information. We publish the data and the code used for this paper in Figshare portal with DOI: 10.6084/m9.figshare.5722831

References

1. Varela F, Lachaux JP, Rodriguez E, Martinerie J. The brainweb: phase synchronization and large-scale integration. Nat Rev Neurosci. 2001;2: 229–239. doi:10.1038/35067550
2. Fries P. Rhythms for Cognition: Communication through Coherence. Neuron. 2015;88: 220–235. doi:10.1016/j.neuron.2015.09.034
3. Hanslmayr S, Gross J, Klimesch W, Shapiro KL. The role of α oscillations in temporal attention. Brain Res Rev. 2011;67: 331–343. doi:10.1016/j.brainresrev.2011.04.002
4. Klimesch W. α-band oscillations, attention, and controlled access to stored information. Trends Cogn Sci (Regul Ed). 2012;16: 606–617. doi:10.1016/j.tics.2012.10.007
5. Hillyard SA, Anllo-Vento L. Event-related brain potentials in the study of visual selective attention. PNAS. 1998;95: 781–787. doi:10.1073/pnas.95.3.781
6. Vugt MK van, Simen P, Nystrom L, Holmes P, Cohen JD. Lateralized Readiness Potentials Reveal Properties of a Neural Mechanism for Implementing a Decision Threshold. PLOS ONE. 2014;9: e90943. doi:10.1371/journal.pone.0090943
7. Lehmann D. Brain Electric Microstates and Cognition: The Atoms of Thought. In: John ER, Harmony T, Prichep LS, Valdés-Sosa M, Valdés-Sosa PA, editors. Machinery of the Mind: Data, Theory, and Speculations About Higher Brain Function. Boston, MA: Birkhäuser; 1990. pp. 209–224. doi:10.1007/978-1-4757-1083-0_10
8. Cabral J, Luckhoo H, Woolrich M, Joensson M, Mohseni H, Baker A, et al. Exploring mechanisms of spontaneous functional connectivity in MEG: How delayed network interactions lead to structured amplitude envelopes of band-pass filtered oscillations. NeuroImage. 2014;90: 423–435. doi:10.1016/j.neuroimage.2013.11.047
9. Vidaurre D, Quinn AJ, Baker AP, Dupret D, Tejero-Cantero A, Woolrich MW. Spectrally resolved fast transient brain states in electrophysiological data. Neuroimage. 2016;126: 81–95. doi:10.1016/j.neuroimage.2015.11.047
10. Anderson JR, Zhang Q, Borst JP, Walsh MM. The discovery of processing stages: Extension of Sternberg's method. Psychol Rev. 2016;123: 481–509. doi:10.1037/rev0000030
11. Shah AS, Bressler SL, Knuth KH, Ding M, Mehta AD, Ulbert I, et al. Neural dynamics and the fundamental mechanisms of event-related brain potentials. Cereb Cortex. 2004;14: 476–483. doi:10.1093/cercor/bhh009
12. Başar E. EEG-brain Dynamics: Relation Between EEG and Brain Evoked Potentials. Elsevier/North-Holland Biomedical Press; 1980.
13. Makeig S. Dynamic Brain Sources of Visual Evoked Responses. Science. 2002;295: 690–694. doi:10.1126/science.1066168
14. Yeung N, Bogacz R, Holroyd CB, Cohen JD. Detection of synchronized oscillations in the electroencephalogram: an evaluation of methods. Psychophysiology. 2004;41: 822–832. doi:10.1111/j.1469-8986.2004.00239.x
15. Yeung N, Bogacz R, Holroyd CB, Nieuwenhuis S, Cohen JD. Theta phase resetting and the error-related negativity. Psychophysiology. 2007;44: 39–49. doi:10.1111/j.1469-8986.2006.00482.x
16. Borst JP, Anderson JR. The discovery of processing stages: Analyzing EEG data with hidden semi-Markov models. NeuroImage. 2015;108: 60–73. doi:10.1016/j.neuroimage.2014.12.029
17. Yu S-Z. Hidden semi-Markov models. Artificial Intelligence. 2010; 29.
18. Anderson JR, Reder LM. The fan effect: New results and new theories. Journal of Experimental Psychology: General. 1999;128: 186–197. doi:10.1037/0096-3445.128.2.186
19. Yonelinas AP. The Nature of Recollection and Familiarity: A Review of 30 Years of Research. Journal of Memory and Language. 2002;46: 441–517. doi:10.1006/jmla.2002.2864
20. Schneider DW, Anderson JR. Modeling fan effects on the time course of associative recognition. Cognitive Psychology. 2012;64: 127–160. doi:10.1016/j.cogpsych.2011.11.001
21. Sternberg S. The discovery of processing stages: Extensions of Donders' method. Acta Psychologica. 1969;30: 276–315. doi:10.1016/0001-6918(69)90055-9
22. Sternberg S. High-speed scanning in human memory. Science. 1966;153: 652–654. doi:10.1126/science.153.3736.652

23. Anderson JR, Bothell D, Lebiere C, Matessa M. An Integrated Theory of List Memory. Journal of Memory and Language. 1998;38: 341–380. doi:10.1006/jmla.1997.2553

24. Jacobs J, Hwang G, Curran T, Kahana MJ. EEG oscillations and recognition memory: theta correlates of memory retrieval and decision making. Neuroimage. 2006;32: 978–987. doi:10.1016/j.neuroimage.2006.02.018

25. Sauseng P, Hoppe J, Klimesch W, Gerloff C, Hummel FC. Dissociation of sustained attention from central executive functions: local activity and interregional connectivity in the theta range. Eur J Neurosci. 2007;25: 587–593. doi:10.1111/j.1460-9568.2006.05286.x

26. Mizuhara H, Yamaguchi Y. Human cortical circuits for central executive function emerge by theta phase synchronization. Neuroimage. 2007;36: 232–244. doi:10.1016/j.neuroimage. 2007.02.026

27. Düzel E, Penny WD, Burgess N. Brain oscillations and memory. Curr Opin Neurobiol. 2010;20: 143–149. doi:10.1016/j.conb.2010.01.004

28. Kopp F, Schröger E, Lipka S. Synchronized brain activity during rehearsal and short-term memory disruption by irrelevant speech is affected by recall mode. Int J Psychophysiol. 2006;61: 188–203. doi:10.1016/j.ijpsycho.2005.10.001

29. Sauseng P, Klimesch W, Doppelmayr M, Hanslmayr S, Schabus M, Gruber WR. Theta coupling in the human electroencephalogram during a working memory task. Neurosci Lett. 2004;354: 123–126. doi:10.1016/j.neulet.2003.10.002

30. Sauseng P, Klimesch W, Freunberger R, Pecherstorfer T, Hanslmayr S, Doppelmayr M. Relevance of EEG alpha and theta oscillations during task switching. Exp Brain Res. 2006;170: 295–301. doi:10.1007/s00221-005-0211-y

31. Vincent JL, Kahn I, Snyder AZ, Raichle ME, Buckner RL. Evidence for a frontoparietal control system revealed by intrinsic functional connectivity. J Neurophysiol. 2008;100: 3328–3342. doi:10.1152/jn.90355.2008

32. Cole MW, Schneider W. The cognitive control network: Integrated cortical regions with dissociable functions. Neuroimage. 2007;37: 343–360. doi:10.1016/j.neuroimage.2007.03.071

33. Dosenbach NUF, Fair DA, Miezin FM, Cohen AL, Wenger KK, Dosenbach RAT, et al. Distinct brain networks for adaptive and stable task control in humans. Proc Natl Acad Sci U S A. 2007;104: 11073–11078. doi:10.1073/pnas.0704320104

34. Borst JP, Anderson JR. Using model-based functional MRI to locate working memory updates and declarative memory retrievals in the fronto-parietal network. Proc Natl Acad Sci U S A. 2013;110: 1628–1633. doi:10.1073/pnas.1221572110

35. Sarnthein J, Petsche H, Rappelsberger P, Shaw GL, Stein AV. Synchronization between prefrontal and posterior association cortex during human working memory. Proc Natl Acad Sci USA. 1998; 5.

36. Weiss S, Rappelsberger P. Long-range EEG synchronization during word encoding correlates with successful memory performance. Brain Res Cogn Brain Res. 2000;9: 299–312. doi:10.1016/s0926-6410(00)00011-2

37. Summerfield C, Mangels JA. Coherent theta-band EEG activity predicts item-context binding during encoding. Neuroimage. 2005;24: 692–703. doi:10.1016/j.neuroimage.2004.09.012

38. Cavanagh JF, Frank MJ. Frontal theta as a mechanism for cognitive control. Trends Cogn Sci. 2014;18: 414–421. doi:10.1016/j.tics.2014.04.012

39. Anokhin AP, Lutzenberger W, Birbaumer N. Spatiotemporal organization of brain dynamics and intelligence: an EEG study in adolescents. Int J Psychophysiol. 1999;33: 259–273. doi:10.1016/s0167-8760(99)00064-1

40. Clayton MS, Yeung N, Cohen Kadosh R. The roles of cortical oscillations in sustained attention. Trends Cogn Sci. 2015;19: 188–195. doi:10.1016/j.tics.2015.02.004

41. Klimesch W, Freunberger R, Sauseng P. Oscillatory mechanisms of process binding in memory. Neurosci Biobehav Rev. 2010;34: 1002–1014. doi:10.1016/j.neubiorev.2009.10.004

42. Klimesch W, Freunberger R, Sauseng P, Gruber W. A short review of slow phase synchronization and memory: evidence for control processes in different memory systems? Brain Res. 2008;1235: 31–44. doi:10.1016/j.brainres.2008.06.049

43. Kujala J, Pammer K, Cornelissen P, Roebroeck A, Formisano E, Salmelin R. Phase coupling in a cerebro-cerebellar network at 8-13 Hz during reading. Cereb Cortex. 2007;17: 1476–1485. doi:10.1093/cercor/bhl059

44. Mima T, Oluwatimilehin T, Hiraoka T, Hallett M. Transient interhemispheric neuronal synchrony correlates with object recognition. J Neurosci. 2001;21: 3942–3948.

45. Classen J, Gerloff C, Honda M, Hallett M. Integrative visuomotor behavior is associated with interregionally coherent oscillations in the human brain. J Neurophysiol. 1998;79: 1567–1573. doi:10.1152/jn.1998.79.3.1567

46. Andres FG, Gerloff C. Coherence of sequential movements and motor learning. J Clin Neurophysiol. 1999;16: 520–527. doi:10.1097/00004691-199911000-00004

47. Hummel F, Gerloff C. Larger interregional synchrony is associated with greater behavioral success in a complex sensory integration task in humans. Cereb Cortex. 2005;15: 670–678. doi:10.1093/cercor/bhh170

48. Wu X, Chen X, Li Z, Han S, Zhang D. Binding of verbal and spatial information in human working memory involves large-scale neural synchronization at theta frequency. Neuroimage. 2007;35: 1654–1662. doi:10.1016/j.neuroimage.2007.02.011

49. Borst JP, Schneider DW, Walsh MM, Anderson JR. Stages of processing in associative recognition: evidence from behavior, EEG, and classification. J Cogn Neurosci. 2013;25: 2151–2166. doi:10.1162/jocn_a_00457

50. Delorme A, Makeig S. EEGLAB: an open source toolbox for analysis of single-trial EEG dynamics including independent component analysis. J Neurosci Methods. 2004;134: 9–21. doi:10.1016/j.jneumeth.2003.10.009

51. Cohen MX. Analyzing Neural Time Series Data: Theory and Practice. 1st edition. Cambridge, Massachusetts: The MIT Press; 2014.

52. Hartigan JA, Hartigan PM. The Dip Test of Unimodality. The Annals of Statistics. 1985;13: 70–84.

53. Vinck M, Oostenveld R, van Wingerden M, Battaglia F, Pennartz CMA. An improved index of phase-synchronization for electrophysiological data in the presence of volume-conduction, noise and sample-size bias. Neuroimage. 2011;55: 1548–1565. doi:10.1016/j.neuroimage. 2011.01.055

54. Cohen MX. Effects of time lag and frequency matching on phase-based connectivity. J Neurosci Methods. 2015;250: 137–146. doi:10.1016/j.jneumeth.2014.09.005

55. Borst JP, Ghuman AS, Anderson JR. Tracking cognitive processing stages with MEG: A spatio-temporal model of associative recognition in the brain. NeuroImage. 2016;141: 416–430. doi:10.1016/j.neuroimage.2016.08.002

56. Rotello CM, Heit E. Associative recognition: a case of recall-to-reject processing. Mem Cognit. 2000;28: 907–922. doi:10.3758/bf03209339

57. Rotello CM, Macmillan NA, Van Tassel G. Recall-to-Reject in Recognition: Evidence from ROC Curves. Journal of Memory and Language. 2000;43: 67–88. doi:10.1006/jmla.1999.2701

58. Malmberg KJ. Recognition memory: a review of the critical findings and an integrated theory for relating them. Cogn Psychol. 2008;57: 335–384. doi:10.1016/j.cogpsych.2008.02.004

59. Rugg MD, Curran T. Event-related potentials and recognition memory. Trends Cogn Sci. 2007;11: 251–257. doi:10.1016/j.tics.2007.04.004

60. Zhang Q, Walsh MM, Anderson JR. The Effects of Probe Similarity on Retrieval and Comparison Processes in Associative Recognition. J Cogn Neurosci. 2017;29: 352–367. doi:10.1162/jocn_a_01059

3 Modulations of local synchrony over time lead to resting-state functional connectivity in a parsimonious large-scale brain model

Biophysical models of large-scale brain activity are a fundamental tool for understanding the mechanisms underlying the patterns observed with neuroimaging. These models combine a macroscopic description of the within- and between-ensemble dynamics of neurons within a single architecture. A challenge for these models is accounting for modulations of within-ensemble synchrony over time. Such modulations in local synchrony are fundamental for modeling behavioral tasks and resting-state activity. Another challenge comes from the difficulty in parametrizing large scale brain models which hinders researching principles related with between-ensembles differences. Here we derive a parsimonious large scale brain model that can describe fluctuations of local synchrony. Crucially, we do not reduce within-ensemble dynamics to macroscopic variables first, instead we consider within and between-ensemble interactions similarly while preserving their physiological differences. The dynamics of within-ensemble synchrony can be tuned with a parameter which manipulates local connectivity strength. We simulated resting-state static and time-resolved functional connectivity of alpha band envelopes in models with identical and dissimilar local connectivities. We show that functional connectivity emerges when there are high fluctuations of local and global synchrony simultaneously (i.e. metastable dynamics). We also show that for most ensembles, leaning towards local asynchrony or synchrony correlates with the functional connectivity with other ensembles, with the exception of some regions belonging to the default-mode network.[2]

2 Submitted as Portoles, O., Qin, Y., Hadida, J., Woolrich, M., Cao, M., van Vugt, M., "*Modulations of local synchrony over time lead to resting-state functional connectivity in a parsimonious large-scale brain model*".

3.1 Introduction

The human brain is one of the most complex systems found in nature, consisting of billions of neurons. Human behavior cannot be understood from only the computing properties of individual neurons. Instead, human behavior requires the coordination of many ensembles of neurons at multiple spatial scales. Neuroimaging studies reveal that patterns of large-scale local and distributed coordination appear and dissolve during behavioral tasks [1–5] , as well as resting-state [6–10].

Biophysical models of large-scale brain networks provide a unified analysis framework for understanding the mechanistic principles that generate large-scale patterns of neural activity. In a generative biophysical model of large-scale whole-brain neural activity (GWBM) the nodes represent the electrophysiological dynamics of ensembles of neurons. These ensembles of neurons interact via neural white matter fibers (edges) that can be derived from diffusion tractography images [11–13]. Currently it is computationally prohibitive to simulate all neurons and synapses in the brain. Moreover, even if it were possible, modeling such a large number of elements would yield results that would be challenging to interpret. Therefore, the neural activity in an ensemble of adjacent neurons is reduced mathematically to a few macroscopic variables. These macroscopic variables are subsequently coupled through the network of white matter fibers and used to simulate neuroimaging data such as magnetoencephalography (MEG) or functional magnetic resonance imaging.

GWBMs have been used among others to determine the relationship between the anatomical structure of neural fibers, the connectome, and the functional connectivity (FC) observed during the resting state [11,14,15]; to assess the influence of source reconstruction or tractography seeding methods on neuroimaging analysis [16,17]; to create personalized models of seizure activity in epileptic patients or models aiding surgical interventions [18–20]; to analyze the sources and sinks of brain waves [21]; to model flows of information through the brain [22]; and to derive the conditions necessary for selective synchronization between ensembles of neurons [23].

However, the assumptions that are made to be able to derive the macroscopic variables which describe the neural activity in an ensemble of neurons impose limitations. A fundamental limitation is that the macroscopic variables cannot describe within-ensemble modulations of synchronization [5,12,24]. Yet, it is exactly these local fluctuations of local synchrony (often referred to as event-related synchronization/desynchronization) that characterize behavioral tasks [25], and are associated with changes in functional connectivity between brain regions during tasks and on-going activity [3,4]. In addition, there is increasing evidence that these local fluctuations can be short-lived (i.e., transient and bursting) in tasks and resting-state [9,10]. Another limitation is more practical as the

number of parameters often scales with the level of biological detail which makes it difficult to fit such models. As a result, most studies assume identical parameters for all ensembles, and thereby neglect between-ensemble differences.

While biologically realistic GWBMs are impractical to model between-ensemble differences, such differences have been modeled with non-biological models. The latter GWBMs model each ensemble as a Stuart-Landau oscillator (SL) [26,27]. Although one SL can describe the mean firing rate in an ensemble of neurons for particular parameterizations [28,29], the SL is obtained from models of macroscopic activity that cannot capture modulations of local synchrony [12,24]. Moreover, when a set of SL oscillators with additive noise and various bifurcation parameters are coupled in a heterogeneous network with time-delays – as they are in GWBMs [27,30], it is very difficult to estimate the range of amplitudes of these SL oscillators. Therefore, it is hard to interpret their amplitudes as the local degree of synchrony and to compare amplitude differences across oscillators.

To obtain a GWBM that explicitly accounts for modulations of local synchrony and still has a low number of parameters, we introduce here a low-dimensional GWBM derived from a network-of-networks of Kuramoto oscillators. The Kuramoto oscillators are a canonical model of synchronization in biological systems, and they account for many of the dynamics of synchrony found in neural populations such as traveling waves and metastability [15,31,32]. Each sub-network of Kuramoto oscillators in this GWBM represents an ensemble of neurons within a particular cortical region, and its synchrony is given by the Kuramoto order parameter (KOP) [33,34]. The KOP has been found to be a good measure of synchrony in an ensemble of neurons whose dynamics are reduced with a mean-field approach [24,35,36]. In turn this mean-field reduction captures modulations of synchrony and explains event-related de/synchronization [5].

There are previous GWBMs that have used a network-of-networks of Kuramoto oscillators structure [20,23,37,38]. Yet, these GWBMs did not model resting-state FC, and their formulation is computationally expensive for GWBMs. Moreover their dynamics are influenced by the number of oscillators in the sub-networks and their natural frequencies [39,40]. Such finite-size effects are relevant for modeling resting-state because resting-state FC emerges at the point with the largest finite-size effects – the edge between asynchrony and partial synchrony [11,27,41]. To solve these problems we applied a mean-field reduction over a model with infinite oscillators on each sub-network. This reduction gave one equation per sub-network that describes the evolution of the local synchrony with the KOP. Moreover, the dynamics of the KOP are manipulated with the local coupling parameter that represents the local connectivity strength.

Our GWBM simulated resting-state alpha band static FC (sFC) and time-resolved FC (trFC) of amplitude envelopes in two scenarios of increasing complexity. The first scenario assumes identical ensembles (homogeneous ensembles), whereas the second scenario generalized this to the case with different local connectivity strengths for each ensemble (heterogeneous ensembles). Our results show that FC emerges in both scenarios when high metastable dynamics (i.e., temporal fluctuations of synchrony) coexist within-ensembles and between-ensembles. At this working point, repulsion from local synchrony along with time-delayed attraction to global synchrony leads to coordinated fluctuations of local synchrony that are responsible for creating changing patterns of FC. At the same time, there are ensembles that are attracted to local synchrony which do not have FC, but influence other ensembles. An exception to this behavior are ensembles that represent parts of the default-mode network as they are attracted to local synchrony and also are functionally connected to each other.

3.2 Results

3.2.1 Dynamics of the large-scale brain model

The GWBM that we propose is defined by equations 1a and 1b, which describe the temporal evolution of the KOP in one ensemble (i.e. the local synchrony within the ensemble). The dynamics of this GWBM are governed by the global coupling parameter G, the local coupling of each ensemble L_n, the spike-propagation velocity (proportional to the time-delays τ_{np}), and the probability distribution of natural frequencies in each ensemble (Ω_n central natural frequency; Δ_n spread of natural frequencies). We focus on the impact of global and local couplings as well as time delays, and assume an identical frequency distribution for all ensembles ($\Omega = 10.5$ Hz, $\Delta=1$). The section *model and methods* explains this GWBM in detail.

$$\dot{r}_n = -\Delta_n r_n + \frac{L_n}{2}(1-r_n^2)r_n + \frac{G}{2E}(1-r_n^2)\sum_{p=1,p\neq n}^{E} A_{np} r_p(t-\tau_{np})\cos\left(\psi_p(t-\tau_{np})-\psi_n\right) \quad (1a)$$

$$\dot{\psi}_n = \Omega_n + \frac{G}{2E}\left(r_n + \frac{1}{r_n}\right)\sum_{p=1,p\neq e}^{E} A_{np} r_p(t-\tau_{np})\sin\left(\psi_p(t-\tau_{np})-\psi_n\right) \quad (1b)$$

In these equations, the over dot represents the time derivative. Notice that we have removed the time dependency of r and ψ when they do not have time delays. Equation 1a represents the temporal evolution of the level of synchronization within ensemble n (brain region). The variable r is bounded between zero and one, where zero means full desynchronization and one means full synchronization. Equation 1a can be divided into three parts by the plus signs. The first and second parts represent local dynamics, while the third part encapsulates the interaction with other ensembles.

- The first part opposes within-ensemble synchrony due to the heterogeneity of natural frequencies Δ_n.
- The second part contains the local coupling parameter L_n , which tunes the connectivity strength within the ensemble.
- The last part scales between-ensemble coupling strength, G, as well as the interaction delays, τ_{np}. The interaction between ensembles depends on the density of neural fibers between them, A_{np}, their phase differences, and their local synchronies.

The contribution of L_n over r_n can be assessed by assuming that the global coupling is equal to zero. With this assumption, equation 1a becomes the mean-field reduction of a canonical Kuramoto model [42]. For this equation, there is a critical coupling value (L^c) at $L_n = 2\Delta_n$. Thus, ensembles with $L_n > 2\Delta_n$ tend to synchronize, while ensembles with $L_n<2\Delta_n$ tend to become desynchronized. The lower L_n (including negative values), the more asynchronous the ensemble, $r_n \rightarrow 0$ [43]. In addition, the further away L_n is from L^c, the stronger the influence of L_n on r_n. Equation 1b describes the dynamics of the mean phase of the oscillations within the ensemble n. The mean phase evolves at the pace of its natural frequency, Ω_n, plus the interaction with other ensembles scaled by G/E and approximately the inverse of its own local synchrony level. Therefore, locally desynchronized ensembles (small r_n) are strongly influenced by other ensembles, while locally synchronized ensembles ($r_n \sim 1$) are almost not influenced by others.

In what follows, we refer to r_n as the local synchrony. The phase synchronization among all ensembles, R, is referred as global synchrony. Global synchrony was measured as the KOP of the local phases as follows,

$$R = \left|\frac{1}{N}\sum_{n=1}^{E} e^{i\psi_n}\right| \tag{2}$$

The standard deviation of the modulus of the KOP over time (i.e. $SD(\,abs(\mathrm{KOP}))_t$) is a measure of the metastability [44] . Therefore we describe the dynamics of the GWBM in terms of global metastability, $SD(R)_t$, and local metastabilities, $SD(r_n)_t$.

3.2.2 Scenario 1: Ensembles with homogeneous local couplings

In the first simulation scenario, we searched for optimal global parameters (global coupling, and spike-propagation velocity), while we held the local coupling identical for all ensembles (the local coupling will be optimized in the second scenario, during which the global parameters are kept at the levels determined by this first scenario). We assumed a

constant spike-propagation velocity and time delays proportional to the Euclidean distance between nodes. The optimal parameters were found by two independent stochastic optimizers (particle swarm optimization, PSO; and adaptive differential evolution, aDE). The fitness function of the optimizers maximized the correlation between simulated and MEG sFC in the alpha band, while it was constrained to biologically plausible solutions (see sections *Fitness function*, and *Optimization constraints*). sFC was measured as the correlations of the low-pass filtered ampliude envelops of the analytic alpha band signals. The optimal solutions had a correlation of ~0.55 between simulated and MEG sFC (Figure 1). The optimal global parameters of the two optimizers were identical up to the second decimal point.

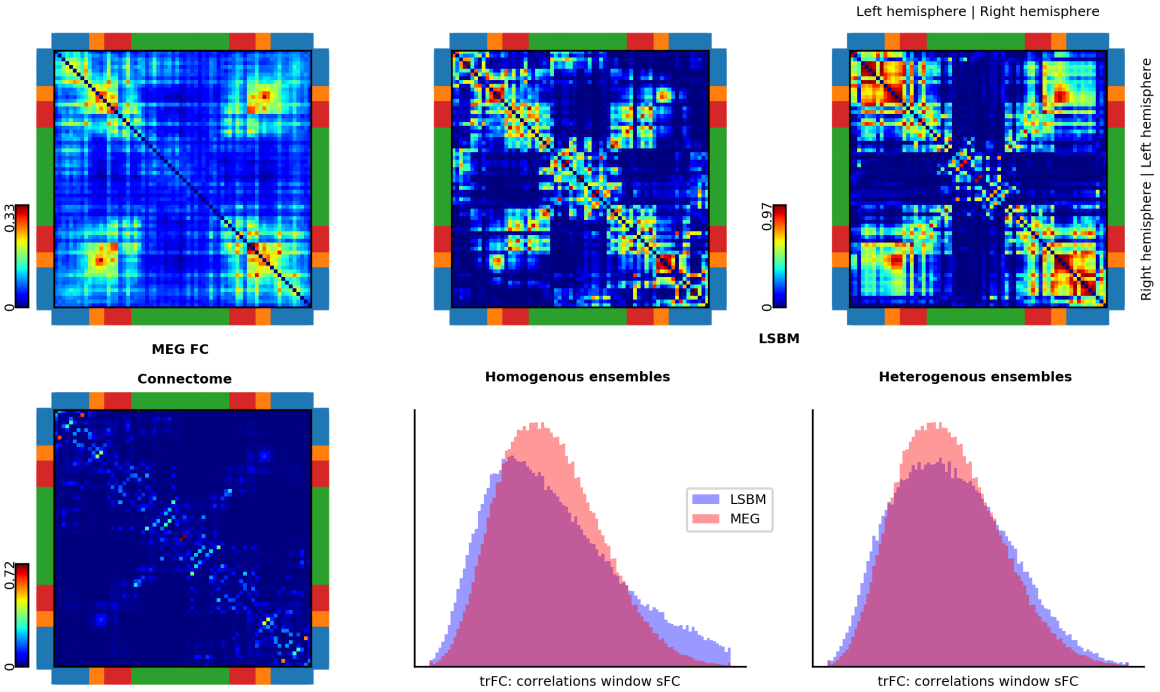

Figure 1. *Connectome and FC from real MEG data and from simulations. First column shows resting-state MEG static FC (orthogonalized alpha band envelope correlations, top), and the anatomical network or connectome (bottom). The second and third columns show the FCs obtained from simulations with homogeneous and heterogeneous ensembles, respectively. The top row shows the static FCs. The bottom row shows the histograms of time-resolved FC recurrence (trFC: correlation of static FCs for 15 sec. moving window with 12 sec. overlap) for simulation (blue) and MEG data (pink). Brain lobes are color-coded around the connectivity matrices – blue, temporal; orange, occipital; red, parietal; and green, frontal.*

Figure 2 shows that FC emerges when the local coupling is below the critical coupling, L^c. Being below L^c would lead to asynchronous ensembles if they were decoupled from the rest of the brain. However, when there are between-ensemble interactions, the local synchrony can increase. Suitable local and global couplings have a negative correlation. The global coupling increases as the local coupling decreases. Moreover, Figure 2 shows that time-delays are needed to reproduce sFC.

A GWBM parametrized within the same range but without time delays leads to full global synchrony (R ~ 1) and steady partial local synchrony ($0 < r_n =$ constant < 1) proportional to the coupling strength with other ensembles. On the contrary, a GWBM with long time delays becomes globally asynchronous with steady partial local synchrony. This is consistent with previous results obtained analytically in a model with homogeneous couplings [45].

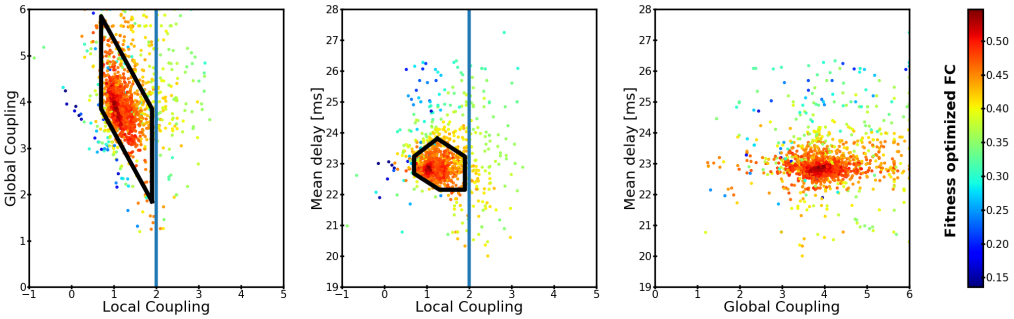

Figure 2. *Similarity between simulated and MEG sFC during the optimization with homogeneous ensembles. Each dot represents the correlation between simulated and empirical MEG sFC during one evaluation of the fitness function. A three-dimensional parameter space consisting of global coupling, local coupling, and mean delay (proportional to spike-conductance velocity) is optimized for reproduction of the empirical sFC. Each panel has one dimension collapsed over the two axes. Simulations outside of the optimization constraints are not shown. The black area indicates the area of the parameter space that is further analyzed for trFC. Only the parameter combinations which produced dynamics within the biological constraints are shown.*

Global and local metastability are relatively high, but not maximal, in the area that better predicts FC (see Sup. Fig. 2). The highest global metastability appears to be above L^c, although the simulated sFC has low similarity with MEG sFC. The highest local metastability appears below L^c. In other regions of the parameter space both metastabilities tend to be lower than in the area that reproduces FC better. The averaged global and local

synchronies are moderately high and almost constant in the area that best predicts FC. Outside of this area, global and local synchrony either increases or drops abruptly (see Sup. Fig. 2).

Next, we evaluated the trFC within the area of the parameter space that reproduces sFC (black polyhedrons in Fig. 2). trFC was measured as the recurrence (Pearson correlation) of sFCs over a 15-second sliding window with 13 seconds overlap. Histograms of recurrence values were built for both simulated and MEG data. The similarity between these two histograms was measured with the Kolmogorov-Smirnov distance (KS-distance). The parameters that best predicted 300-second sFC and trFC simultaneously were associated with the highest concurrent local and global metastabilities (Figure 3). The best trFC had a KS-distance of ~0.04, and the best sFC had a correlation of ~0.52. The Supplementary Figure 3 shows the trFC KS-distances and sFC correlations over the polyhedron in Figure 3. The global parameters that provided the best joint fit of sFC and trFC were used in the second scenario (this corresponded to: spike-conductance velocity ≈ 3.42 m/s, and global coupling ≈ 3.57; magenta arrow in Figure 3).

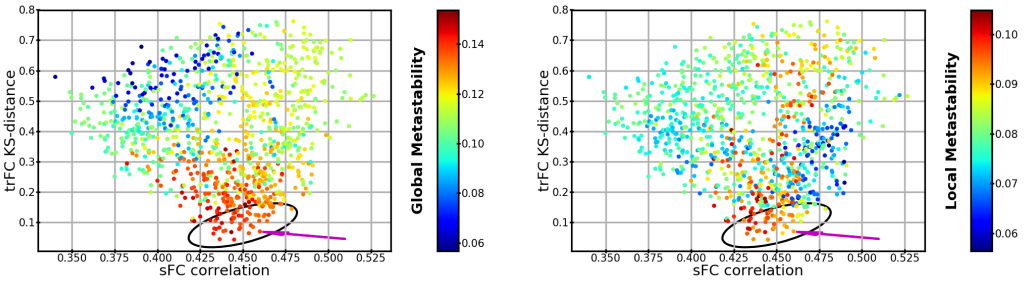

Figure 3. *Global and local metastability as a function of trFC and sFC similarity between 300-second simulations and MEG. Each dot has the same conventions as Figure 2, but the dots are arranged by similarity to trFC (KS-distance; y-axis), and similarity to sFC (correlation; x-axis). (Left panel) Dots are colored by their global metastability. (Right panel) Dots are colored by the local metastability averaged over ensembles. The black ellipsoid marks the areas that provide a good compromise between trFC and sFC fit. Magenta arrows indicate the simulation from which we took the global parameters for the second scenario.*

A simulation with a good fit to MEG (Figure 3; magenta arrow) is shown in Figures 1 (sFC and trFC) and 4 (time-courses of synchrony and power spectra). The power spectra shows the central frequency of each ensemble. However, the power density at the microscopic level would be broader than in Figure 4 (except if $r_n = 1$) because the GWBM reduces a

probability density of frequencies to its mean-field frequency. It is a non-trivial task to obtain the individual frequencies that contribute to the mean-field frequency. Local synchrony fluctuates at different rates at each ensemble. These fluctuations are not strictly periodic because they do not have a constant frequency. Nevertheless some regularities are visible at different time scales within and between ensembles. The global synchrony has large fluctuations as well. These aperiodic but temporally structured fluctuations at both spatial scales resemble metastable dynamics. The first 20 seconds of simulation correspond to the initial transient dynamics that were not included in the FC.

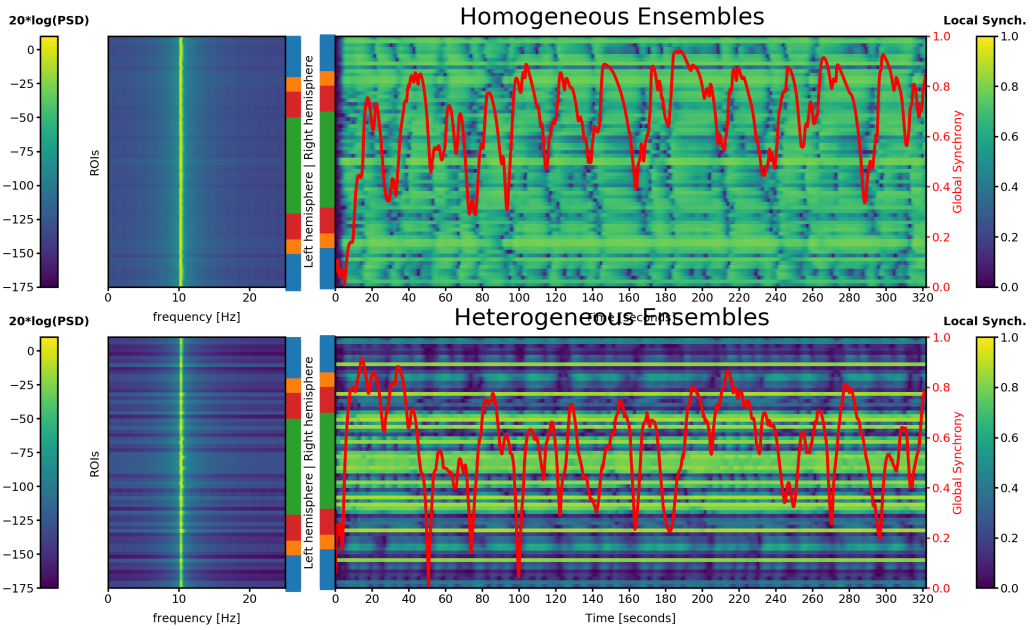

Figure 4. *Power spectral density (PSD) and temporal evolution of local synchrony in each ensemble, overlaid with the level of global synchrony. Top: GWBM with homogeneous ensembles; Bottom: GWBM with heterogeneous ensembles. Each horizontal line reflects the ensemble that represents one brain region. The lobes are color-coded using the same conventions as previous figures. The left panel shows the power spectrum of the central frequency from the probability density of frequencies. The right panel shows the temporal evolution of local (within-ensemble) synchrony in yellow-blue color. The global synchrony (between-ensembles) is represented in red (right, y-axis).*

3.2.3 Scenario 2: Ensembles with heterogeneous local couplings

Having established the global parameters of our GWBM, we then turn to the scenario in which local couplings can differ between ensembles. Here, the optimizers identified the local couplings that reproduced sFC, while the global parameters were kept constant (derived from the first scenario). To reduce the dimensionality of the parameter space, we assumed equal local couplings in homotopic ensembles as the sFC and the anatomical networks are almost symmetric respect to the interhemispheric fissure.

PSO and aDE achieved a maximal correlation between simulated and MEG sFC of 0.80 and 0.78, respectively. The optimal parameters found by each optimizer were not identical (0.81 correlation & 0.84 cosine similarity), and neither were the sFCs generated (0.90 correlation & 0.94 cosine similarity). Supplementary Figure 3 shows the local coupling parameters used in each optimization iteration sorted by the correlation with MEG sFC. Next, we looked at the 300-second sFC and trFC produced by the 1000 best solutions from each optimizer.

Figure 5 shows that the solutions with high similarity to MEG data tend to have high global and local metastabilities, although there are some differences in metastability for solutions with comparable fit to sFC and trFC (see later). The best fit to MEG trFC has a KS-distance of ~0.02, and the best correlation to MEG sFC is ~0.79.

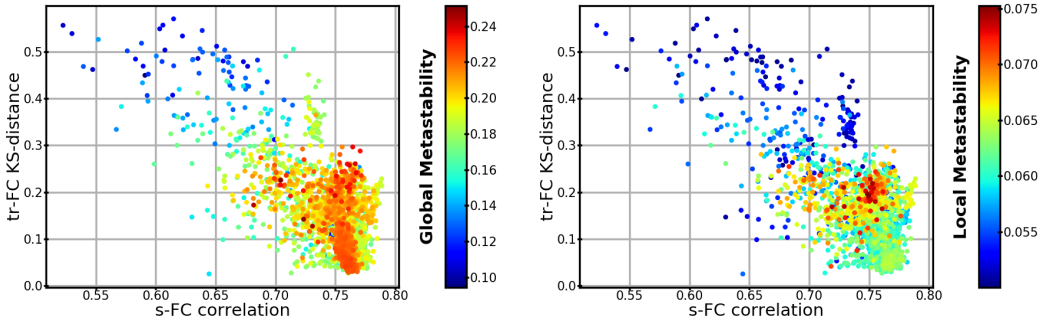

Figure 5. *Global and local metastability of heterogeneous ensembles as a function of trFC and sFC similarity between 300-second simulations and MEG for the best 2000 simulations. Each dot represents one simulation similar to Figure 3. (Left panel) Dots are colored by their global metastability. (Right panel) Dots are colored by their local metastability.*

Figure 6 shows in red the local couplings for the solutions that achieved the best compromise between sFC and trFC similarity to MEG data (correlation > 0.75 and KS-

distance < 0.04), a set of 49 solutions. There is not a unique combination of local couplings which predicts sFC and trFC. Some ensembles—such as the superior temporal or the inferior temporal regions—can take a wide range of local couplings, while others—such as the precuneus—work within a narrow range of local couplings. There are other ensembles like the parahippocampal area, the cuneus, or the posterior cingulate that can take local couplings from two disjoint sets of values. For example, the local couplings at the posterior cingulate group either around 6 or -3. Next, the local couplings at the posterior cingulate region were used to divide these 49 solutions into two groups. The group with local couplings above 2 is shown with the orange histogram in Figure 6. The solutions from each group had the local couplings reconfigured in a way that produced almost the same sFC and trFC.

The global metastability is significantly different (Mann-Whitney U test) between the groups separated by the local coupling at the posterior cingulate (p-value < 10^{-8}) as well as the local metastability averaged over ensembles (p-value < 10^{-6}). Such differences in metastability are also significant for solutions with sFC correlation higher than 0.7 and trFC KS-distance lower than 0.15. These differences are noticeable in Figure 6 as well.

Next, simulated local metastability was compared with local MEG metastability. Local MEG metastability for a particular brain region measured as the standard deviation over time of the envelope from the Hilbert transformed alpha band signals. Local metastability was measured in each participant independently, and subsequently averaged across participants. The group of solutions depicted in orange in Figure 6 had a median correlation of 0.13 between MEG and simulated local metastability, while the other group of solutions had a median correlation of -0.14. This shows that although FC is very similar for both groups of local couplings, the metastable dynamics can be quite different. In what follows, we will show only results from the cluster of local couplings which have a positive correlations with MEG data (orange histogram in Fig. 6).

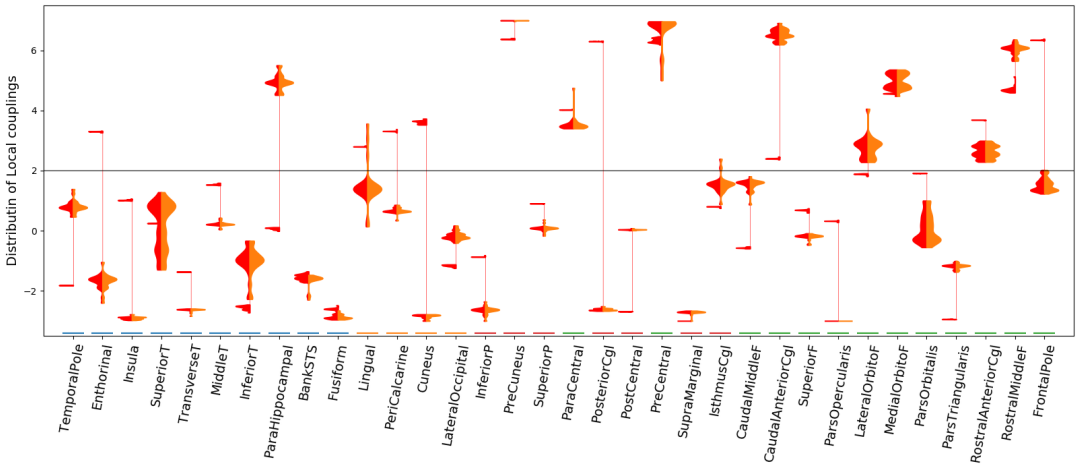

Figure 6, *Density estimates of local couplings by brain regions for the best solutions in terms of sFC and trFC similarity. Each column on the x-axis is a brain region. In each column, there are vertically two density estimates of local couplings with the value indicated by the y-axis. The densities on the left (red) contain the number of solutions that best predict sFC and trFC for a given local coupling (y-axis). The vertical thin red line connects clusters of solutions in the same brain region. The densities on the right (orange) are a subset of the local couplings of the densities on the left. This subset contains solutions from only one cluster of local couplings. The horizontal gray line indicates the critical local coupling.*

The local couplings have a significant negative correlation with the simulated nodal sFC strength (sFCS; average correlation of -0.46 and -0.40 for the right and left hemispheres respectively, p-values $< 10^{-5}$). The nodal sFCS is the sum of sFC in a node, so brain regions with high functional connectivity to other regions have high sFCS. Figure 7 shows that there is a general tendency of areas with high sFCS to have local couplings below the critical local coupling, L^c. In contrast, areas with lower sFCS have their local couplings either above or below L^c. There are a few exceptions to this, such as the precuneus or the parahippocampal which have relatively high sFCS and high local couplings, or the insula and the pars orbitalis which both have low local coupling and low sFCS. Simulated and MEG sFCS follow the same pattern except for some asymmetries between hemispheres. For example, the simulations show a strong sFCS asymmetry in the precuneus, and the isthmus cingulate which are not present in the MEG data. The local couplings were not correlated with the nodal connectivity strength of the anatomical network ($\rho < 0.07$ in right and left hemispheres).

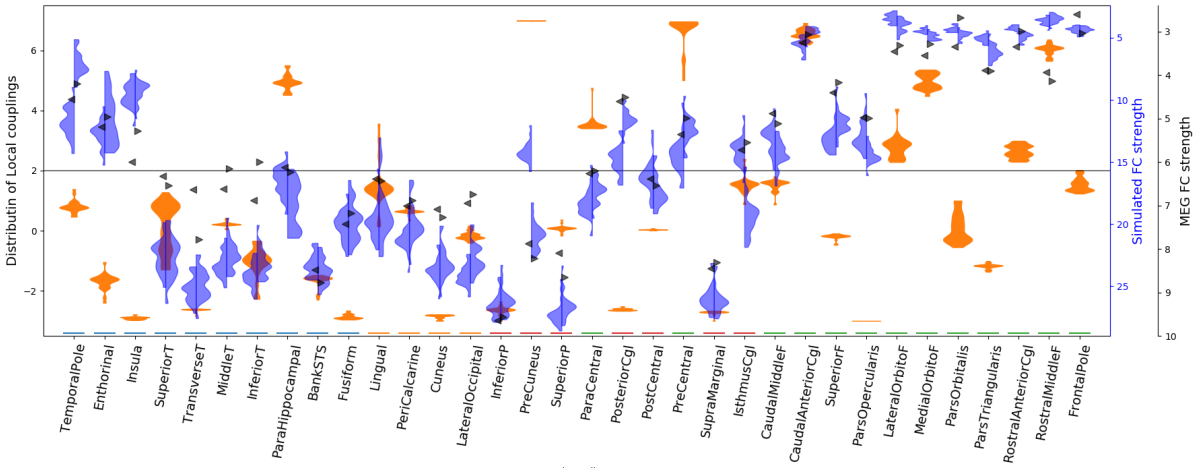

Figure 7, *Density estimates of local couplings and functional connectivity strength by brain region. Each column on the x-axis is a brain region. In each column there are: one two-sided density in orange, two one-sided densities in blue (left/right), and two arrows in black. The orange density contains the same local couplings that are shown in orange in Figure 6. The magnitude of local coupling is indicated on the left y-axis. Blue densities represent the sFCS for these local couplings, left and right for each hemisphere. The black triangles indicate the MEG mean sFCS across subjects for each hemisphere. Both scales of FCS are on the right y-axis with the respective colors. The scales of sFCS are inverted to aid visual comparison with local couplings as they have a negative correlation (-0.46 and -0.40 for the right and left hemispheres respectively). The horizontal gray line indicates the critical local coupling.*

The sFC and trFC of one these solution are shown in Figure 1, and the associated power spectra as well as the synchrony time courses are shown in Figure 4. Similar to the heterogeneous ensembles, there is a variety of short- and long lasting patterns of within- and between-ensembles synchrony that resemble metastable dynamics. However, in the model with heterogeneous local couplings there is higher variability of local and global synchrony than in the mode with homogeneous local couplings. The Supplementary Figure 7 shows the spectrogram of the solution shown in Figures 1 and 4.

3.3 Discussion

We have derived a parsimonious large-scale whole-brain model that is able to successfully simulate the dynamics of resting-state MEG functional connectivity in the alpha frequency band. This GWBM reconciles simplicity with biological interpretability and allows for the

manipulation of both local and global neural synchrony within one framework. Such modulations of synchrony are observed in neuroimaging data at multiple spatial and temporal scales, and are believed to be fundamental property of neural activity [1–3,5–8,18,25,27,46] Our model goes beyond traditional GWBMs that are not able to capture modulations of local synchrony [5,12,24]. Moreover, the tendency of each ensemble to de/synchronize can be adjusted with a single parameter that represents within-ensemble connectivity strength. Because local synchrony can be manipulated with one parameter, it is feasible to fit GWBMs with heterogeneous local synchronies and to analyse between-ensemble differences.

The proposed GWBM was able to simulate resting-state sFC and trFC of MEG alpha band envelopes in two scenarios. In the first scenario all ensembles were identical (homogeneous ensembles). In the other scenario each ensemble could take a different local coupling parameters (heterogeneous ensembles).

3.3.1 Scenario 1: Ensembles with homogeneous local couplings

The GWBM with identical ensembles showed that FC emerged when there were interaction delays between ensembles. This is in agreement with findings of previous GWBMs that relied on different reductions of neural activity [14,16,30,47] . Such interaction delays between ensembles of neurons are due to finite spike-conductance velocities along neural fibers [48,49].

Another consistent finding in GWBMs is that FC emerges when the dynamics of the ensembles are close to a critical point. Below this critical point, ensembles do not oscillate, but once the critical point is exceeded, the ensembles start to oscillate [11,26,27,41]. For example, a stability analysis of GWBMs with several reductions of neural activity showed that additive noise as well as delayed coupling with other ensembles induced oscillations and plausible patterns of resting-state sFC [41]; GWBMs based on Stuart-Landau oscillators reproduced sFC and trFC only when the ensembles were near a supercritical Hopf bifurcation [26,27]. Similarly, FC emerged in our GWBM if the local coupling was just below a critical local coupling, L^c. L^c was the minimum coupling required by an unperturbed ensemble to leave the desynchronized state. Below L^c the ensembles pushed towards local asynchrony while local couplings above L^c promoted local synchronization.

Ensembles that had low local coupling, reflecting desynchronization, were more sensitive to the phase of other ensembles, which facilitated between-ensemble synchrony. This increase of between-ensembles synchrony raised local synchrony, but local synchrony could not be maintained as between-ensemble synchrony was perturbed by interaction delays, and there was not enough local connectivity to sustain the synchrony from within

the ensemble itself. Therefore, the ensembles went into a state of fluctuating partial local synchronization that gave rise to FC networks.

We have shown that FC depends on a balanced interaction between the local coupling and the global coupling among ensembles. When the global coupling increased, the local coupling decreased proportionally. However, if only the global coupling increased, the GWBM became fully synchronized globally and locally (See Supplementary Figure 2) – a pathological state that occurs during epileptic seizures [50]. When only the local coupling decreased, the ensembles became asynchronous and the fluctuations of local and global synchrony stopped (See Supplementary Figure 2). In other words, in order to maintain the state of fluctuating partial synchrony responsible for FC, the ensembles counterbalanced an increase of attraction to global synchrony by decreasing local synchrony and vice versa. Hence, FC emerged from precise opposition between local attraction to asynchrony and between-ensembles attraction to synchronicity, the latter being perturbed by interaction delays. This relationship between local and global couplings suggest that the critical local coupling was shifted towards lower local couplings if the global coupling increased. Other GWBM have included a local feedback inhibitory control mechanism to counteract the increase of global coupling [51,52]. Feedback inhibitory control adapts the strength of recurrent inhibitory synapses to compensate for the increase in excitatory activity due to long-range connections with other ensembles. Feedback inhibitory control increased the predictability of FC for spontaneous and evoked activity [51,52].

Interestingly, FC was reproduced when high metastability (fluctuations of synchrony) coexisted at global and local scales. Metastability is a hallmark of brain dynamics and it occurs at multiple spatial scales. Metastability allows to simultaneously integrate and segregate information [21,46]. Metastable dynamics are believed to provide the neural flexibility needed to adapt and respond fast as well as to maintain current states like memories [46,53]. Because previous GWBM could not capture fluctuations of local synchrony [5,12,24], they reported only high global metastability without corresponding local metastability [15,26,27]. In contrast, our GWBM showed maximal global metastability when local metastability and the fitness to sFC were low. This suggest that accounting for fluctuations of local synchrony – local metastability – might be necessary for successfully modeling large-scale brain networks.

3.3.2 Scenario 2: Ensembles with heterogeneous local couplings

The GWBM with heterogeneous ensembles allowed for ensembles which could promote local synchrony or aynchrony at various levels. This model simulated FC with higher accuracy than the model with homogeneous ensembles. This was not entirely surprising given that the model with heterogeneous ensembles had 34 parameters to tune local dynamics compared to a single parameter in the model with homogeneous ensembles.

More interestingly, the plausible local couplings of each ensemble exhibited different distributions, including bimodal distributions. This suggests that there is not a single way to generate a particular target FC, but instead it can be generated by multiple different configurations of local dynamics. Such pattern points at an adaptive property of the brain, which can function in a number of different states, thereby making it resilient to perturbations. A similar effect is observed at a lower scale as the same macroscopic activity can be obtained form a network of neurons with different synaptic strengths [54].

The local coupling had a negative correlation with the sum of nodal sFC strength (sFCS). In other words, ensembles with lower local couplings (below L^c) had a tendency to higher sFCS, and vice versa. Similar to the GWBMs with homogeneous ensembles, the balance between the local tendency towards asynchrony and the time-delayed between-ensemble synchrony gave rise to fluctuations of local synchrony and FC. In contrast, ensembles with high local couplings (above L^c) had a tendency to synchronize locally and did not engage into coordinated fluctuations of local synchrony, i.e. FC. Such ensembles were more attracted to local than between-ensemble synchrony. Nevertheless, they had strong influence on other ensembles driving ensembles with low local coupling. Some exceptions to this observation were ensembles that belong to the default-mode network, such as the precuneus or the parahippocampal areas [55], which tended to have high local couplings and relatively high FC as well. Such high local coupling may reflect a state of high local coupling and low excitability that allows for maintaining the local dynamics in the face of external disturbance. Future research should investigate these individual differences in dynamics between the different ensembles.

In the simulations there were ensembles with asymmetric sFCS between hemispheres which were different from the MEG sFCS asymmetries (e.g. the precuneus). These discrepancies might be due to the assumption of equal local coupling at homotopic brain regions. To our knowledge there is only one study so far which has attempted to optimize all cortical brain regions in a GWBM [27]. This study showed that some homotopic brain regions had different parameters. However it is not possible to compare parameters systematically across studies because the topologies of the FC are considerably different and the neuroimaging technologies are different (FC in [27] included frontal but not occipital regions and it was measured with fMRI). Although the assumption of homotopy reduced our ability to fit the functional data, we decided that this was the best trade-off between model complexity and model fit.

3.3.3 Optimization framework

While we have argued that a multimodal distribution of plausible local couplings can have reasonable biological underpinnings, there exist other plausible explanations. First, it could be that the optimizers explored two local optima, but they failed to find a global optimum.

It is known that stochastic optimization does not guarantee finding a global optimum. However, we think this explanation is unlikely because we have obtained similar results in multiple runs of different optimizers. It is therefore likely that there were two global optima.

Second, we used sFC and trFC to assess the similarity between simulations and MEG data. The fitness function of the optimizers only evaluated the similarity of sFC, but this was sufficient to predict trFC with high precision. However local and global metastability were different among the two clusters of local couplings. Adding local information to the fitness function might help to constrain the solutions of the optimization. Here we focused on optimizing FC as this is the most common approach on the literature. Moreover, we find relevant the fact that similar FC could emerge from different local dynamics. This might contribute to explain the variability in neuroimaging measurements between and within-subjects during-resting sate as well as behavioral tasks.

Third, not all optimizers were able to find suitable solutions. For example a successful optimizer on similar problems (covariance matrix adaptation evolutionary strategy [56]) was not able to find proper solutions in this context, while aDE and PSO worked satisfactorily. aDE and PSO found similar solutions, although they relied on different heuristics. These heuristics were noticeable in their evolution towards the best solution. PSO was more exploitative, while aDE was more explorative. PSO found a good set of parameters fast, and then restricted exploration near these parameters. On the contrary, aDE favored diverse combinations of parameters, but took longer to find a good set of parameters. Given the dissimilar behavior of the two optimizers, a further improvement could be to try other algorithms or to migrate solutions between optimizers. Strategic migrations of parameters tends to improve the optimization[57]. However, this enhancement might not avoid converging to local optima, nor may it improve the similarity between simulated and MEG data. Recently an optimization approach based on Bayesian Gaussian-process optimization gave remarkable results in a GWBM with a 5-dimensional-parameter space with less computing time [16]. Further research on this framework with higher-dimensional-parameter spaces could fuel the usability of GWBM.

3.3.4 Limitations and extensions

In this GWBM we made several assumptions and choices that might influence the results. First, we imposed a network-of-networks structure where the higher level nodes represent ensembles of neurons in each region of a cortical parcellation. The parcellation scheme determines the number of brain regions, their size, and the topology of the anatomical network that connects the ensembles. This should be taken into account when interpreting or comparing the results with other studies. Moreover sub-cortical structures were not included, although synaptic noise in the thalamus has been related with multistable changes

of alpha band amplitude [58]. The study of such noise-driven changes of amplitude was limited to a single region, but sub-cortical structures might be relevant for faster changes on FC and enhanced metastability.

To derive the model we assumed that each ensemble is a fully connected network. This assumption could be relaxed. A similar model to ours that contained random Erdös-Réniy topologies at the ensembles showed analytically and numerically that the same synchrony states are achieved with a shift in the coupling parameters proportional to the average degree of the networks [59]. Manipulating the topology of the connectivity of the ensembles might be useful to understand its impact on FC [60]. Moreover topological manipulations could contribute to understanding the effects of neurological disorders and different kinds of brain damage arising from natural causes or surgical interventions [19,60]. For example, GWBMs with a network-of-networks of Kuramoto oscillators have previously been used to understand abnormal neural synchrony [20,37,38]. These studies found, for example, that hyper-synchronous activity was found to emerge more easily from structurally central regions and when neural fibers had altered properties [38]. In addition, they demonstrated that hyper-synchrony can emerge more easily form the resting-state FC of epileptic patients [20,37], although these studies used the network of FC to couple the ensembles instead of the network of neural fibers. A network-of-networks of Kuramoto oscillators is an effective method to derive analytically the features of the brain that allow specific patterns of FC [23].

Another local heterogeneity that could be introduced is a diversity of density distributions of natural frequencies. We assumed that all ensembles have identical distributions of natural frequencies. Nevertheless heterogeneous natural frequencies might be a relevant factor because it has been observed in EEG data that the alpha peak frequency differs between brain regions during resting-state and behavioral tasks [61]. Such difference infrequencies might perturb global phase synchronization on the same manner as time-delays.

One may argue that a limitation or virtue of this GWBM is that it models only one frequency band but not the whole power spectrum of MEG. Yet, MEG is typically analyzed in frequency bands which each seem to play distinct functional roles [3,5,7,25,62–64]. During behavioral tasks as well as resting-state each frequency band tends to produce a different FC pattern [3,7,64]. Moreover, behavioral studies analyze event related synchronization within one frequency band [5,25,65]. Therefore, this GWBM provides a simple framework for modeling single-frequency-band electrophysiological data. Additionally the mathematical framework of the GWBM allows for multimodal distributions of frequencies [66]. Here we focused on reproducing FC in the alpha band, but we hypothesize that FC could be reproduced in other frequency bands simply by shifting the distribution of natural frequencies to the same frequency band, as a Hopf bifurcation model has already demonstrated successfully [26].

We have shown that the GWBM reproduces not only static FC, but also time-resolved FC. However, time-resolved FC might be influenced by the length of the moving windows used to estimate short-lived FC states. We chose a conservative length of 15 seconds, which may have missed short-lived FC patterns [7].

Finally, we assumed that all neural fibers have the same spike-propagation velocity, and that the length of the neural fibers is the Euclidean distance between ensembles. However there is a broad range of possible velocities which depend on the physiological properties of the neural fibers [48,49]. Some of this variability could be incorporated in the GWBM by using a probability density function of time delays [67]. Furthermore, other simulation studies have shown that the density of inter-hemispheric neural fibers is underestimated, and better predictions of FC can be achieved by scaling the inter-hemispheric connections [16,17]. Additionally, we assumed that homotopic ensembles have the same local coupling to exploit the symmetries on the anatomical and FC networks as well as to speed up computations. Even though our results suggest that without this assumption the similarity between MEG and simulations could improve, we think that this assumption is a good compromise between model complexity, computational time, and explanatory power.

3.3.5 Significance

This study shows that resting-state MEG sFC and trFC emerge from the opposition between local asynchrony and global synchrony perturbed by interaction delays. Local asynchrony is facilitated by low local connectivity. Ensembles with low local connectivity adapt rapidly their phases to synchronize with other ensembles which suggest higher excitability. The increase of between-ensemble phase synchrony leads to higher local synchrony. However, between-ensemble synchrony is broken intermittently by the interaction delays, causing local synchrony to drop. These dynamics create coordinated fluctuations of local synchrony. The dynamics of the model are highly metastable at global and local scales when FC emerges. We also observed ensembles with high local connectivity which did not engage in FC, but still influenced the dynamics of ensembles that are responsible for FC. Parts of the default-mode networks show a differential behavior with high local coupling and strong FC.

We have presented a parsimonious large-scale brain model that balances simplicity and biological interpretability. Such a framework might contribute to determining the conditions and mechanisms that lead to the patterns observed in neuroimaging data. We have shown that this model can realistically simulate resting-state FC, and we hypothesize that it could be used to simulate changes in FC over a course of a behavioral task as well [3]. Moreover, our results suggest that modulations of local synchrony are fundamental for large-scale synchronization and FC. In the future we aim to use this model to understand which and how brain regions contribute to switch between transient functional connectivity networks

during a behavioral task, which will contribute to elucidate how cognitive functions can arise from specific patterns of functional connectivity.

3.4 Methods and Model

3.4.1 Modeling one ensemble of neurons

The GWBM presented here aims at describing the evolution of the neural synchrony in an ensemble of neurons (cortical region) with a temporal resolution similar to MEG measurements. Moreover the GWBM should have the same framework for local and global synchrony. The model should have only one parameter to tune local synchrony, but it should allow for incorporating other properties of neural ensembles. The model is motivated by recent findings showing that modulations of synchrony in an ensemble of neurons can be expressed in terms of the Kuramoto order parameter (KOP) [5,24,35,36].

In our GWBM the neural activity within an ensemble of neurons is describe by the KOP, and the KOP is obtained form a network of Kuramoto oscillators [33,34]. Kuramoto oscillators can describe many synchronization phenomena observed on neural ensembles [31,32]. The KOP is a complex number with the modulus bounded between zero and one. When the modulus of the KOP, r_n, is zero the neurons fire asynchronous, so the total electric potential produced is minimal. When the modulus of the KOP is equal to one, the neurons fire in a fully synchronized manner, resulting in a maximal electric potential.

3.4.2 Modeling a network of ensembles of neurons

In a GWBM an ensemble of contiguous highly connected neurons – a brain region – is typically represented as a node in a fixed network whose edges are neural fibers. The set of edges connecting pairs of ensembles of neurons form a heterogeneous weighted multigraph. One weight of the multigraph is proportional to the density of neural fibers, A. The second weight of the multigraph represents the distance between the ensembles, D. This distance might impose time delays in the interaction between ensembles due to finite spike-conductance velocities [48,49]. At the ensemble level – sub network – it is reasonable to assume that the interaction delays are negligible and the neurons are fully connected. In this way, the brain model becomes a network-of-networks. The section *Anatomical network of neural fibers* has more details about computing the multigraph of neural fibers.

The KOP for each ensemble of neurons was derived with a mean-field reduction in a network-of-networks of Kuramoto oscillators. To enforce such structure, the couplings within-ensemble were instantaneous, and identical, while the couplings between ensembles were delayed and weighted by the multigraph of neural fibers. In addition, the couplings within-ensemble were much larger than the couplings between ensembles. Kuramoto

models with a network-of-networks structure have been studied previously [20,23,45,59]. We used a Kuramoto model and a mean-field reduction similar to the one analyzed by Skardal et al. [45,59]. The mean-field reduction is based on the Ott-Antonsen ansatz [42]. With this reduction the dynamics of each ensemble are given by the KOP ($KOP = r_n e^{i\psi_n}$). The temporal evolution of the KOP is dictated by equations 1a and 1b in the results section (S15a and S15b in the Supplementary information). In total the GWBM consists of E complex delayed differential equations where E represents the number of ensembles (brain regions). The Supplementary information provides all the mathematical details needed to derive the GWBM.

3.4.3 Model parameters

Some parameters of the GWBM can be given beforehand, while others should be estimated. The natural frequencies on the ensembles were set beforehand by a Lorentzian distribution function with center frequency Ω and spread Δ. We limited our simulations to the alpha frequency band, and we assumed the same distribution of frequencies for all ensembles (Ω = 10.5 Hz; Δ = 1). We chose this range for three reasons. First, other MEG resting-state studies have reported significant FC in this band [7,64,68,69]. Second, earlier GWBMs have shown high correlation of simulated and empirical sFC in alpha band [17,26,47]. Third, the MEG used on this study had relatively higher power in the alpha band compared to other bands (See Supplementary Figure 6)

Other parameters were estimated with stochastic optimizers – the global coupling among ensembles, G, the local coupling within each ensemble, L_n, and the spike-propagation velocity, v. The spike-propagation velocity and the distance between ensembles determined the interaction delays, $\tau_{ee'}$. A constant spike-propagation velocity was assumed for simplicity. However, neural fibers have a wide range of spike-propagation velocities [48,49]. Nonetheless most GWBM either neglect time delays or assume a constant velocity as well. These parameters were estimated because they have a large impact on the dynamics of GWBMs [15,16,30,47].

3.4.4 Simulation scenarios and parameters estimation

The GWBM was evaluated in two scenarios. The first scenario assumed that all local couplings were identical (heterogeneous ensembles), resulting in *3* free parameters (spike-propagation velocity, global coupling, and one local coupling for all ensembles). Studies with GWBMs often assume identical ensembles, hence this scenario is similar to previous literature. In the second scenario the local couplings were free to vary across ensembles (heterogeneous ensembles), while the global parameters were fixed from the first scenario (spike-propagation velocity, and global coupling). The second scenario assumed that

homotopic ensembles in the left and right hemisphere had identical local couplings, thus having *E/2* free parameters. This assumption reduced the parameter space, as well as the computing time, and it exploited the symmetries in the model. The multigraph of neural fibers and the MEG sFC are almost symmetric with respect to the interhemispheric fissure (see Figure 2). The relatively small number of parameters allowed stochastic optimizers to efficiently identify the parameters that reproduced MEG sFC. Then, trFC was computed within the restricted area of the parameter space that reproduced sFC. Supplementary Figure 1 contains an schematic representation of the parameter identification process.

3.4.5 Fitness function

The fitness function of the optimizers assessed the similarity between the sFC of MEG data and simulated neural activity. Each evaluation of the fitness function included 20 runs of the GWBM with identical parameters but different initial conditions (phases, ψ_n, but not r_n). The initial phases were drawn from a uniform distribution in the range [$-\pi$ to π) at the beginning of the optimization and kept across iterations of the optimizers. The initial r_n of each ensemble was set to its equilibrium point, r_n^{eq}, if the ensemble was detached from other ensembles ($r_n^{eq} = \sqrt{1-2\Delta/L_n}$). Multiple initial conditions were used to avoid overfitting of parameters to one set of initial conditions, which improves the chances of generalizing the results. Moreover, using multiple initial conditions allows for evaluating the effect of the initial conditions on the simulated FC (Supplementary Figure 5). These initial conditions might be interpreted as the previous state of the system.

The sFC from each run of the GWBM was obtained in the same way as the empirical MEG except for the orthogonalization step. Simulated data were not orthogonalized because there is no source leakage in the simulation. Another reason for not orthogonalizing was that the simulated data often were not normally distributed, which is a necessary condition for successfully applying orthogonalization [70]. Nevertheless we checked that simulated FC was not driven by zero-phase synchronization. Simulated neural activity was the imaginary part of the KOP. The same projection to neural activity has been used in prior GWBMs [15,26,27]. The median sFC across the 20 runs of the GWBM was compared with the MEG sFC by calculating the correlation between the upper triangular elements of the sFC matrices. The section *MEG and simulated data processing* provides more details on data processing.

3.4.6 Optimization constraints

The optimizers were constrained to biologically plausible solutions. These constraints prevented the GWBM from being either fully synchronized or incoherent, and enforced a minimal metastability. Full synchrony and incoherence are biologically implausible because low global synchrony appears during unconscious states [71], while high global synchrony

appear during epileptic seizures [20,50]. In addition, previous studies have shown that during resting-state there is high metastability [15,21,27]. The constraints were derived from the global synchrony (Eq. 2) averaged over time, $\langle R \rangle_t$, the global metastability, $SD(R)_t$, the average of local synchrony over ensembles and over time, $\langle \langle r_e \rangle_E \rangle_t$, and the average local metastability over ensembles $\langle SD\left(r_n\right)_t \rangle_E$. The median of these metrics across the 20 runs of the GWBM in one iteration had to comply with:

- $0.25 <$ median($\langle R \rangle_t$) < 0.8,
- $0.05 <$ median($SD(R)_t$),
- $0.25 <$ median($\langle \langle r_n \rangle_E \rangle_t$) < 0.8,
- $0.05 <$ median($\langle SD\left(r_n\right)_t \rangle_E$)

Solutions outside these constraints were heavily penalized to guarantee that the same set of parameters was not chosen again. These boundary values were selected based on visual inspection of model behavior.

3.4.7 Stochastic optimization algorithms

The optimization was carried out by three independent stochastic sampling algorithms. Several algorithms were used to examine the reproducibility and stability of solutions, and to avoid that a particular optimizer could not handle the optimization. Stochastic sampling algorithms are especially useful for complex global optimization problems in which the fitness function cannot be treated analytically. The fitness function is treated as a black box, although it is not guaranteed to find a global optimum. Nevertheless, a single best solution was not taken, but rather a range of optimal solutions which were used to evaluate trFC later.

The optimization algorithms used were – self-adaptive Differential Evolution (aDE), Covariance Matrix Evolutionary Strategy, and Particle Swarm Optimization (PSO) [56,57,72]. These algorithms are generally successful in solving benchmark problems that include features of our problem like a high-dimensional parameter space, a non-separable function and a non-linear function [57,72–75]. Other features like the shape of the cost function could not be obtained beforehand, although the chosen algorithms can cope well with unimodal and multimodal functions [57,72–75]. More information about these algorithms can be found in other sources [56,57,72,73]. The algorithms were implemented with the toolbox pagmo version 2.7 [76] in Python programming language. The 1220DE flavor of the aDE algorithm was used with all mutation variants and the iDE adaptation

scheme. We opted for this algorithm because it has several parameters that are self-adapted to the features of the cost function. The parameters of the other algorithms were set to their default values, which align with the values recommended in the literature [56,57,72,73]. In the first scenario the optimizers had a population of 20 individuals and 200 generations. Each individual consisted of one set of candidate parameters for which the fitness functions were evaluated. The generations are the number of iterations of the algorithm. The optimizers on the second scenario had 110 individuals and 250 generations. The Covariance Matrix Evolutionary Strategy exhibited very poor performance, and therefore it is not reported further.

3.4.8 Model simulations

Numerical simulations of the GWBM were carried out using the time-delayed first-order Euler method. The integration step size was set to 0.001 seconds. Because of the time delays, a history of initial values was simulated independently for each ensemble from the longest time delay to the initial simulation point. Then, simulations were run for another 66 seconds in the fitness function, or 321 seconds when trFC was computed. In both cases, the first 19 seconds were discarded to remove the initial transient dynamics. The first and last second of the remaining time were discarded after filtering and Hilbert transforming the simulated neural data in order to avoid edge artifacts. In total 45 seconds were used to compute sFC in the fitness function, and 300 seconds were used for computing trFC. We kept the simulation time as short as possible to reduce the total optimization time. The model was implemented in Python. The fitness function was compiled and parallelized with Numba. One evaluation of the fitness function for one individual (i.e. 20 GWBMs, one for each of the initial conditions) took approximately 7 seconds. The 20 GWBMs in the fitness function were parallelized over 20 nodes in a computing cluster. In total one optimizer in the first scenario took approximately 8 hours. One optimizer in the second scenario took approximately 70 hours.

3.4.9 Search of time-resolved functional connectivity

trFC was searched within the range of parameters that adequately reproduced sFC. In the first scenario, trFC was evaluated within the polyhedron of parameter space defined by black lines in figure 3. A total of 1000 models were evaluated with parameters randomly taken from the optimal polyhedrons. To obtain the random parameters, first, the velocity-local-coupling polyhedron was subdivided into triangles which were uniformly sampled relative to their areas. Next, a global coupling parameter was uniformly sampled from the range of possible values given the local coupling drawn before. The polyhedrons were defined by hand to capture the set of solutions with higher sFC similarity to MEG while remaining within the biological constraints. The polyhedron approach reduced the number of trFC simulations need to cover the parameter space. Each combination of parameters

was simulated 30 times with different initial phases. The initial phases were different to the ones used during the optimization. trFC as well as sFC were computed over 300 seconds of simulated data in the same way as MEG trFC and sFC. A similar approach was followed in the second scenario, apart from the polyhedron approach. In the second scenario trFC and sFC were simulated with the best 1000 parameter combinations found by each of the optimizers (2000 combinations of parameters in total). The similarity between simulated and MEG trFC was measured by the Kolmogorov-Smirnov distance between the recurrence histograms of simulated and MEG data. Similar approaches have been used before to assess the similarity of trFCs in GWBMs [26,27].

3.4.10 Analysis of MEG and simulated data

The MEG resting-state datasets (300 seconds, eyes open) of 55 healthy participants, previously acquired as part of the UK MEG partnership [7,77], were used in this work. For each participant, the data were downsampled to 250Hz using an anti-aliasing filter; high-pass filtered to remove low-frequency variations below 1Hz; source-reconstructed in MNI 8mm standard space using LCMV beamforming [78] (see [77] for further details about the pre-processing). Summary time-courses were subsequently computed within each of the 68 regions of the Desikan-Killiany cortical parcellation [79] using PCA, while preserving the relative variances between regions, and signal leakage was mitigated using symmetric multivariate leakage correction [80]. To compute FC in alpha-band, the orthogonalized time-courses were band-pass filtered between 8-13Hz, their Hilbert envelope was then low-pass filtered above 0.5 Hz and downsampled to 5 Hz. Pairwise Pearson correlations between regions were computed between downsampled envelopes to obtain sFC. trFC was computed over sliding widows of 15 seconds with an overlap of 12 seconds. Within each window sFC was computed. Recurrence of sFC within-subjects was measured by the Pearson correlation between the upper diagonal elements of the sFCs for each pair of windows. Finally, a histogram of sFC reoccurrences was built. Supplementary Figure 6 shows the time-frequency spectra of broad-band and alpha-band MEG activity.

3.4.11 Computation of the anatomical network

The anatomical network was computed by averaging the results of probabilistic tractography [81,82] on 10 diffusion datasets from the Human Connectome Project [83,84] parcellated into 68 cortical regions (34 per hemisphere) using the Desikan-Killiany cortical parcellation [79]. The FSL tool ProbTrackX [85,86] was used to compute 1000 probabilistic streamlines starting from each brain voxel, and ending at the boundary between white-matter and grey-matter (WM/GM) as defined by the CIFTI format [87]. For connectivity strength between any two regions A and B was computed by dividing the number of streamlines connecting A and B, by the total number of streamlines reaching A or B (so-

called fractional-scaling [88]). The resulting connectivity matrix was made symmetric by averaging with its transpose, and rescaled to have an average degree of 1. Then the connectivity matrix was normalized to have average edge weight equal to one. Finally, Euclidean distances were computed between the barycentre of each region in order to estimate the delays between them.

3.5 Supplementary Information

3.5.1 Motivation to use the Kuramoto order parameter to describe neural synchrony.

Our GWBM is motivated by previous work which has derived exact dynamical equations for the aggregated activity of an ensemble of neurons in terms of the average firing-rate and average membrane potential using mean-field reductions from a specific set of neuron models [5,24,35,36]. A mean-field reduction allows for the simplification of the dynamics of a large number of interacting elements, in this case neurons, with a few macroscopic variables, in this case membrane potential and firing-rate. In contrast to the previous neural-mass reductions (see [12,89] for more details on neural-mass models), this mean-field reduction provides an exact bridge between the microscopic properties of individual elements and their macroscopic collective properties. For this reason, neural mean-field reductions of this sort have been referred to as 'Next generation neural mass models*' [24]*.

Here we outline briefly the mean-field reduction of Montbrio et al. [35]. This reduction uses a quadratic integrate-and-fire (QIF) neuron model as elementary unit. It does however not rely crucially on this particular neuron type since similar reductions have been done with a theta neuron model [5,24,36]. The macroscopic membrane potential and the firing-rate of an ensemble of neurons are obtained from a heterogeneous all-to-all-connected population of QIF neurons. This reduction is exact in the thermodynamic limit, i.e., when the number of QIF neurons is infinite. The method and the steps to obtain the macroscopic variables are not within the scope of this paper, but can be found in Montbrio et al. [35]. Next we summarize this procedure.

The QIF neuron is a class I neuron model derived to simplify the Hodgkin-Huxley neuronal model. Class I neuron models go from quiescence state to periodic firing when the input current is increased, and the neuron passes through saddle-node bifurcation. The state of a QIF neuron, *j*, is given by an ordinary differential equation of its membrane potential, V_j.

$$\dot{V}_j = V_j^2 + I_j, \ \textit{if} \ \ V_j \geq V_{th}, \ \textit{then} \ V_{8r} \rightarrow V_j \tag{S1}$$

The overdot represents the temporal derivative. I_j represents a trans-membrane input current. When the membrane potential reaches a threshold V_{th}, the neuron emits a spike and

the membrane potential is reset to a resting value V_r. The trans-membrane input current has the form

$$I_j = \eta_j + Js(t) + I(t) \quad \text{(S2)}$$

, where η_j is a constant external current, *I(t)* is a time varying input current common to all neurons, *J* is a synaptic weight, and *s(t)* is the mean synaptic activation.

Montbrio et. al. [35] demonstrated that the macroscopic dynamics of a fully connected ensemble of neurons in the thermodynamic limit follow exactly two ordinary differential equations in which *f* represents the firing-rate and *v* the average membrane potential.

$$\dot{f} = \gamma/\pi + 2fv \quad \text{(S3)}$$
$$\dot{v} = v^2 + \bar{\eta} + Jf + I(t) - (\pi f)^2 \quad \text{(S4)}$$

The heterogeneity of the external currents is represented by a Lorentzian distribution with half-width at half-maximum γ and maximum peak at η.

Furthermore, Montbrio et al. [35] demonstrated that the macroscopic dynamics of the ensemble can be simplified further with a conformal mapping to the Kuramoto order parameter (KOP), *z*. Note that other mean-field reductions with the θ-neuron model can be mapped to the KOP as well [5,24]. This mapping has the form of

$$z = \frac{1-w}{1+w}, \quad w = \frac{1-z}{1+z}, \text{ where } w \equiv f\pi + iv, \text{ and } z = r e^{i\psi} \text{ with } r = [0,1], \text{ and } \psi = [-\pi,\pi]. \quad \text{(S5)}$$

In the above equation, the asterisk denotes the complex conjugate. In our GWBM we use the KOP as the descriptor of the neural activity in an ensemble of neurons, although the dynamics of the KOP are not given by the equations of Montbrio et al. [35].

3.5.2 Derivation of the GWBM equations

For the sake of simplicity we obtain the KOP from a fully connected network of Kuramoto oscillators [33,34] instead of equations 3S, 4S, and 5S. The Kuramoto model has been widely studied theoretically and it has also been applied to many biological examples of collective synchronization [34]. In a Kuramoto model the synchronization is controlled by a coupling parameter. Natural frequencies are drawn form a probability distribution *g(ω)* and initial phases are drawn from a uniform distribution (*r = 0*). When the coupling is low, each oscillator follows its own natural frequency. When the coupling increases above a critical value the oscillators began to synchronize. As the coupling continues increasing their synchrony increases until they reach full synchrony if the coupling continues increasing.

Next, we derive the equations of the GWBM. We consider a network with E ensembles labeled $n = 1,2, \ldots E,$ where ensemble n contains N_n oscillators $\theta_n^i(t)$ with $i = 1,2, \ldots N_n$. Pairs of ensembles, n and p, are coupled through the anatomical network A_{np} (the connectome), likewise, τ_{np} represents the time delays between the same pair of ensembles. The coupling between all pairs of ensembles is scaled by a global coupling G. The global coupling is scaled by 1/E, in order to impose community structure with stronger local than global coupling. Local couplings, L_n, determine the coupling within each individual ensemble of oscillators. The local couplings allow us to manipulate the synchrony within each ensemble. For simplicity, the anatomical network A, the global coupling scaling factor G/E, and the local couplings L_n are embedded into an $E \times E$ coupling matrix K_{np}. The diagonal elements of the matrix K_{np} contain the local couplings L_n. The off-diagonal elements of K_{np} contain the values of the anatomical network A scaled by the global coupling scaling factor G/E. The natural frequencies of the oscillators in each ensemble are drawn from different probability distributions. The distribution of natural frequencies in one ensemble is denoted by $g_n(\omega)$, and the natural frequency of one oscillator in the same ensemble is ω_n^i. With the previous definitions, the evolution of oscillator i in the ensemble n follows the next delayed differential equation.

$$\dot{\theta}_n^i = \omega_n^i + \sum_{p=1}^{E} \frac{K_{np}}{N_p} \sum_{j=1}^{N_p} \sin\left(\theta_p^j(t-\tau_{np}) - \theta_n^i(t)\right) \tag{S6}$$

We are interested in describing each ensemble by the KOP introduced in equation S5. The KOP in an ensemble of oscillators can be defined as follows [33]:

$$z_n = r_n e^{i\psi_n} = \frac{1}{N_n} \sum_{i=1}^{N_n} e^{i\theta_n^i}, \tag{S7}$$

where r_n and ψ_n represent the average phase coherence and the mean phase in ensemble n respectively. Substituting equation S7 into equation S6, we can rewrite equation S6 in terms of the KOP as follows:

$$\theta_n^i = \omega_n^i + \sum_{p=1}^{E} K_{np} \mathrm{Im}\left(e^{-i\theta_n^i(t)} z_p(t-\tau_{np})\right) \tag{S8}$$

Now we consider the case in which the number of oscillators in one ensemble is very large i.e. $N_n \to \infty$, and we define $\rho_n(\theta_n, \omega_n, t)$ as the probability density of oscillators in n with phase θ and frequency ω at time t. Since the number of oscillators on each ensemble remains unchanged, ρ_n satisfies the local continuity equation,

$$\frac{\partial \rho_n}{\partial t}+\frac{\partial}{\partial \theta_n}\left(\rho_n,\dot{\theta}_n\right)=\frac{\partial \rho_n}{\partial t}\frac{\partial}{\partial \theta_n}\left\{\rho_n\left[\omega_n+\sum_{p=1}^{E}K_{np}\mathrm{Im}\left(e^{-i\theta_n(t)}z_p\left(t-\tau_{np}\right)\right)\right]\right\}=0 \tag{S9}$$

Next we consider the Fourier series of ρ_n

$$\rho_n(\theta,\omega,t)=\frac{g_n(\omega)}{2\pi}\left[1+\sum_{k=1}^{\infty}c_{n,k}(\omega,t)e^{ik\theta}+c.c.\right], \tag{S10}$$

where c.c. stands for complex conjugate. Following the Ott and Antonsen ansatzt [42], we consider a class of $c(\omega,t)$ such that $c_{n,k}(\omega,t)=a_n(\omega,t)^k$, where $|a_n(\omega,t)|\le 1$. Then, inserting the series expansion $a_n(\omega,t)$ into equation S9 we obtain

$$\frac{\partial a_n}{\partial t}+i\omega_n a_n+\frac{1}{2}\sum_{p=1}^{E}K_{np}\left[z_p\left(t-\tau_{np}\right)a_n^2-z_p\left(t-\tau_{np}\right)\right]=0. \tag{S11}$$

Letting the distribution of frequencies $g_n(\omega)$ to be a Lorentzian distribution with center at Ω_n and spread of Δ_n, i.e.

$$g_n(\omega)=\frac{\Delta_n}{\pi\left[\left(\omega-\Omega_n\right)^2+\Delta_n^2\right]} \tag{S12}$$

we can calculate z_n in the continuum limit as

$$z_n=\int_{-\infty}^{\infty}\int_{0}^{2\pi}\rho_n(\theta,\omega,t)e^{i\theta}d\theta d\omega=\int_{-\infty}^{\infty}g_n(\omega)a_n(\omega,t)d\omega=a_n\left(\Omega_n-i\Delta_n,\mathrm{t}\right) \tag{S13}$$

Thus, by evaluating equation S11 at $\omega=\Omega_n-\Delta_n$, we can obtain the dynamics of z_n as

$$\dot{z}_n+\left(\Delta_n-i\Omega_n\right)z_n+\frac{1}{2}\sum_{p=1}^{E}K_{np}\left[z_p\left(t-\tau_{np}\right)z_n^2-z_p\left(t-\tau_{np}\right)\right]=0 \tag{S14}$$

Therefore the GWBM is defined by E complex delayed differential equations. Because of the first equality of equation S7, the GWBM with E equations can be converted to $2E$ real delayed differential equations with the forms

$$\dot{r}_n = -\Delta_n r_n + \frac{1-r_n^2}{2}\sum_{p=1}^{E} K_{np}\,\mathrm{Re}\left[z_p\left(t-\tau_{np}\right)e^{-i\psi_n}\right] \tag{S15a}$$

$$\dot{\psi}_n = \Omega_n + \frac{r_n^2+1}{2r_n}\sum_{p=1}^{E} K_{np}\,\mathrm{Im}\left[z_p\left(t-\tau_{np}\right)e^{-i\psi_n}\right] \tag{S15b}$$

where $\dot{r}_n$ and $\dot{\psi}_n$ describe the temporal evolution of the KOP ($z_n = r_n e^{i\psi_n}$) in terms of the level of synchrony and the mean phase in ensemble *n* respectively. The equations 1a and 1b in the main text are obtained by extracting the global coupling scaling factor, *G/E*, the local coupling, L_n, and the anatomical network of neural fibers, *A*, from the coupling matrix, K_{np} , in equations S15a and S15b.

3.5.3 Supplementary figures

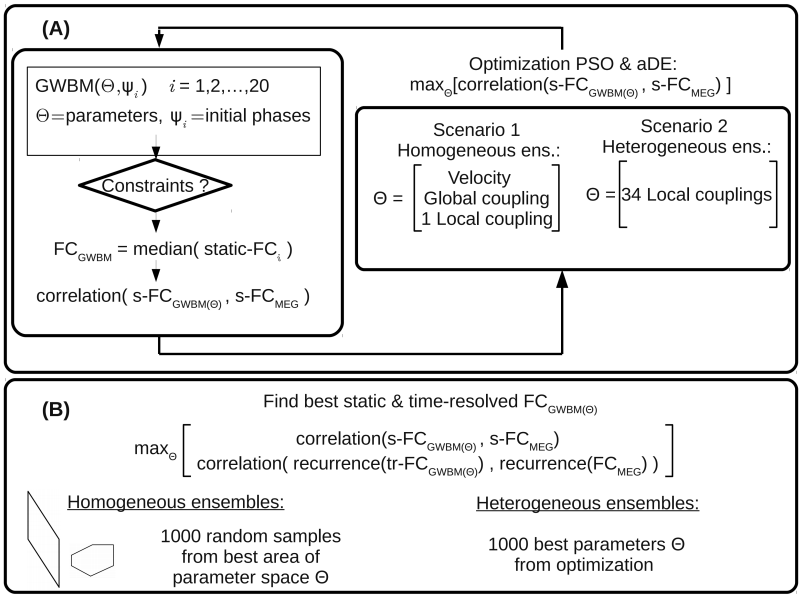

Supplementary Figure 1. *Schematic representation of the parameter identification process. (A) Optimization of parameters for the first (homogeneous ensembles) or the second scenario (heterogeneous ensembles). (B) Simulations to find the parameters that are able to predict static FC and time-resolved FC.*

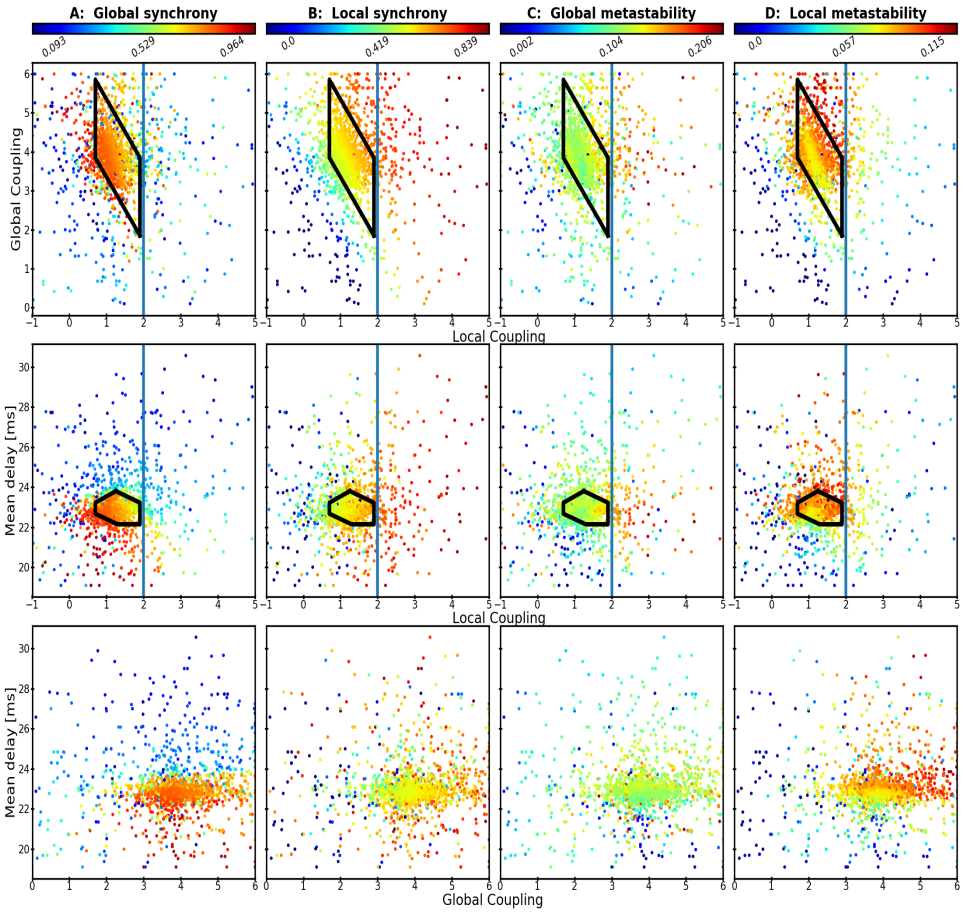

Supplementary Figure 2. *Dynamics of the model with homogeneous ensembles. Each dot corresponds to one combination of parameters (x-y axis) during the optimization. Each column corresponds to a different dynamical feature. (A) Global synchrony averaged over time. (B) Local synchrony averaged over ensembles first and then over time. (C) Global metastability (D) Local metastability averaged over ensembles. For each metric, each value corresponds to the median obtained across 20 simulations computed with different initial conditions. Vertical blue lines indicate the critical local couplings of the ensembles,* L^c*. The black areas indicate the region of the parameter space within which time-resolved fucntional connectivity was analyzed*

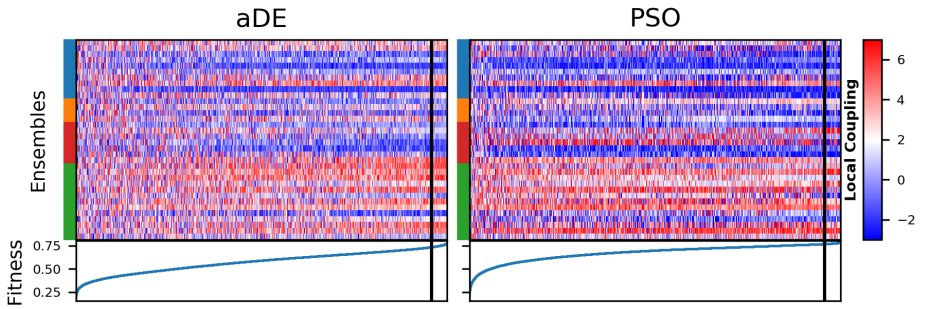

Sup. Figure 3. *Evolution of local couplings optimization sorted by fitness to MEG sFC. Each row inside the upper panel depicts the local couplings of one ensemble. The columns correspond to iterations of the respective optimizer (aDE and PSO). The brain lobe associated with each ensemble is color coded on the left (same as Figure 2). The fitness (Pearson correlation between MEG and simulated sFC) of each iteration is at the bottom of the panels. trFC was evaluated at the parameters to the right of the black vertical line.*

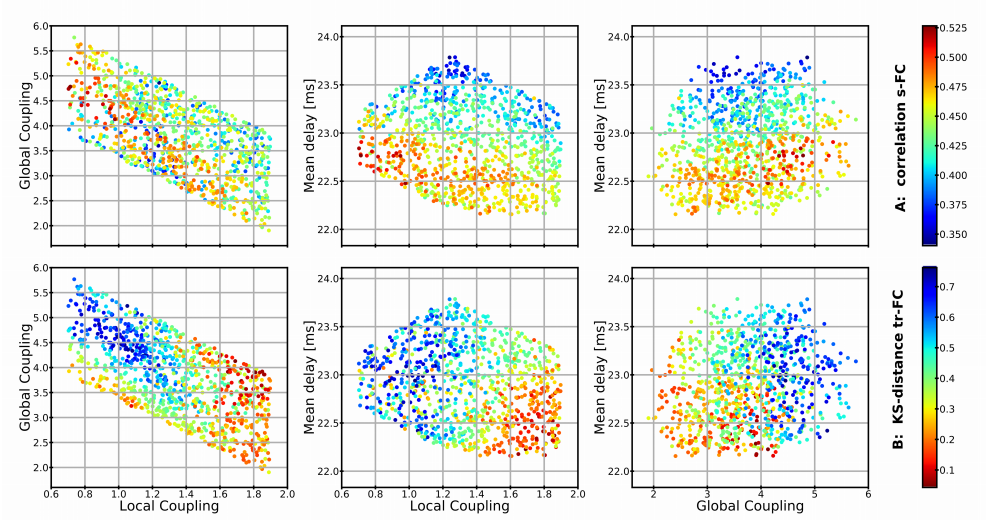

Sup. Figure 4. *FC comparison between 300-second simulations and MEG data. Each dot corresponds to one combination of parameters – global coupling, local coupling, and mean delay. The parameters are restricted to the area that gave the best sFC predictions during the optimization (black area in figure 2). (sFC, first row) correlation between the simulated and MEG sFC. (trFC, second row) KS-distance between the histograms (simulated vs. MEG data) built from the recurrence of sFC recurrence over a 15-second sliding window with 12-second overlap. Each dot is the median of 30 simulations with identical parameters and different initial conditions.*

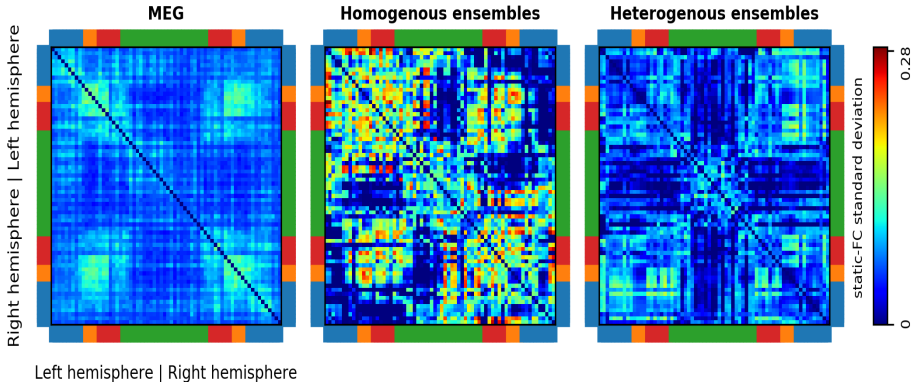

Sup. Figure 5. *Functional connectivity (FC) variability. (Left) Standard deviation of the FC over subjects (Middle, model with homogeneous ensembles) Standard deviation of the FC from simulations with identical parameters but different initial conditions. (Right, model with heterogeneous ensembles) Standard deviation of the FC from simulations with identical parameters but different initial conditions.*

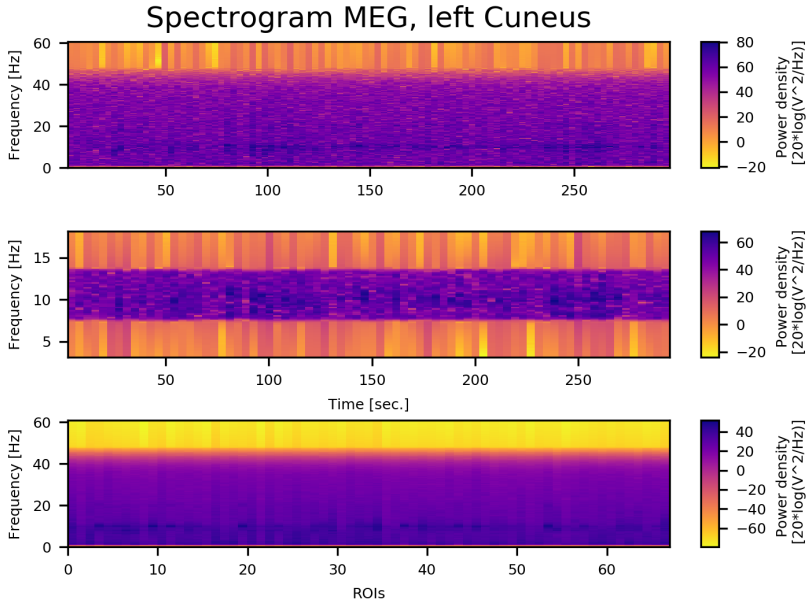

Sup.Figure 6. *Time-frequency spectrogram from MEG activity in the alpha band. (Above) Broadband activity with a low-pass filter at 48 Hz. (Middle) Band-pass filtered alpha-band activity. (Bottom) Welch periodogram of broadband activity in all ROIs .*

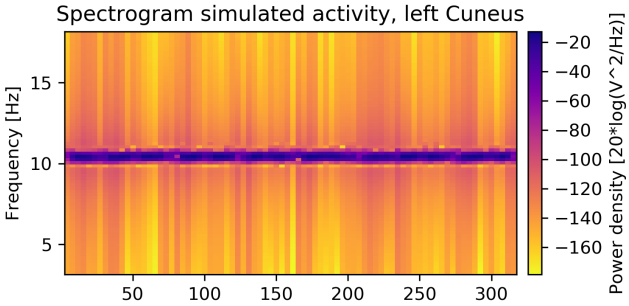

Sup. Figure 7. *Time-frequency spectrogram from simulated activity in the alpha band**.** The parameters are the s*ame parameters as Figure 2 and 5 for heterogeneous ensembles.

Institutional acknowledgments

Center for Information Technology of the University of Groningen for their support and for providing access to the Peregrine high performance computing cluster.

University of Oxford Advanced Research Computing (ARC) facility. http://dx.doi.org/10.5281/zenodo.22558

Joana Cabral from University of Minho and University of Oxford for insightful discussions and instrumental role in establishing this collaboration.

Ben Hunt from the University of Bristol (formerly in the group of Matt Brookes at the University of Nottingham) for the data collection as part of the UK MEG partnership

References

1. Braun U, Schäfer A, Walter H, Erk S, Romanczuk-Seiferth N, Haddad L, et al. Dynamic reconfiguration of frontal brain networks during executive cognition in humans. Proc Natl Acad Sci USA. 2015;112: 11678–11683. doi:10.1073/pnas.1422487112
2. Reinhart RMG, Nguyen JA. Working memory revived in older adults by synchronizing rhythmic brain circuits. Nat Neurosci. 2019;22: 820–827. doi:10.1038/s41593-019-0371-x
3. Portoles O, Borst JP, van Vugt MK. Characterizing synchrony patterns across cognitive task stages of associative recognition memory. Eur J Neurosci. 2018;48: 2759–2769. doi:10.1111/ejn.13817
4. Tewarie P, Hunt BAE, O'Neill GC, Byrne A, Aquino K, Bauer M, et al. Relationships Between Neuronal Oscillatory Amplitude and Dynamic Functional Connectivity. Cerebral Cortex. 2019;29: 2668–2681. doi:10.1093/cercor/bhy136
5. Byrne Á, Brookes MJ, Coombes S. A mean field model for movement induced changes in the beta rhythm. J Comput Neurosci. 2017;43: 143–158. doi:10.1007/s10827-017-0655-7
6. de Pasquale F, Della Penna S, Snyder AZ, Lewis C, Mantini D, Marzetti L, et al. Temporal dynamics of spontaneous MEG activity in brain networks. Proceedings of the National Academy of Sciences. 2010;107: 6040–6045. doi:10.1073/pnas.0913863107
7. Vidaurre D, Hunt LT, Quinn AJ, Hunt BAE, Brookes MJ, Nobre AC, et al. Spontaneous cortical activity transiently organises into frequency specific phase-coupling networks. Nat Commun. 2018;9: 2987. doi:10.1038/s41467-018-05316-z
8. Hipp JF, Hawellek DJ, Corbetta M, Siegel M, Engel AK. Large-scale cortical correlation structure of spontaneous oscillatory activity. Nat Neurosci. 2012;15: 884–890. doi:10.1038/nn.3101
9. Seedat ZA, Quinn AJ, Vidaurre D, Liuzzi L, Gascoyne LE, Hunt BAE, et al. The role of transient spectral 'bursts' in functional connectivity: A magnetoencephalography study. NeuroImage. 2020;209: 116537. doi:10.1016/j.neuroimage.2020.116537
10. Quinn AJ, van Ede F, Brookes MJ, Heideman SG, Nowak M, Seedat ZA, et al. Unpacking Transient Event Dynamics in Electrophysiological Power Spectra. Brain Topogr. 2019;32: 1020–1034. doi:10.1007/s10548-019-00745-5
11. Honey CJ, Sporns O, Cammoun L, Gigandet X, Thiran JP, Meuli R, et al. Predicting human resting-state functional connectivity from structural connectivity. PNAS. 2009;106: 2035–2040. doi:10.1073/pnas.0811168106
12. Breakspear M. Dynamic models of large-scale brain activity. Nat Neurosci. 2017;20: 340–352. doi:10.1038/nn.4497
13. Woolrich MW, Stephan KE. Biophysical network models and the human connectome. NeuroImage. 2013;80: 330–338. doi:10.1016/j.neuroimage.2013.03.059
14. Cabral J, Kringelbach ML, Deco G. Functional connectivity dynamically evolves on multiple time-scales over a static structural connectome: Models and mechanisms. NeuroImage. 2017;160: 84–96. doi:10.1016/j.neuroimage.2017.03.045
15. Cabral J, Luckhoo H, Woolrich M, Joensson M, Mohseni H, Baker A, et al. Exploring mechanisms of spontaneous functional connectivity in MEG: How delayed network interactions lead to structured amplitude envelopes of band-pass filtered oscillations. NeuroImage. 2014;90: 423–435. doi:10.1016/j.neuroimage.2013.11.047
16. Hadida J, Sotiropoulos SN, Abeysuriya RG, Woolrich MW, Jbabdi S. Bayesian Optimisation of Large-Scale Biophysical Networks. NeuroImage. 2018;174: 219–236. doi:10.1016/j.neuroimage.2018.02.063
17. Finger H, Bönstrup M, Cheng B, Messé A, Hilgetag C, Thomalla G, et al. Modeling of Large-Scale Functional Brain Networks Based on Structural Connectivity from DTI: Comparison with EEG Derived Phase Coupling Networks and Evaluation of Alternative Methods along the Modeling Path. PLoS Comput Biol. 2016;12: e1005025. doi:10.1371/journal.pcbi.1005025
18. Jirsa VK, Proix T, Perdikis D, Woodman MM, Wang H, Gonzalez-Martinez J, et al. The Virtual Epileptic Patient: Individualized whole-brain models of epilepsy spread. Neuroimage. 2017;145: 377–388. doi:10.1016/j.neuroimage.2016.04.049
19. Aerts H, Schirner M, Jeurissen B, Van Roost D, Achten E, Ritter P, et al. Modeling Brain Dynamics in Brain Tumor Patients Using the Virtual Brain. eNeuro. 2018;5. doi:10.1523/ENEURO.0083-18.2018

20. Schmidt H, Petkov G, Richardson MP, Terry JR. Dynamics on Networks: The Role of Local Dynamics and Global Networks on the Emergence of Hypersynchronous Neural Activity. Daunizeau J, editor. PLoS Comput Biol. 2014;10: e1003947. doi:10.1371/journal.pcbi.1003947

21. Roberts JA, Gollo LL, Abeysuriya RG, Roberts G, Mitchell PB, Woolrich MW, et al. Metastable brain waves. Nature Communications. 2019;10: 1056. doi:10.1038/s41467-019-08999-0

22. Kirst C, Timme M, Battaglia D. Dynamic information routing in complex networks. Nat Commun. 2016;7: 11061. doi:10.1038/ncomms11061

23. Qin Y, Kawano Y, Portoles O, Cao M. Partial Phase Cohesiveness in Networks of Kuramoto Oscillator Networks. 2019.

24. Coombes S, Byrne Á. Next generation neural mass models. arXiv:160706251 [q-bio]. 2016 [cited 9 Jul 2019]. Available: http://arxiv.org/abs/1607.06251

25. Pfurtscheller G, Lopes da Silva FH. Event-related EEG/MEG synchronization and desynchronization: basic principles. Clin Neurophysiol. 1999;110: 1842–1857.

26. Deco G, Cabral J, Woolrich MW, Stevner ABA, van Hartevelt TJ, Kringelbach ML. Single or multiple frequency generators in on-going brain activity: A mechanistic whole-brain model of empirical MEG data. NeuroImage. 2017;152: 538–550. doi:10.1016/j.neuroimage.2017.03.023

27. Deco G, Kringelbach ML, Jirsa VK, Ritter P. The dynamics of resting fluctuations in the brain: metastability and its dynamical cortical core. Sci Rep. 2017;7: 3095. doi:10.1038/s41598-017-03073-5

28. Roxin A, Compte A. Oscillations in the bistable regime of neuronal networks. Phys Rev E. 2016;94: 012410. doi:10.1103/PhysRevE.94.012410

29. Brunel N, Hakim V. Fast Global Oscillations in Networks of Integrate-and-Fire Neurons with Low Firing Rates. Neural Computation. 1999;11: 1621–1671. doi:10.1162/089976699300016179

30. Deco G, Jirsa V, McIntosh AR, Sporns O, Kötter R. Key role of coupling, delay, and noise in resting brain fluctuations. PNAS. 2009;106: 10302–10307. doi:10.1073/pnas.0901831106

31. Breakspear M, Heitmann S, Daffertshofer A. Generative Models of Cortical Oscillations: Neurobiological Implications of the Kuramoto Model. Front Hum Neurosci. 2010;4. doi:10.3389/fnhum.2010.00190

32. Cumin D, Unsworth CP. Generalising the Kuramoto model for the study of neuronal synchronisation in the brain. Physica D: Nonlinear Phenomena. 2007;226: 181–196. doi:10.1016/j.physd.2006.12.004

33. Kuramoto Y. Chemical Oscillations, Waves, and Turbulence. Courier Corporation; 2003.

34. Acebrón JA, Bonilla LL, Pérez Vicente CJ, Ritort F, Spigler R. The Kuramoto model: A simple paradigm for synchronization phenomena. Rev Mod Phys. 2005;77: 137–185. doi:10.1103/RevModPhys.77.137

35. Montbrió E, Pazó D, Roxin A. Macroscopic Description for Networks of Spiking Neurons. Phys Rev X. 2015;5: 021028. doi:10.1103/PhysRevX.5.021028

36. Luke TB, Barreto E, So P. Complete Classification of the Macroscopic Behavior of a Heterogeneous Network of Theta Neurons. Neural Computation. 2013;25: 3207–3234. doi:10.1162/NECO_a_00525

37. Woldman W, Schmidt H, Abela E, Chowdhury FA, Pawley AD, Jewell S, et al. Dynamic network properties of the interictal brain determine whether seizures appear focal or generalised. Sci Rep. 2020;10: 7043. doi:10.1038/s41598-020-63430-9

38. Yan B, Li P. The emergence of abnormal hypersynchronization in the anatomical structural network of human brain. NeuroImage. 2013;65: 34–51. doi:10.1016/j.neuroimage.2012.09.031

39. Daido H. Intrinsic fluctuations and a phase transition in a class of large populations of interacting oscillators. J Stat Phys. 1990;60: 753–800. doi:10.1007/BF01025993

40. Peter F, Pikovsky A. Transition to collective oscillations in finite Kuramoto ensembles. Phys Rev E. 2018;97: 032310. doi:10.1103/PhysRevE.97.032310

41. Ghosh A, Rho Y, McIntosh AR, Kötter R, Jirsa VK. Noise during Rest Enables the Exploration of the Brain's Dynamic Repertoire. PLOS Computational Biology. 2008;4: e1000196. doi:10.1371/journal.pcbi.1000196

42. Ott E, Antonsen TM. Low dimensional behavior of large systems of globally coupled oscillators. Chaos. 2008;18: 037113. doi:10.1063/1.2930766

43. Tsimring LS, Rulkov NF, Larsen ML, Gabbay M. Repulsive Synchronization in an Array of Phase Oscillators. Phys Rev Lett. 2005;95: 014101. doi:10.1103/PhysRevLett.95.014101

44. Wildie M, Shanahan M. Metastability and chimera states in modular delay and pulse-coupled oscillator networks. Chaos. 2012;22: 043131. doi:10.1063/1.4766592

45. Skardal PS, Restrepo JG. Hierarchical synchrony of phase oscillators in modular networks. Phys Rev E. 2012;85: 016208. doi:10.1103/PhysRevE.85.016208

46. Tognoli E, Kelso JAS. The Metastable Brain. Neuron. 2014;81: 35–48. doi:10.1016/j.neuron.2013.12.022

47. Nakagawa TT, Woolrich M, Luckhoo H, Joensson M, Mohseni H, Kringelbach ML, et al. How delays matter in an oscillatory whole-brain spiking-neuron network model for MEG alpha-rhythms at rest. NeuroImage. 2014;87: 383–394. doi:10.1016/j.neuroimage.2013.11.009

48. Caminiti R, Carducci F, Piervincenzi C, Battaglia-Mayer A, Confalone G, Visco-Comandini F, et al. Diameter, Length, Speed, and Conduction Delay of Callosal Axons in Macaque Monkeys and Humans: Comparing Data from Histology and Magnetic Resonance Imaging Diffusion Tractography. Journal of Neuroscience. 2013;33: 14501–14511. doi:10.1523/JNEUROSCI.0761-13.2013

49. Liewald D, Miller R, Logothetis N, Wagner H-J, Schüz A. Distribution of axon diameters in cortical white matter: an electron-microscopic study on three human brains and a macaque. Biol Cybern. 2014;108: 541–557. doi:10.1007/s00422-014-0626-2

50. Jiruska P, de Curtis M, Jefferys JGR, Schevon CA, Schiff SJ, Schindler K. Synchronization and desynchronization in epilepsy: controversies and hypotheses: Synchronization in epilepsy. The Journal of Physiology. 2013;591: 787–797. doi:10.1113/jphysiol.2012.239590

51. Deco G, Ponce-Alvarez A, Hagmann P, Romani GL, Mantini D, Corbetta M. How Local Excitation-Inhibition Ratio Impacts the Whole Brain Dynamics. Journal of Neuroscience. 2014;34: 7886–7898. doi:10.1523/JNEUROSCI.5068-13.2014

52. Abeysuriya RG, Hadida J, Sotiropoulos SN, Jbabdi S, Becker R, Hunt BAE, et al. A biophysical model of dynamic balancing of excitation and inhibition in fast oscillatory large-scale networks. Marinazzo D, editor. PLoS Comput Biol. 2018;14: e1006007. doi:10.1371/journal.pcbi.1006007

53. Kello CT, Brown GDA, Ferrer-i-Cancho R, Holden JG, Linkenkaer-Hansen K, Rhodes T, et al. Scaling laws in cognitive sciences. Trends in Cognitive Sciences. 2010;14: 223–232. doi:10.1016/j.tics.2010.02.005

54. Prinz AA, Bucher D, Marder E. Similar network activity from disparate circuit parameters. Nat Neurosci. 2004;7: 1345–1352. doi:10.1038/nn1352

55. Andrews-Hanna JR, Smallwood J, Spreng RN. The default network and self-generated thought: component processes, dynamic control, and clinical relevance. Annals of the New York Academy of Sciences. 2014;1316: 29–52. doi:10.1111/nyas.12360

56. Hansen N. The CMA Evolution Strategy: A Comparing Review. : 28.

57. Das S, Suganthan PN. Differential Evolution: A Survey of the State-of-the-Art. IEEE Trans Evol Computat. 2011;15: 4–31. doi:10.1109/TEVC.2010.2059031

58. Freyer F, Roberts JA, Becker R, Robinson PA, Ritter P, Breakspear M. Biophysical Mechanisms of Multistability in Resting-State Cortical Rhythms. Journal of Neuroscience. 2011;31: 6353–6361. doi:10.1523/JNEUROSCI.6693-10.2011

59. Skardal PS, Restrepo JG. Synchronization of Kuramoto oscillators in networks of networks. arXiv:12063822 [math, nlin]. 2012 [cited 9 Jul 2019]. Available: http://arxiv.org/abs/1206.3822

60. Demirtaş M, Burt JB, Helmer M, Ji JL, Adkinson BD, Glasser MF, et al. Hierarchical Heterogeneity across Human Cortex Shapes Large-Scale Neural Dynamics. Neuron. 2019;101: 1181-1194.e13. doi:10.1016/j.neuron.2019.01.017

61. Haegens S, Cousijn H, Wallis G, Harrison PJ, Nobre AC. Inter- and intra-individual variability in alpha peak frequency. Neuroimage. 2014;92: 46–55. doi:10.1016/j.neuroimage.2014.01.049

62. Sauseng P, Griesmayr B, Freunberger R, Klimesch W. Control mechanisms in working memory: a possible function of EEG theta oscillations. Neurosci Biobehav Rev. 2010;34: 1015–1022. doi:10.1016/j.neubiorev.2009.12.006

63. Klimesch W. α-band oscillations, attention, and controlled access to stored information. Trends Cogn Sci (Regul Ed). 2012;16: 606–617. doi:10.1016/j.tics.2012.10.007

64. Hillebrand A, Barnes GR, Bosboom JL, Berendse HW, Stam CJ. Frequency-dependent functional connectivity within resting-state networks: An atlas-based MEG beamformer solution. NeuroImage. 2012;59: 3909–3921. doi:10.1016/j.neuroimage.2011.11.005

65. Makeig S. Dynamic Brain Sources of Visual Evoked Responses. Science. 2002;295: 690–694. doi:10.1126/science.1066168

66. Martens EA, Barreto E, Strogatz SH, Ott E, So P, Antonsen TM. Exact results for the Kuramoto model with a bimodal frequency distribution. Phys Rev E. 2009;79: 026204. doi:10.1103/PhysRevE.79.026204

67. Petkoski S, Jirsa VK. Transmission time delays organize the brain network synchronization. Phil Trans R Soc A. 2019;377: 20180132. doi:10.1098/rsta.2018.0132

68. Hillebrand A, Tewarie P, van Dellen E, Yu M, Carbo EWS, Douw L, et al. Direction of information flow in large-scale resting-state networks is frequency-dependent. Proc Natl Acad Sci USA. 2016;113: 3867–3872. doi:10.1073/pnas.1515657113

69. Basti A, Pizzella V, Chella F, Romani GL, Nolte G, Marzetti L. Disclosing large-scale directed functional connections in MEG with the multivariate phase slope index. NeuroImage. 2018;175: 161–175. doi:10.1016/j.neuroimage.2018.03.004

70. O'Neill GC, Barratt EL, Hunt BAE, Tewarie PK, Brookes MJ. Measuring electrophysiological connectivity by power envelope correlation: a technical review on MEG methods. Phys Med Biol. 2015;60: R271–R295. doi:10.1088/0031-9155/60/21/R271

71. Mashour GA, Hudetz AG. Neural Correlates of Unconsciousness in Large-Scale Brain Networks. Trends in Neurosciences. 2018;41: 150–160. doi:10.1016/j.tins.2018.01.003

72. Marini F, Walczak B. Particle swarm optimization (PSO). A tutorial. Chemometrics and Intelligent Laboratory Systems. 2015;149: 153–165. doi:10.1016/j.chemolab.2015.08.020

73. Das S, Mullick SS, Suganthan PN. Recent advances in differential evolution – An updated survey. Swarm and Evolutionary Computation. 2016;27: 1–30. doi:10.1016/j.swevo.2016.01.004

74. Moles CG. Parameter Estimation in Biochemical Pathways: A Comparison of Global Optimization Methods. Genome Research. 2003;13: 2467–2474. doi:10.1101/gr.1262503

75. Vesterstrom J, Thomsen R. A comparative study of differential evolution, particle swarm optimization, and evolutionary algorithms on numerical benchmark problems. : 8.

76. Francesco Biscani, Dario Izzo, Marcus Märtens. esa/pagmo2: pagmo 2.7. Zenodo; 2018. doi:10.5281/zenodo.1217831

77. Hunt BAE, Tewarie PK, Mougin OE, Geades N, Jones DK, Singh KD, et al. Relationships between cortical myeloarchitecture and electrophysiological networks. PNAS. 2016;113: 13510–13515. doi:10.1073/pnas.1608587113

78. Hillebrand A, Barnes GR. Beamformer analysis of MEG data. Int Rev Neurobiol. 2005;68: 149–171. doi:10.1016/S0074-7742(05)68006-3

79. Desikan RS, Ségonne F, Fischl B, Quinn BT, Dickerson BC, Blacker D, et al. An automated labeling system for subdividing the human cerebral cortex on MRI scans into gyral based regions of interest. Neuroimage. 2006;31: 968–980. doi:10.1016/j.neuroimage.2006.01.021

80. Colclough GL, Brookes MJ, Smith SM, Woolrich MW. A symmetric multivariate leakage correction for MEG connectomes. Neuroimage. 2015;117: 439–448. doi:10.1016/j.neuroimage.2015.03.071

81. Behrens TEJ, Berg HJ, Jbabdi S, Rushworth MFS, Woolrich MW. Probabilistic diffusion tractography with multiple fibre orientations: What can we gain? Neuroimage. 2007;34: 144–155. doi:10.1016/j.neuroimage.2006.09.018

82. Jbabdi S, Sotiropoulos SN, Haber SN, Essen DCV, Behrens TE. Measuring macroscopic brain connections in vivo. Nat Neurosci. 2015;18: 1546–1555. doi:10.1038/nn.4134

83. Sotiropoulos SN, Jbabdi S, Xu J, Andersson JL, Moeller S, Auerbach EJ, et al. Advances in diffusion MRI acquisition and processing in the Human Connectome Project. Neuroimage. 2013;80: 125–143. doi:10.1016/j.neuroimage.2013.05.057

84. Van Essen DC, Ugurbil K, Auerbach E, Barch D, Behrens TEJ, Bucholz R, et al. The Human Connectome Project: a data acquisition perspective. Neuroimage. 2012;62: 2222–2231. doi:10.1016/j.neuroimage.2012.02.018

85. Hernández M, Guerrero GD, Cecilia JM, García JM, Inuggi A, Jbabdi S, et al. Accelerating Fibre Orientation Estimation from Diffusion Weighted Magnetic Resonance Imaging Using GPUs. PLOS ONE. 2013;8: e61892. doi:10.1371/journal.pone.0061892

86. Jbabdi S, Sotiropoulos SN, Savio AM, Graña M, Behrens TEJ. Model-based analysis of multishell diffusion MR data for tractography: how to get over fitting problems. Magn Reson Med. 2012;68: 1846–1855. doi:10.1002/mrm.24204

87. Glasser MF, Sotiropoulos SN, Wilson JA, Coalson TS, Fischl B, Andersson JL, et al. The minimal preprocessing pipelines for the Human Connectome Project. Neuroimage. 2013;80: 105–124. doi:10.1016/j.neuroimage.2013.04.127

88. Donahue CJ, Sotiropoulos SN, Jbabdi S, Hernandez-Fernandez M, Behrens TE, Dyrby TB, et al. Using Diffusion Tractography to Predict Cortical Connection Strength and Distance: A Quantitative Comparison with Tracers in the Monkey. J Neurosci. 2016;36: 6758–6770. doi:10.1523/JNEUROSCI.0493-16.2016

89. Jirsa VK, McIntosh AR, editors. Handbook of Brain Connectivity. Berlin Heidelberg: Springer-Verlag; 2007. Available: https://www.springer.com/gp/book/9783540714620

4 Thalamic bursts modulate cortical synchrony locally to switch between states of global functional connectivity in a cognitive task

To do any task, the brain goes through a sequence of cognitive stages, ranging from perceptual processing to creating a motor response. These stages are thought to be triggered by sub-cortical events that modulate cortex-wide neural coordination. However, our understanding of these dynamics remains limited due to technical and methodological challenges. Here, we overcame these challenges by applying machine-learning to identify the onset of cognitive stages on a trial-by-trial basis in MEG data from an associative recognition task. Our analysis revealed that each cognitive stage starts with brief modulations of local synchrony followed by a new cortex-wide network of directed functional connectivity that persists throughout the stage. To understand how the brain switches between these cognitive stages of cortical coordination, we used a generative whole-brain model. Sub-cortical inputs at the onset of cognitive stages imitated thalamocortical bursts targeted at excitatory or inhibitory cortical synapses that modulate local connectivity strength. In addition to the sub-cortical inputs, the anatomical topology of the brain contributed to determining new states of coordination. The simulated sequence of coordination states was consistent with observations in the MEG data. This whole-brain model solved, for the first time, the challenges that prevent the simulation of coordination dynamics throughout a task. More generally, these results shed light on the network-level mechanisms needed for reaching the neural coordination states that form the basis of our cognition. Finally, they pave the way to understanding other phenomena such as the interplay between localized brain stimulation, cortex-wide activity modulations, and cognition.[3]

3 Submitted as Portoles, O., Van Vugt, M. Cao, Borst, J.P. "*How the Brain Switches between Cognitive Processes: modulations of local coordination lead to switches in cortico-cortical coordination*"

4.1 Introduction

Already in the 19th century, Donders hypothesized that information processing in the brain proceeds through a sequence of fundamental cognitive stages with different functions such as visual encoding, memory retrieval, and decision making (1). Initially, cognitive stages were investigated with behavioral metrics like reaction time (e.g., (2)). Over the past decade, neuroimaging analyses have begun to uncover the neural correlates of these cognitive stages (e.g., (3)).

The dominant view is that cognitive stages require specific patterns of neural coordination across the cortex (3–5). The transition between cognitive stages is thought to be driven by the basal-ganglia-thalamus (BGT) system which sets new states of cortical coordination (6–9). The striatum monitors the current state of the cortex, and based on a comparison to predefined states, selects and triggers the next cognitive stage. The role of the BGT system modulating cortical coordination is supported by animal studies, intracranial recordings, and neural models (10–15). However, the network-level mechanisms required to reach a new state of cortical coordination from subcortical inputs are poorly understood.

To give a detailed account of these mechanisms, one first need to characterize the different states of neural coordination within the sequence of cognitive stages. We measured neural activity with cortically projected magnetoencephalographic (MEG) recordings as these have a sufficiently fine temporal resolution to measure cognitive stages, as well as adequate spatial resolution. However, cognitive stages have high temporal variability – that is, stages typically have a different duration on each trial of an experimental task – which makes it difficult to measure neural coordination. To overcome this problem,we used a machine learning method that identifies the onsets of cognitive stages on a trial-by-trial basis (16). Afterwards, the stage onsets were used to time-lock the measures of neural coordination within regions (local synchrony) and between regions (functional connectivity, FC), as there are concurrent changes at both spatial scales (17, 18).

The machine learning method to identify cognitive stages combines multivariate pattern analysis with a Hidden semi-Markov Model (HSMM-MVPA). The HSMM-MVPA method searches in each trial for a sequence of short-lived modulations of MEG amplitude (hereafter called *bumps,* following the original paper (16)) that have a consistent topology across trials. These bumps signify the onset of cognitive stages, and are thought to be triggered by the BGT system. Previously this method has been used successfully to, for example, identify the cognitive stages that are affected by task manipulations such as difficulty, stage insertion, and evidence accumulation for decisions (4, 5, 16, 19, 20).

To understand how events from the BGT system can cause switches between states of neural coordination – and thus between cognitive stages – we build upon generative whole-brain biophysical models of large-scale activity (GWBM) that have been used to explain

the dynamics of neural coordination at rest (21). GWBMs reduce the whole-brain network of neurons and synapses to a smaller network that still incorporates the most relevant principles of neural dynamics. The nodes of such a network describe the macroscopic activity within a region, while the links reflect the neural fibers that connect these regions (i.e. structural connectivity).

GWBMs of resting state indicate that time-resolved patterns of neural coordination are related to the anatomical structure of the brain and that these patterns evolve without requiring any input (a phenomenon referred to as *metastable coordination*; (18, 21, 22). Such coordination dynamics are thought to provide an optimal mechanism for simultaneously integrating and segregating information that allows the system to adapt quickly or alternatively, to persist in a given state (23). While this is sufficient to explain resting-state data, cognitive tasks require specific, controlled sequences of coordination states.

Here, we explored a GWBM in which inputs from the BGT system modulated local connectivity strength briefly at the onset of cognitive stages, as suggested by cognitive theories and electrophysiology measurements (6–15). In other complex networks with similar dynamics as the brain, such local perturbations can, in turn, produce controlled switches between global states (24). Similarly, even though the inputs from the BGT system only triggered direct changes in local connectivity strength, we observed transient modulations of local synchrony and switches to the targeted states of directed functional connectivity that lasted until the next input. When there were no further inputs from the BGT system, neural coordination returned to resting-state patterns after tens of seconds. These results matched the observed neural coordination throughout the cognitive stages in the empirical data. Finally, we used the GWBM to determine the importance of each brain region in facilitating the switches between states of coordination.

4.2 Results

4.2.1 Five cognitive stages in an associative memory task.

We re-analyzed MEG data from an associative memory recognition task with 18 participants (3). We chose this task because associative recognition memory requires a rich variety of cognitive stages that have been widely studied (3, 5, 16, 25, 26). The task consisted of a self-directed learning phase during which participants memorized 32 word pairs and a test phase. In the test phase – which we analyzed here – participants were again presented with word pairs. These could be *target* pairs from the learning phase or *re-paired foil* pairs, which consisted of the same words paired differently (e.g., if the participants learned apple-tree and month-house, a foil pair could be apple-house). Participants were asked to indicate as quickly and accurately as possible with a key press if it was a learned

pair or a re-paired foil. Only correct responses were included in our analysis. We were interested in the evolution of neural coordination along with the cognitive stages involved in performing the task, and in particular in how the brain switches between these consecutive states of functional neural coordination.

As the goal is to develop a cortical model, the MEG signals were projected onto 5,124 cortical sources using the structural MRI of each participant with minimum-norm estimation (3, 27). The resulting cortical activity was parcellated and averaged into time-series for 68 cortical regions following the Desikan-Killiany atlas (28, 29). Next, HSMM-MVPA was used to estimate the timing of bumps that indicate the onset of cognitive stages in each trial. All trials were assumed to go through the same sequence of stages as in previous studies (3, 4, 16). Thus, bumps were assumed to have the same spatial topology across trials, but trial-to-trial variable temporal location. Nevertheless, the HSMM-MVPA can cope relatively well with extra bumps in some trials (16). The intervals between stimulus-onset-to-bump, bump-to-bump, and bump-to-response constitute the cognitive stages. A leave-one-subject-out cross validation method showed that the MEG data were best explained by a HSMM-MVPA model with four bumps, which corresponds to five cognitive stages (Figure 1A).

Following previous work on associative recognition (3, 5, 16), we interpreted the five cognitive stages as follows: pre-encoding, encoding of visual information, memory retrieval, decision making, and motor response. We did not analyze the pre-encoding stage as it is mostly driven by the task stimulus and not by events from the BGT system that are associated with transitioning between cognitive stages. The retrieval and motor stages were longer and had larger across-trial variability than the encoding and decision stages (Figure 1A and 1E).

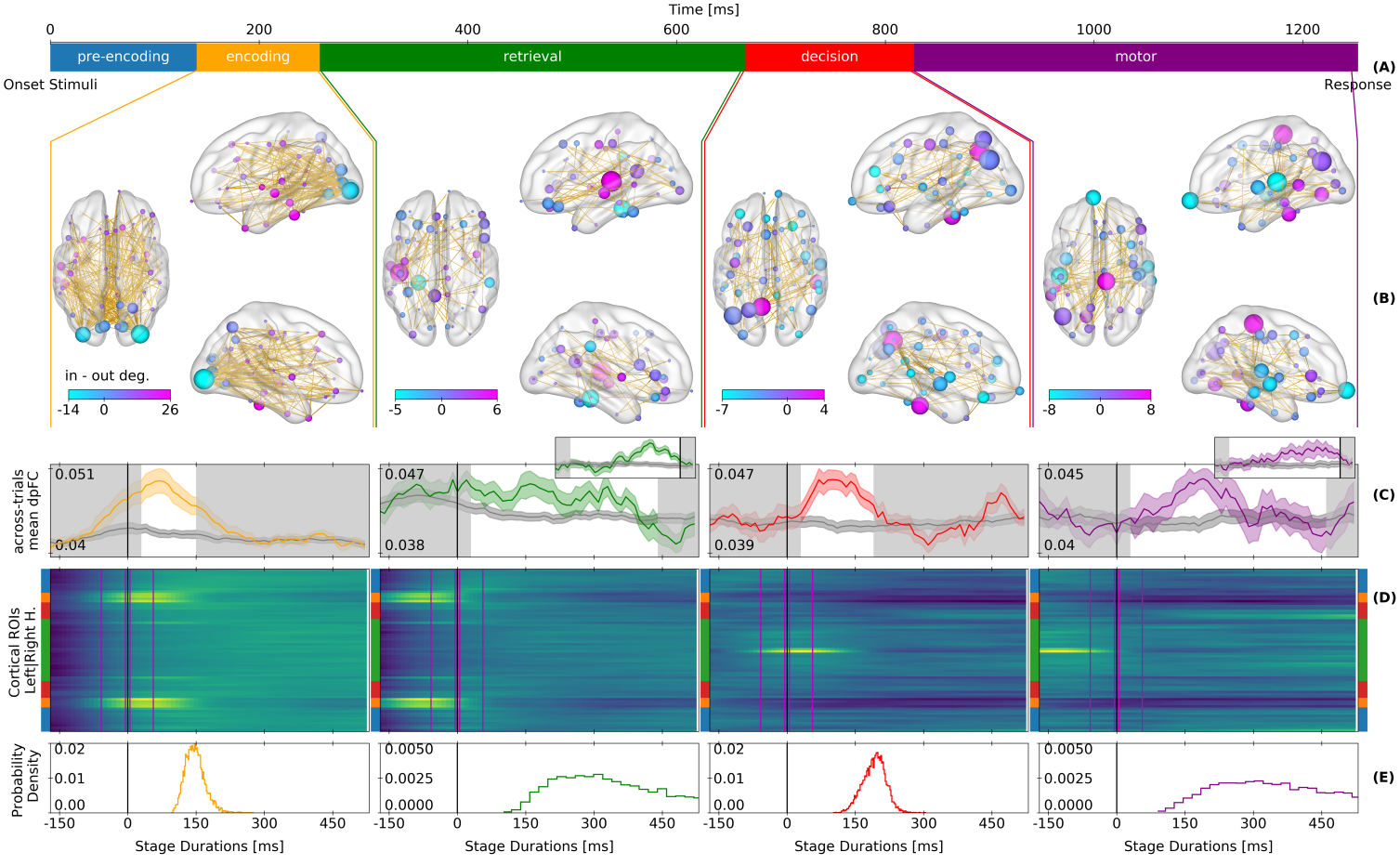
Time [ms]
0
200
400
600
800
1000
1200
pre-encoding
encoding
retrieval
decision
motor
(A)
Onset Stimuli
Response
(B)
in - out deg.
-14 0 26
-5 0 6
-7 0 4
-8 0 8
across-trials mean dpFC
0.051
0.04
0.047
0.038
0.047
0.039
0.045
0.04
(C)
Cortical ROIs Left|Right H.
(D)
Probability Density
0.02
0.01
0.00
0.0050
0.0025
0.0000
(E)
-150 0 150 300 450
Stage Durations [ms]

Figure 1. *Theta-band MEG local synchrony and directed functional connectivity by cognitive stages. (A) Cognitive stages derived with the HSMM-MVPA with their median durations. (B) Significant directed functional connectivity throughout the stage (within-stage dpFC). Links go from phase-ahead to phase-behind regions. The nodes represent the nodal degree (size) and the difference between phase-ahead and phase-behind links (color). (C)* Directed functional connectivity time-locked at the onset of the stages (*across-trials dpFC*). *Color (dark gray) line: average across links with (without) significant across-trial dpFC at the current stage; Shade around lines: standard error of the mean across subjects. Black vertical lines are the onset of the stages. The white background spans the median stage duration. Retrieval and response insets: Directed functional connectivity time-locked to the onset of the* decision stage and to the end-of-trial response, respectively *(D) Across-trials averaged local synchrony (z-scored envelope of amplitudes) time-locked at the onset of the stages. Y-axis represents cortical regions – blue: temporal, orange: occipital, red: parietal, and green: frontal. Magenta lines: time windows to measure the relative change in local coordination at the onset of the stages. (E) Histogram of stage durations derived with the HSMM-MVPA.*

4.2.2 Different local synchrony and directed functional connectivity states between stages.

Next, we measured neural coordination in the discovered stages. We focused on coordination of theta band oscillations (4-8 Hz), for several reasons: we previously found this frequency band to vary across task stages (4); theta oscillations have been related to cognitive processes such as attention, memory, control, and decision making (30–33); the phase of theta oscillations is known to modulate the activity in higher frequency bands (31, 34); local modulations of theta-band activity are hypothesized to mediate changes in long-range functional connectivity (35); and thalamic activity modulates cortical theta band activity (36).

Directed FC in the theta band was operationalized by means of the directed phase-lag index (37) (dpFC). A significant dpFC indicates that the phase in one region is consistently ahead or behind another region. The significance of dpFC was obtained using 200 surrogate data sets with random circular shifts of the original phases. We measured first *within-stage dpFC* to capture directed FC states that are constant from the start to the end of a cognitive stage. Figure 1B shows the links with significant within-stage dpFC, as well as the local difference between phase-ahead and phase-behind links (node color) and the total number of links regardless of their direction (node size). Next, we measured *across-trial dpFC* of the significant links in a stage to reveal the temporal evolution of directed FC during the

stage (Figure 1C). Across-trial dpFC was calculated sample-by-sample with the trials time-locked to the onset of each stage.

Across-trial dpFC revealed that functional states of directed FC switch at the transition between cognitive stages. These switches are visible because across-trial dpFC takes into account the trial-to-trial temporal variability of the cognitive stages as revealed by the HSMM-MVPA analysis. For example, for the memory retrieval stage, across-trial dpFC seems to fade halfway through. However, when across-trial dpFC is time-locked to the onset of the next stage – the decision stage – dpFC for memory retrieval materializes until shortly before the decision stage (see the insets in Figure 1). This illustrates why the HSMM-MVPA analysis is crucial: otherwise dpFC would appear to fade quickly after stimulus onset, while that is not the case when first isolating cognitive stages.

Local synchrony was operationalized as the envelope of the theta band analytic signals in each region, which indicates the degree of synchronous neural activity within a region. The envelopes were z-scored over time and then averaged across trials and participants. Across-trial averages were time-locked to the onset of cognitive stages which gave a time course of local synchrony for each stage (Figure 1D). This showed that local synchrony occurred only briefly at the start of each stage, with different regions depending on the functionality of the stage.

As expected, each stage had a different neural coordination pattern. In the visual encoding stage, occipital and left-temporal regions showed local synchrony and dpFC which might facilitate the transfer of visual information to the medial temporal lobe and the hippocampus to start a retrieval process (26). The encoding of information is controlled by a large fronto-posterior, fronto-lateral network (30, 31). During the memory retrieval stage, local synchrony at occipital and temporal regions is reduced. dpFC now happens mostly between left-medial-temporal and frontal regions, whose coordination is required for memory tasks (26, 38). At the onset of decision making the frontal regions begin to synchronize locally. The decision process is mediated by fronto-parietal dpFC (32), and dpFC between temporal and parietal regions dpFC to reinsert the memory retrieved into the left-parietal cortex (26). Finally, at the motor stage a large dpFC network appears between motor, temporal, left-parietal, and pre-frontal regions. This complex network has previously been associated with motor preparation, action reevaluation, decision, and cognitive control (33, 39), suggesting that the action is reevaluated during the motor response (40).

Together, these analyses unveiled that right at the onset of a cognitive stage there is a reorganization of neural coordination in the cortex. Whereas the change in local synchrony was only brief, dpFC lasted throughout the cognitive stage, indicating that short modulations of local synchrony can have persistent global effects. Next, we used a GWBM to investigate the mechanism underlying this.

4.2.3 Generative large-scale whole-brain model (GWBM)

In order to integrate cognitive stages and neural coordination into one framework along with neural anatomy and neural dynamics, we used a parsimonious GWBM that describes within- and between-region modulations of synchrony. Previously, we have used this model to demonstrate that modulations of local synchrony are related to time-resolved FC during resting state (18).

This GWBM is a low-dimensional reduction of a network-of-networks of Kuramoto oscillators (41). Kuramoto oscillators describe the dynamics of synchrony in biological systems including neural networks (22, 42, 43). Each sub-network represents a cortical region. All units in a region are assumed to be fully and instantly connected, while connections between regions are weighted and delayed by the density and length of the neural fibers in MRI-derived structural connectivity networks. The regions in the GWBM were defined with the same parcellation atlas as the MEG data that we seek to model.

First, we set default values for local connectivity strength (L in Eq. 2, identical for all regions), and global scaling (G in Eq. 2 and Eq. 3) of the structural connectivity such that the model simulated resting-state coordination dynamics in the theta-band (21, 44). Resting-state dynamics are characterized by fluctuations over time of local synchrony and time-resolved FC patterns (i.e. local and global metastability) (18, 21, 44). These dynamical properties of resting state neural coordination were identified with GWBMs simulated over a grid of L and G values. The identified L and G displayed the most similar dynamics to local and global metastability in the grid search.(see Supplementary Information and Supplementary Figure S1A).

Next, we simulated the switching between cognitive states by adding short inputs (30 milliseconds) from the BGT system at the onset of cognitive stages. The rationale for using this mechanism derives from theories of cognition and data derived from electrophysiology. Cognitive theories state that the BGT system modulate cortical coordination at the onset of cognitive stages via thalamocortical signals (6, 25). Electrophysiology has shown that thalamocortical neurons can indeed drive cortical activity (11, 14) and establish FC (45, 46). These thalamocortical neurons tend to produce short burst of activity (47), which target pools of either excitatory or inhibitory cortical neurons specifically (13, 48). Therefore, our model simulated thalamocortical inputs as short pulses of increased or decreased local connectivity strength (L in Eq. 2) that represent transient modulations in excitatory or inhibitory synaptic activity (43).

To simulate the sequence of neural coordination states found in the MEG data, we estimated the required activity pulses simultaneously in all regions, stage-by-stage. The optimization scheme maximized concurrently the fitness of local synchrony and within-stage dpFC, while minimizing the total magnitude of the pulses. The optimization was

accomplished with the generalized island model for distributed evolutionary optimization which in relatively short time explores and exploits different areas of the parameter space simultaneously (49).

4.2.4 Changes in local connectivity cause switches between global states of cognitive coordination

To assess how well the model simulated local synchrony, we measured the relative change in theta envelope before and after stage onset (magenta lines in Figure 1D). All model results were computed from 1000 models randomly selected from the top one percentile of models after the optimization. Relative changes in simulated and MEG envelopes were correlated significantly across different cortical regions (Spearman's ρ – encoding: 0.552 ± 0.00158 SEM; retrieval: 0.702 ± 0.000434 SEM; decision: 0.743 ± 0.000683 SEM; motor 0.477 ± 0.00151 SEM; all p-values < 0.05).

Figure 2A compares the within-stage dpFC fitness of the *worst* model in the top one percentile to a distribution of the same fitness metric obtained with 20,000 random within-stage dpFCs, indicating that the model performs much better than chance. Figure 2B shows the fitness of within-stage dpFC at individual links. The fitness was quantified as the proportion of links with the same phase-lag direction as in the MEG data (encoding: 0.697 ± 0.00014 SEM; retrieval: 0.837 ± 0.0016 SEM; decision: 0.749 ± 0.00092 SEM; motor: 0.758 ± 0.001 SEM). Figure 2C compares the across-trial dpFC of the model to the MEG data over time. Each state of dpFC begins after the pulse that modulates local connectivity strength at the onset of the stage, and vanishes with the next onset (Figure 2C). The last state of dpFC – the motor response – vanishes slowly (~10 seconds), and the GWBM returns to resting-state coordination dynamics (Supplementary Figure S2).

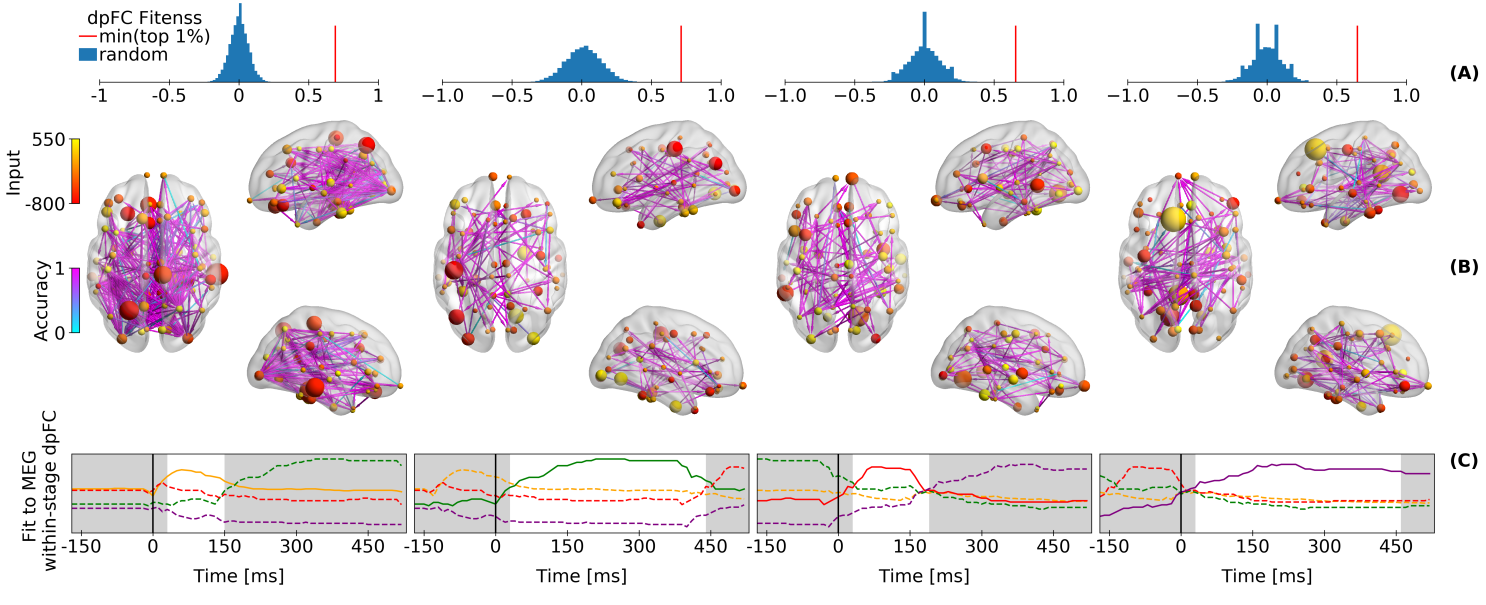
dpFC Fitenss
min(top 1%)
random
(A)
Input
550
-800
Accuracy
1
0
(B)
Fit to MEG
within-stage dpFC
(C)
Time [ms]
Time [ms]
Time [ms]
Time [ms]

Figure 2. *Simulated directed functional connectivity.(A) Blue histograms show the fitness between 20,000 randomly generated within-stage dpFCs* and the MEG *within-stage dpFC.* The red line indicates the *within-stage dpFCs* fitness of the model with the lowest fitness index within the top 1 percentile of the optimized models. *(B) Fitness of simulated-to-MEG within-stage dpFC is shown in cyan-purple grading over MEG links with significant within-stage dpFC (same as Figure 1B). The nodes indicate the relevance of a region for reaching a state of within-stage dpFC (size), and the pulse of local connectivity strength at the onset of the stage due to sub-cortical inputs (colors). These results show the averages of 1000 random picks from top ~1% of the optimizations. (C) Temporal evolution of simulated-to-MEG fitness of within-stage dpFC for the current stages (solid lines) compared to other stages (dashed). The white background spans the median stage duration. The color of the lines represent the different stages and follows Figure 1C.*

Taken together, the GWBM showed that a short pulse of local connectivity strength at the onset of a cognitive stage can first cause a modulation of local synchrony and then a new state of dpFC that lasts until the onset of the next stage (Figure 2C). If there is no subsequent cognitive stage, the GWBM returns to the coordination dynamics that are characteristic of the resting state.

4.2.5 Relevance of regions to switch between functional states of coordination

Not all regions in the GWBM are equally important for switching between states of dpFC. The relevance of a region increases with the size of the pulses and the strength of structural connectivity with other regions. The size of the nodes in Figure 2B indicates the relevance of a region for switching between states of dpFC. The absolute size of the pulses from the BGT predicts 22.52 % (± 0.096 SEM) of the variance in the relevance of the nodes, while the interaction between the absolute size of these BGT pulses and the log-scaled strength of structural connectivity predicts 25.98 % (± 0.12 SEM) of the same variance.

This analysis shows that there are regions like the left superior frontal region in the last stage that do not show dpFC, but that are still highly relevant for entering a state of high dpFC between other regions. This supports the mechanistic role of the superior frontal regions in cognitive control (30, 32); and it highlights the complexity of interactions required for implementing changes in FC patterns.

4.3 Discussion

In this paper, we first analyzed the evolution of macroscopic neural coordination across the cortex during an associative recognition memory task. Our analysis of MEG data showed that at the onset of fundamental cognitive stages there are transient modulations of local synchrony, which are directly followed by a new state of dpFC that persists until the next cognitive stage. Next, we used a generative model of whole brain activity (GWBM) with inputs from the basal-ganglia-thalamus system to explain these findings. The GWBM showed that short pulses that strengthen or weaken local connectivity strength at the onset of cognitive stages were sufficient to cause the switch between states of neural coordination consistent with empirical data. In addition, the GWBM indicated which individual regions were most relevant for causing these switches.

4.3.1 GWBM and the Basal Ganglia-Thalamus Circuit

The GWBM that we developed in this paper has shown that inputs from the basal-ganglia-thalamus system at the onset of cognitive stages are sufficient to cause switches between cognitive stages. This role of the BGT system had been hypothesized by cognitive theories (6, 25). Direct evidence for thalamic modulations of cortical activity is limited to some cortical regions due to methodological constraints, such as the fact that it is challenging to record simultaneously from many sub-cortical and cortical areas with high temporal resolution (11, 13, 14, 45). Nevertheless, a recent meta-analysis has shown that the thalamus plays a critical role as a central hub that connects neighboring and distant regions to allow for cognitive functions (10), which is in line with the hypothesis that local thalamocortical inputs can mediate FC (15). In addition, there is evidence for neural fibers connecting the thalamus with most cortical regions (50). Our model provides additional support for both hypotheses: the BGT systems can trigger the switch between fundamental stages of cognition (6, 25) and thalamic input modulates coordination of cortical activity according to cognitive demands (15).

Given our limited understanding of how the thalamus modulates cortical activity, we opted for a very simple representation of thalamocortical input. These inputs were short (45–47), targeted excitatory or inhibitory local connections (13, 48), and came at the onset of cognitive stages (6, 25). Such inputs drove the GWBM throughout the sequence of empirical local synchrony and dpFC states. Afterwards, the GWBM returned to resting state dynamics. In other words, a short modulation of local excitation/inhibition modified the local synchrony and the phase of the local mean-field oscillation. This change in local mean-field phase set a new phase-lag relationship with other regions that vanished over time due to structural cortical interactions. This response to local perturbations suggests that cortical dynamics are metastable as many states of coordination can be reached, and the brain does not remain into a particular state in the absence of perturbations. Metastable

dynamics are thought to allow for integrating and segregating information simultaneously, as well as for the flexibility of cognitive functions and behaviors (23).

Importantly, dpFC was not driven by thalamocortical inputs exclusively. Instead, the macroscopic connectivity structure of the brain also played an important role. The relevance of the structural connectivity was highlighted by the presence of regions with very low dpFC that turn out to be very important for coordinating other pairs of regions. One example of such regions is the left superior frontal region during the motor response stage, a region that has been related to cognitive control, attention, and decision making (30, 32, 33). The role of structural connectivity for generating specific coordination patterns was first brought to light by GWBMs of resting-state dynamics (21, 22). In a previous study we have shown analytically that the strength of structural connectivity plays an important role in selectively coordinating regions by means of modulations of local connectivity strength (51). Additionally, structural symmetries and time-delays might have influenced dpFC in our simulations (22, 52, 53).

There are other biological aspects that might be relevant for coordination of cortical activity that were not included here, including the delay over thalamocortical neurons (54), the dynamics of the synapses targeted by thalamocortical inputs (13), tonic activity in the thalamus (47), noise, or the state of cortical oscillations at the time of a thalamic input. Moreover, our measurement of directed FC has neglected zero-phase-lag coordination which can emerge from thalamocortical and cortico-cortical loops (54). However, while including these additional aspects might improve the fit of the model, the current model could already account for the data surprisingly well. Additionally, we have assumed that perturbations of cortical dynamics at the onset of cognitive stages come exclusively from the thalamus. However, there might be other regions such as the hypothalamus that modulate cortical activity in the same or another way that is not included in our model.

4.3.2 Neural coordination across the cortex along a sequence of cognitive stages

Our stage-by-stage analyses of neural coordination corroborates the hypothesis that the local modulations of phase synchrony in the theta-band mark a change in long-range functional connectivity and enable a new cognitive function (35). Moreover, our results confirm the hypothesis that a new state of neural coordination is established at the onset of cognitive stages (6, 8). Our previous research has shown that alpha band FC also varies across cognitive stages (4), but cortical alpha has been found to lead thalamic activity rather than being caused by it (55), as is the case with theta (14).

To uncover neural coordination stage-by-stage it was crucial to account for the temporal variability of cognitive stages across trials using the HsMM-MVPA analysis. Only after

correcting for this variability, our analyses showed that dpFC lasts throughout a cognitive stage and differs across stages. The corresponding states of dpFC had different length, strength, and topology. This diversity of properties might have biased some traditional metrics of neural coordination. For example, if one were interested in the FC at the interval between 250 and 600 milliseconds after stimulus onset – roughly the period of memory retrieval, this interval would contain elements of the encoding or decision stages. The first reason for this is the trial-by-trial variability in stage durations: in one trial encoding might last till 400 ms, while in another trial memory retrieval might already have finished by 400 ms. Secondly, the retrieval stage has fewer and weaker connections than the encoding and decision stages in our study, which mean that these connections might have been missed altogether. These effects are worse the further one moves away from fixed time points (trial onset/response), which is one of the reasons that M/EEG studies have had severely limited trial lengths traditionally.

Furthermore, our stage-by-stage analysis might contribute to disentangling competing theories. For example, our results suggest that the decision is made and evaluated in the last two stages. We interpreted the penultimate stage as a decision process in which memories are transferred to parietal areas by coordinating left-temporal regions with parietal regions, mediated by local frontal and fronto-parietal coordination (16, 26, 30, 32). The last stage has been traditionally related with a pure motor response. However, our results indicate that the motor stage has elements associated with motor preparation, action reevaluation, decision, and cognitive control (31, 33, 39). This functional network suggests that during the motor stage the decision is reevaluated, and it supports the line of thought in which responding is a process that is not independent from decision making (e.g., (40, 56).

4.3.3 Conclusion

To the best of our knowledge we have developed the first generative large-scale brain model that simulates the dynamics of the states of neural coordination along the fundamental cognitive stages in a task. In this model we have integrated structural connectivity, macroscopic neural dynamics, sub-cortical inputs, and the theoretical basis of associative recognition memory. The model has multiple simplifying assumptions which made it feasible to simulate and optimize the model while taking into accountthe macroscopic properties of neural anatomy and dynamics.

4.4 Methods

4.4.1 Experimental paradigm

We re-analyzed MEG data from an associative memory task (3). We combined the trials with correct responses from all experimental conditions, as we were interested in the

transition between fundamental cognitive stages and not in the differences between conditions (which did all proceed through the same stages; (16)). All 18 participants were right handed (6 males and 12 females with mean age of 23.6 years).

First, participants studied 32 pairs of words until they knew them well (3). This was followed by a test session in which MEG was recorded. In the test session participants were presented with pairs of words which were either the same as in the study season (*targets*) or paired differently (*re-paired foils*). The pairs of words remained on the screen until the participant responded, and were followed by 1-sec feedback and a brief inter-trial interval. A full description of the task and the recording procedure can be found in (3).

4.4.2 MEG data preprocessing

MEG data was preprocessed and source reconstructed following the analysis pipeline of the original manuscript (3). After artifact rejection there were 6,708 trials left. The MEG data of each participant was combined with their own structural MRI to obtain the cortical sources of MEG data. MEG sources consisted of 5,024 dipoles estimated with cortically constrained minimum norm estimates (3, 27). Source estimates were then morphed onto the standard MNI brain and parcellated into 68 cortical regions with the Desikan-Killiany atlas (29). Each parcel contained the average activity of all dipoles within the region with a 100 Hz sampling rate.

4.4.3 Identification of cognitive stages

To find the onset of cognitive stages the data were bandpass filtered (1-30 Hz, which are default values in Field Trip (60)) and epoched from trial onset to response. Single trials were baseline corrected (-0.4 to 0 seconds), and transformed to one covariance matrix per subject. The average covariance matrix across subjects was used to reduce the dimensionality of the data to 33 principal components (which together accounted for 90 % of variance). These principal components were z-scored and fed into the HSMM-MVPA. The HSMM-MVPA first applies a half-sine window function to increase the signal-to-noise ratio of the *bumps,* the cortical response to sub-cortical input. The bumps are assumed to be 50-millisecond modulations of amplitude at the onset of cognitive stages with the same topology across trials. The signals from the end of a bump to the next bump are assumed to have zero-mean amplitude, a *flat*. The duration of a given stage (bump + flat) is assumed to come from a gamma distribution with shape parameter equal to two. Consequently, a stage is modeled as a bump of a certain amplitude followed by a zero-mean amplitude flat and a duration given by a gamma-2 distribution. There is one exception and this is the first stage (pre-visual encoding here) which does not start with a bump. With this stage model and a predefined number of stages, the Baum-Welch algorithm for HSMMs searches the amplitude and location of bumps that explain the z-scored principal components best (61).

The bump amplitudes (for the 33 PCA components) are the same for all trials and vary across stages. The temporal location of the bumps also varies across trials, but the resulting stage durations are constrained to gamma-2 distributions with one scale parameter per stage.

We explored models with 3 to 7 cognitive stages as previous studies have shown that this memory task consists of 5 to 6 stages (4, 5, 16). For each model we ran the HSMM-MVPA 200 times with random initial parameters to avoid converging in local maxima. We used a leave-one-subject-out cross-validation to assess whether a model with *N+1* stages could explain the data significantly better (using a sign-test) than a model with *N* stages (16). The final model was the simplest one that generalized across subjects – a five-stage model. Then, we allowed one stage to have different gamma-scale parameters across experimental conditions, and we used leave-one-subject-out cross-validation to decide on the best model. As in previous studies (4, 16), a model with different gamma distributions in the retrieval stage explained the MEG data best.

4.4.4 Measuring neural coordination

To measure neural coordination – local synchrony and directed functional connectivity – we used the analytic signal of theta band oscillations. The parcellated MEG data were band pass filtered (cut-off frequencies: 3.8, and 8.5 Hz; forward-backward IIR Butterworth filter of order 4) and epoched from -0.4 seconds before the stimuli onset to 0.4 seconds after the response. Epochs were Hilbert transformed to the analytic signal using symmetric padding of 0.4 seconds to avoid edge artifacts.

4.4.5 Directed Functional Connectivity

Directed functional connectivity between regions *i* and *j* was measured with the directed phase-lag index (dpFC) (37) as follows:

$$dpFC^{ij} = \frac{1}{N}\sum_{n=1}^{N}\frac{1}{T_n}\sum_{t=s+1}^{s+T_n} sgn\left(\mathrm{Im}\left(S_{nt}^{ij}\right)\right) \qquad \text{Eq. 1}$$

In Eq. 1, $Im(S^{ij})$ is the imaginary part of the cross-spectral density, and *sgn* is the sign function. To compute within-stage dpFC, *s+1* was the first sample 0.05 seconds after the onset of the stage, *Tn* was the length of the stage in trial *n*, and *N* is the number of trials. Across-trials dpFC was computed sample-by-sample with *Tn* = 1 and time-locked to stage onset. Both within-stage and across-trial dpFC were later averaged across subjects. A detailed explanation can be found in the SI.

4.4.6 Generative whole-brain model

The generative whole-brain model (GWBM) was derived with the Ott-Antonsen ansatz (58) from a network-of-networks of Kuramoto oscillators (41). See (18) for a step-by-step derivation. The dynamics of synchrony in a region are given by the Kuramoto order parameter (KOP) which describes the dynamics of synchrony in in biological systems as well as a pool of neurons (59). The KOP is a complex number $\left(KOP = r\,e^{i\psi}\right)$ with the modulus bound by zero (asynchrony) and one (full synchrony). Here, the KOP simulated the analytic signal of the MEG data. Beforehand we set the natural frequencies of the oscillators to a Lorentzian distribution centered in the theta band (center, Ω: 6 Hz, spread, Δ: 1), and the spike-propagation velocity along the structural fibers to 5 m/s. The equations of the KOP in on region, i, of the GWBM are as follows:

$$\dot{r}_i = -\Delta_i r_i + \frac{L_i}{2}(1 - r_i^2) r_i + \frac{G}{2R}(1 - r_i^2) \sum_{j=1, j\neq i}^{R} A_{ij} r_j\left(t - \tau_{ij}\right) \cos\left(\psi_j\left(t - \tau_{ij}\right) - \psi_i\right) \qquad \text{Eq. 2}$$

$$\dot{\psi}_i = \Omega_i + \frac{G}{2R}\left(r_i + \frac{1}{r_i}\right) \sum_{j=1, j\neq i}^{R} A_{ij} r_j\left(t - \tau_{ij}\right) \sin\left(\psi_j\left(t - \tau_{ij}\right) - \psi_i\right) \qquad \text{Eq. 3}$$

The time dependency has been removed in variables without time delays; τ are the time delays between regions (fiber length x spike-propagation velocity); A is the coupling strength between regions (density of structural fibers); and R is the number of regions. To simulate resting state dynamics we explored parameters G (global scaling of structural connectivity) and L (local connectivity strength, same in all regions) with 25 randomly initialized models. The results of this exploration are shown in SI Figure 1. With G and L set to simulate resting-state, the thalamocortical inputs were simulated as 0.03 second increases/decreases of L at each region and stage onset independently. Simulated dpFC was measured with Eq. 1, but here N represented 25 models with different initial conditions and T_n was the median duration of the MEG stages. The initial conditions of the first stage were the MEG phases and amplitudes at the pre-encoding stage plus random noise. More details of the simulations are reported below.

4.4.7 Optimization of thalamocortical inputs

The generalized island model optimized ten islands in parallel that occasionally exchanged their best-fitted individuals. In the generalized island model an island is a metaphor for an evolutionary optimization algrithm that ocasionally exachanges information with other evolutionary optimization algorithms. Each island consisted of 50 individuals with a particular parametrization of a differential evolution algorithm. Their fitness function had three objectives that were combined into one index of fitness. The dominant objective was to maximize the similarity of simulated and empirical within-stage dpFC, f_1:

$$f_1 = \sum_{i=1}^{E} x_i \cdot y_i \left(\sum_{i=1}^{E} |x_i| \right)^{-1} \qquad \text{Eq. 4}$$

The links, E, in the empirical dpFC, x, were either 0 (not significant), 1 (lag-ahead) or -1 (lag-behind). Simulated dpFC links, y, were either -1 or 1. The objective f_1 gave discrete values which interval was used by the other two objectives. The second objective, f_2, maximized the topological similarity of the relative change in envelope amplitude at the onset of each stage. This similarity was measured with the Spearman rank-correlation between MEG and simulated relative amplitudes. The third objective, f_3, minimized the absolute size of the thalamic pulses as

$$f_3 = \frac{1}{L_{max}} \sum_{j=1}^{R} |L_j| \left(\sum_{i=1}^{E} |x_i| \right)^{-1} \qquad \text{Eq. 5}$$

where L_i are the local connectivities, and L_{max} is the largest absolute pulse allowed to the optimizers. The combined fitness index was $f = f_1 - (1-f_2)f_3$. The best individual had the minimal $(1-f_2)f_3$ among the 5000 individuals with the highest f in order to avoid a GWBM with low f_2 and f_3. The last simulated samples of this individual were used to initialize the simulations of the next stage (see SI).

4.4.8 Relevance of individual regions for switches

To assess the relevance of a region for switching between states of dpFC, a GWBM was lesioned by setting the thalamocortical pulse in this region to zero while the remaining regions were left untouched. Then, the fitness of the lesioned GWBM (Eq. 4) was compared to the fitness achieved by the original GWBM. The relevance of a region was measured as the number of within-stage dpFC links in the lesioned model that were not matching MEG data relative to the number of links matching MEG data in the full model. This process to measure relevance was repeated for the 68 regions in the GWBM and the four transitions between stages. To obtain a measure of relevance that was not dependent on a single GWBM, relevance was evaluated in 1,000 GWBMs randomly picked among the models in the top one percentile after optimization. Next, we used linear regions models with one independent variable to explain the relevance of regions. Each linear model included as dependent variable the relevance of the 68 regions and four stages in a lesioned GWBM. A linear model was fitted for each of the 1,000 lesioned models independently.

4.4.9 Generative whole-brain model: Resting-state

To identify a GWBM that simulated resting-state dynamics we performed a grid-search over the global and local coupling parameter space. The local couplings were assumed identical for all regions. Resting-state dynamics are characterized by temporal fluctuations of global and local synchrony, and time-resolved patterns of functional connectivity (i.e.

metastable dynamics). Metastability was measured as the standard deviation of the modulus of the KOP over time at local and global levels (76, 77). At local level the metastabilities were averaged across regions. To obtain the global KOP over time we averaged the phases of the local KOPs across regions (ψ in Equation 3 of the main text). To assess the temporal structure of the global metastability we computed the mean of the absolute values of its autocorrelation function. To avoid the influence of the initial conditions on the simulations we ran twenty-five GWBMs with random initial conditions for each combination of parameters. The simulations were run for 1000 seconds, but the initial 200 seconds were removed to discard initial transients. All simulations were performed with a time-delayed first-order Euler method and an integration step of 1 millisecond. We ended up with a global coupling of 0.15 and a local coupling of 0.7, which had the best trade-off between high metastability and low autocorrelation of global KOP, and therefore were chosen as the default values for the following GWBMsr. Figure S1 shows the grid-search results of resting-state dynamics.

4.4.10 Generative whole-brain model: cognitive task

To simulate the sequence of cognitive stages and their associated neural coordination patterns, we initialized 25 models informed by the theta-band phases and envelope amplitudes observed at the pre-encoding stage. The MEG envelopes were measured 0.1 and 0.05 seconds before the onset of the encoding stage. Then, the initial history of the KOP modulus was a straight line that joined the mean of these amplitudes across trials plus Gaussian noise (σ=0.01). To choose the initial history of phases we measured inter-trial phase consistency, and within-stage dpFC at the pre-encoding stage. There were 10 regions (mostly occipital and parietal) that showed significant inter-trial phase consistency. The initial history of phases at these regions were set to the average MEG phases across trials at 0.05 seconds before the onset of the first stage plus Gaussian noise (σ=0.01). The phases of these regions were used as a referent point for the remaining regions. The initial phases of the remaining regions were set by an optimization algorithm (CMAES (78)) which tried to establish a phase relationship between regions as in the empirical within-stage dpFC. The dpFC of the initial history of phases had an average similarity to empirical within-stage dpFC of 78%. To initialized the 25 GWBMs of the remaining stages, we used the last simulated samples in the best individual of the optimization process (see section *Methods: Optimization of thalamocortical inputs* in the main text).

The model with the best fitting sequence of parameters was left to run 400 seconds after the last stage. Figure S2 shows that the model neither remained trapped into the functional connectivity state of the last stage, nor did it return to any of the previous states (SI Fig. 2, bottom). Instead, the model returned to resting state: global and local synchrony, as well as functional connectivity fluctuated over time (metastable dynamics; SI Fig. 2, top & middle).

4.4.11 Optimization of thalamocortical inputs

To find the optimal thalamocortical inputs, we used the generalized island model for evolutionary optimization with 10 islands (49). Each island ran on a separate CPU. The islands had heterogeneous parameters and they were connected forming a ring. This configuration allowed for simultaneously exploring and exploiting multiple areas of the parameter space. The islands used the differential evolution algorithm DE1220 as implemented in the pagmo toolbox (79). The DE1220 algorithm incorporates self-adaptive heuristics for the mutation method and the parameters F (differential weight) and C (crossover probability) of the traditional differential evolution algorithm.

Table 1: Parameters of DE1220 algorithm on each island.

Island IDs	Mutation variants allowed	Adaptation scheme for F and C
1	best/1/exp; rand-to-best/1/exp; best/1/bin; rand-to-best/1/bin	jDE
2	rand-to-current/2/exp; rand-to-current/2/bin	jDE
3	rand-to-current/2/exp; rand-to-current/2/bin	iDE
4	best/1/exp; rand-to-best/1/exp; best/1/bin; rand-to-best/1/bin	iDE
5	rand/1/exp; rand/1/bin	jDE
6	rand-to-current/2/exp; rand-to-current/2/bin	jDE
7	rand-to-current/2/exp; rand-to-current/2/bin	iDE
8	best/1/exp; rand-to-best/1/exp; best/1/bin; rand-to-best/1/bin	jDE
9	best/1/exp; rand-to-best/1/exp; best/1/bin; rand-to-best/1/bin	iDE
10	rand/1/exp; rand/1/bin	jDE

The islands were connected in a ring following the order of Table 1. Figure S3 shows the parameters of the individuals and their fitness along the evolution in one island. This figure shows how the cost function could simultaneously maximize the fitness of within-stage dpFC and relative local synchrony at the onset (Spearman correlation), while the change in local coupling was minimized. The optimization of the four stages took approximately 4 days using 10 CPUs.

4.4.12 Structural connectivity, MRI acquisition and processing

We used 45 subjects from the test-retest dataset of the Human Connectome Project (HCP) 3T. This data set consisted of T1-weighted and multi-shell diffusion MRI data. T1-weighted data were acquired with 0.7 mm isotropic voxel size, TE = 2.14 ms, and TR = 2400 ms. Diffusion MRI data were acquired with a 1.25-mm isotropic voxel size, TE = 89.5 ms, and TR 5520 ms, with three shells with b = 1000, 2000, and 3000 s/mm^2, each shell with 90 diffusion weighted volumes and 6 non-weighted images (62). The diffusion MRI data was already preprocessed as described in (57). In short, diffusion MRI data were corrected for

head motion and geometrical distortions arising from eddy currents and susceptibility artifacts (63). Finally, the diffusion MRI images were aligned to the structural T1 image. The T1w image was parcellated using the Desikan–Killany parcellation (29), resulting in 68 cortical ROIs. Using the T1w image, the probability maps of the different tissues were obtained to create the five tissue-type files (64, 65).

Tractography was carried out with constrained spherical deconvolution (66, 67). A multi-tissue response function was calculated (68) and the average response functions were calculated. The multi-tissue fiber orientation distribution was calculated (69) with the average response function (L_{max} = 8). The fiber orientation distribution images had a joint bias field correction and a multi-tissue informed log-domain intensity normalization (70). Then, tractography was performed with the iFOD2 algorithm (71) using anatomically constrained tractography (72); generating 10 million streamlines (cutoff at 0.05, default); and using backtracking (72) and a dynamic seeding (73). The length of the fibers was set to a minimum of 20 mm and a maximum of 250 mm (72). To be able to quantitatively assess the connectivity, SIFT2 was applied to the resulting tractograms (73).

The connectivity matrix was built with a robust approach. In particular a 2-mm radial search at the end of the streamline was performed to allow the tracts to reach the gray matter parcellation (74). Each connectivity matrix was multiplied by its μ coefficient obtained from the SIFT2 process, as the sum of the streamline weights needs to be proportional to the units of fiber density for each subject (75). Connectivity matrices were averaged across subjects, and the 10% of links with the highest coefficient of variation across subjects were set to zero. Finally, the averaged and thresholded structural connectivity matrix was normalized to have an average value of one.

4.5 Supplementary Figures

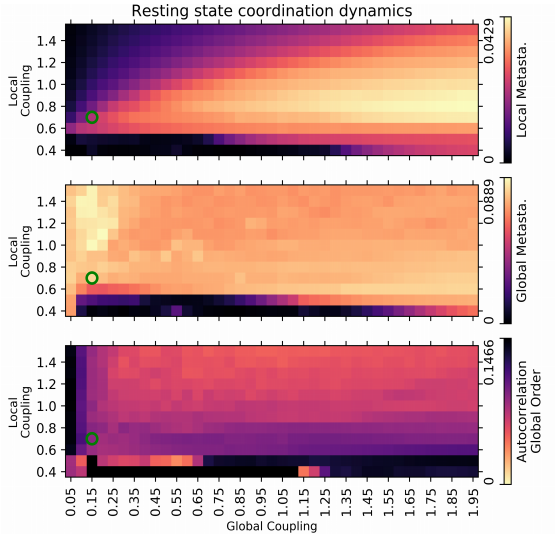

Figure S1. *Resting state neural coordination dynamics.* The green dot indicates the parametrization of the model. The location of the green dot was based on the idea that resting state dynamics should have simultaneously the lightest color in the three panels and the weakest coupling parameters.

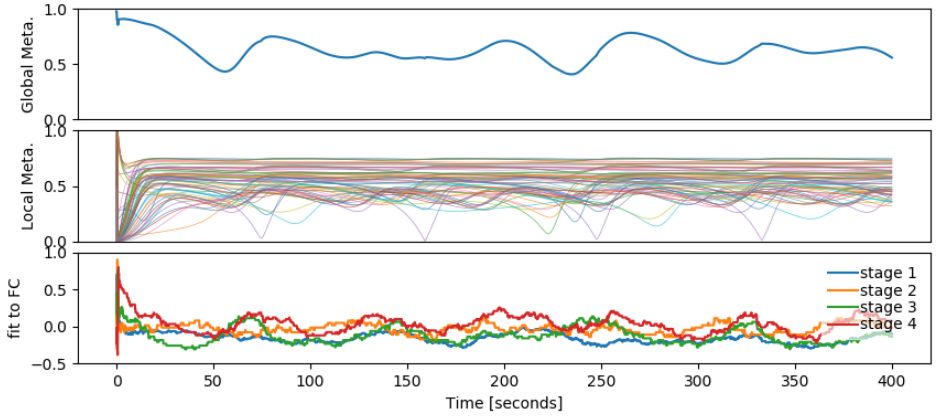

Figure S2. *Return to resting-state after cognitive stages. Top: Modulus of the global KOP. Middle: Modulus of the local KOP for the cortical 68 ROIs. Bottom: Temporal evolution of simulated-to-MEG fitness of within-stage dpFC for the four cognitive stages. This is similar to Figure 2B but for a much longer period of time. The MEG within-stage dpFC* of each stage (Fig. 1B) were compared (Eq. 4) with the simulated *dpFC* sample-by-sample (Eq. 1).

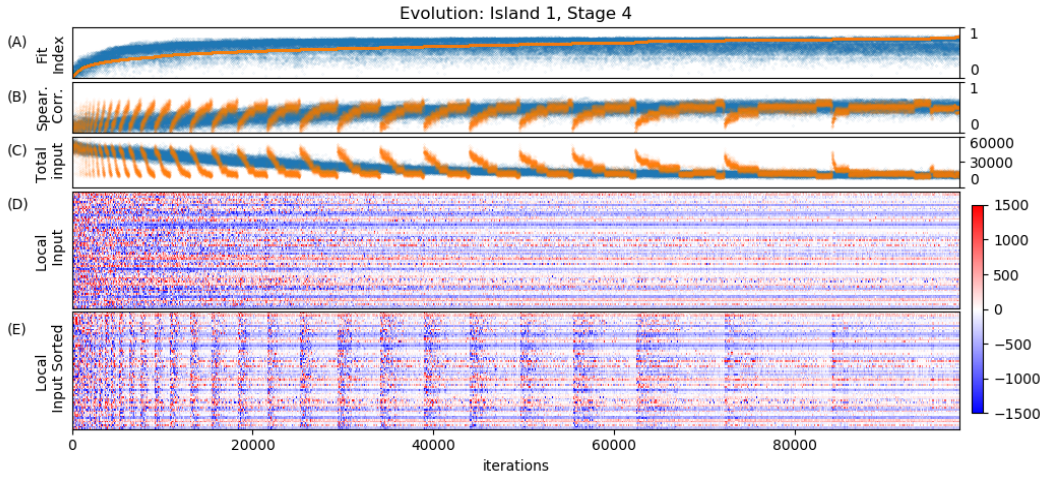

Figure S3. *Individuals and their fitness along the optimization in one island. (A) fitness index f. (B) Spearman correlation, objective f_1. (C) Sum of the absolute change in local coupling at the onset of the stage. Blue dots are the A, B and C values in the order that they were evaluated along the optimization process. Orange dots are the same values but sorted by the Fit Index (A). (D) Change in local coupling (thalamic input) at the onset that produces the blue dots in A, B, C. (E) Change in local coupling (thalamic input) at the onset that produces the orange dots in A, B, C.*

References

1. F. C. Donders, On the speed of mental processes. *Acta Psychol (Ams)* **30**, 412–431 (1969).
2. S. Sternberg, The discovery of processing stages: Extensions of Donders' method. *Acta Psychologica* **30**, 276–315 (1969).
3. J. P. Borst, A. S. Ghuman, J. R. Anderson, Tracking cognitive processing stages with MEG: A spatio-temporal model of associative recognition in the brain. *NeuroImage* **141**, 416–430 (2016).
4. O. Portoles, J. P. Borst, M. K. van Vugt, Characterizing synchrony patterns across cognitive task stages of associative recognition memory. *Eur J Neurosci* **48**, 2759–2769 (2018).
5. J. R. Anderson, *et al.*, The Common Time Course of Memory Processes Revealed. *Psychol Sci* **29**, 1463–1474 (2018).
6. A. Stocco, C. Lebiere, J. R. Anderson, Conditional routing of information to the cortex: A model of the basal ganglia's role in cognitive coordination. *Psychol Rev* **117**, 541–574 (2010).
7. R. C. O'Reilly, M. J. Frank, Making working memory work: a computational model of learning in the prefrontal cortex and basal ganglia. *Neural Comput* **18**, 283–328 (2006).
8. T. C. Stewart, T. Bekolay, C. Eliasmith, Learning to Select Actions with Spiking Neurons in the Basal Ganglia. *Front. Neurosci.* **6** (2012).
9. P. Redgrave, T. J. Prescott, K. Gurney, The basal ganglia: a vertebrate solution to the selection problem? *Neuroscience* **89**, 1009–1023 (1999).
10. K. Hwang, M. A. Bertolero, W. B. Liu, M. D'Esposito, The Human Thalamus Is an Integrative Hub for Functional Brain Networks. *J. Neurosci.* **37**, 5594–5607 (2017).
11. R. M. Bruno, B. Sakmann, Cortex Is Driven by Weak but Synchronously Active Thalamocortical Synapses. *Science* **312**, 1622–1627 (2006).
12. I. Rektor, *et al.*, Cognitive- and movement-related potentials recorded in the human basal ganglia. *Mov. Disord.* **20**, 562–568 (2005).
13. S. J. Cruikshank, T. J. Lewis, B. W. Connors, Synaptic basis for intense thalamocortical activation of feedforward inhibitory cells in neocortex. *Nat Neurosci* **10**, 462–468 (2007).
14. M. Malekmohammadi, W. J. Elias, N. Pouratian, Human thalamus regulates cortical activity via spatially specific and structurally constrained phase-amplitude coupling. *Cereb Cortex* **25**, 1618–1628 (2015).
15. Y. B. Saalmann, Intralaminar and medial thalamic influence on cortical synchrony, information transmission and cognition. *Front. Syst. Neurosci.* **8** (2014).
16. J. R. Anderson, Q. Zhang, J. P. Borst, M. M. Walsh, The discovery of processing stages: Extension of Sternberg's method. *Psychol Rev* **123**, 481–509 (2016).
17. P. Tewarie, *et al.*, Relationships Between Neuronal Oscillatory Amplitude and Dynamic Functional Connectivity. *Cerebral Cortex* **29**, 2668–2681 (2019).
18. O. Portoles, *et al.*, Modulations of local synchrony over time lead to resting-state functional connectivity in a parsimonious large-scale brain model. *bioRxiv*, 2021.01.20.427443 (2021).
19. H. S. Berberyan, L. van Maanen, H. van Rijn, J. Borst, EEG-based Identification of Evidence Accumulation Stages in Decision-Making. *J Cogn Neurosci* **33**, 510–527 (2020).
20. Q. Zhang, M. M. Walsh, J. R. Anderson, The Impact of Inserting an Additional Mental Process. *Comput Brain Behav* **1**, 22–35 (2018).
21. J. Cabral, M. L. Kringelbach, G. Deco, Functional connectivity dynamically evolves on multiple time-scales over a static structural connectome: Models and mechanisms. *NeuroImage* **160**, 84–96 (2017).
22. J. Cabral, *et al.*, Exploring mechanisms of spontaneous functional connectivity in MEG: How delayed network interactions lead to structured amplitude envelopes of band-pass filtered oscillations. *NeuroImage* **90**, 423–435 (2014).
23. E. Tognoli, J. A. S. Kelso, The Metastable Brain. *Neuron* **81**, 35–48 (2014).
24. L.-Z. Wang, *et al.*, A geometrical approach to control and controllability of nonlinear dynamical networks. *Nat Commun* **7**, 11323 (2016).
25. J. R. Anderson, *How can the human mind occur in the physical universe?* (Oxford University Press, 2007).
26. B. P. Staresina, M. Wimber, A Neural Chronometry of Memory Recall. *Trends Cogn Sci* **23**, 1071–1085 (2019).
27. A. Gramfort, *et al.*, MNE software for processing MEG and EEG data. *NeuroImage* **86**, 446–460 (2014).

28. B. Fischl, FreeSurfer. *NeuroImage* **62**, 774–781 (2012).

29. R. S. Desikan, *et al.*, An automated labeling system for subdividing the human cerebral cortex on MRI scans into gyral based regions of interest. *Neuroimage* **31**, 968–980 (2006).

30. J. F. Cavanagh, M. J. Frank, Frontal theta as a mechanism for cognitive control. *Trends Cogn Sci* **18**, 414–421 (2014).

31. P. Sauseng, B. Griesmayr, R. Freunberger, W. Klimesch, Control mechanisms in working memory: a possible function of EEG theta oscillations. *Neurosci Biobehav Rev* **34**, 1015–1022 (2010).

32. A. Rajan, *et al.*, Theta Oscillations Index Frontal Decision-Making and Mediate Reciprocal Frontal–Parietal Interactions in Willed Attention. *Cereb Cortex* **29**, 2832 (2019).

33. G. Pellegrino, L. Tomasevic, D. M. Herz, K. M. Larsen, H. R. Siebner, Theta Activity in the Left Dorsal Premotor Cortex During Action Re-Evaluation and Motor Reprogramming. *Front. Hum. Neurosci.* **12** (2018).

34. R. T. Canolty, *et al.*, High Gamma Power Is Phase-Locked to Theta Oscillations in Human Neocortex. *Science* **313**, 1626–1628 (2006).

35. B. Voloh, T. Womelsdorf, A Role of Phase-Resetting in Coordinating Large Scale Neural Networks During Attention and Goal-Directed Behavior. *Front. Syst. Neurosci.* **10** (2016).

36. N. A. Ketz, O. Jensen, R. C. O'Reilly, Thalamic pathways underlying prefrontal cortex-medial temporal lobe oscillatory interactions. *Trends Neurosci* **38**, 3–12 (2015).

37. C. J. Stam, E. C. W. van Straaten, Go with the flow: Use of a directed phase lag index (dPLI) to characterize patterns of phase relations in a large-scale model of brain dynamics. *NeuroImage* **62**, 1415–1428 (2012).

38. R. M. G. Reinhart, Working memory revived in older adults by synchronizing rhythmic brain circuits. *Nat Neurosci*, 16.

39. G. Hartwigsen, H. R. Siebner, Joint Contribution of Left Dorsal Premotor Cortex and Supramarginal Gyrus to Rapid Action Reprogramming. *Brain Stimul* **8**, 945–952 (2015).

40. J. P. Gallivan, C. S. Chapman, D. M. Wolpert, J. R. Flanagan, Decision-making in sensorimotor control. *Nat Rev Neurosci* **19**, 519–534 (2018).

41. P. S. Skardal, J. G. Restrepo, Hierarchical synchrony of phase oscillators in modular networks. *Phys. Rev. E* **85**, 016208 (2012).

42. M. Breakspear, S. Heitmann, A. Daffertshofer, Generative Models of Cortical Oscillations: Neurobiological Implications of the Kuramoto Model. *Front. Hum. Neurosci.* **4** (2010).

43. Y. L. Maistrenko, B. Lysyansky, C. Hauptmann, O. Burylko, P. A. Tass, Multistability in the Kuramoto model with synaptic plasticity. *Phys. Rev. E* **75**, 066207 (2007).

44. G. Deco, *et al.*, Single or multiple frequency generators in on-going brain activity: A mechanistic whole-brain model of empirical MEG data. *NeuroImage* **152**, 538–550 (2017).

45. Y. B. Saalmann, M. A. Pinsk, L. Wang, X. Li, S. Kastner, The Pulvinar Regulates Information Transmission Between Cortical Areas Based on Attention Demands. *Science* **337**, 753–756 (2012).

46. S. M. Sherman, The thalamus is more than just a relay. *Curr Opin Neurobiol* **17**, 417–422 (2007).

47. E. J. Ramcharan, J. W. Gnadt, S. M. Sherman, Higher-order thalamic relays burst more than first-order relays. *Proc. Natl. Acad. Sci. U.S.A.* **102**, 12236–12241 (2005).

48. M. Kloc, A. Maffei, Target-Specific Properties of Thalamocortical Synapses onto Layer 4 of Mouse Primary Visual Cortex. *J Neurosci* **34**, 15455–15465 (2014).

49. D. Izzo, M. Ruciński, F. Biscani, The Generalized Island Model. *Parallel Architectures and Bioinspired Algorithms*, 151–169 (2012).

50. T. E. J. Behrens, *et al.*, Non-invasive mapping of connections between human thalamus and cortex using diffusion imaging. *Nat Neurosci* **6**, 750–757 (2003).

51. Y. Qin, Y. Kawano, O. Portoles, M. Cao, Partial Phase Cohesiveness in Networks of Networks of Kuramoto Oscillators. *IEEE Trans Automat Contr*, 1–1 (2021).

52. V. Nicosia, M. Valencia, M. Chavez, A. Díaz-Guilera, V. Latora, Remote Synchronization Reveals Network Symmetries and Functional Modules. *Phys. Rev. Lett.* **110**, 174102 (2013).

53. S. Petkoski, *et al.*, Heterogeneity of time delays determines synchronization of coupled oscillators. *Phys. Rev. E* **94**, 012209 (2016).

54. R. Vicente, L. L. Gollo, C. R. Mirasso, I. Fischer, G. Pipa, Dynamical relaying can yield zero time lag neuronal synchrony despite long conduction delays. *Proc. Natl. Acad. Sci. U.S.A.* **105**, 17157–17162 (2008).

55. M. Halgren, *et al.*, The generation and propagation of the human alpha rhythm. *Proc. Natl. Acad. Sci. U.S.A.* **116**, 23772–23782 (2019).

56. M. K. van Vugt, P. Simen, L. Nystrom, P. Holmes, J. D. Cohen, Correction: Lateralized Readiness Potentials Reveal Properties of a Neural Mechanism for Implementing a Decision Threshold. *PLoS One* **10**, e0132197 (2015).

57. M. F. Glasser, *et al.*, The minimal preprocessing pipelines for the Human Connectome Project. *Neuroimage* **80**, 105–124 (2013).

58. E. Ott, T. M. Antonsen, Low dimensional behavior of large systems of globally coupled oscillators. *Chaos* **18**, 037113 (2008).

59. E. Montbrió, D. Pazó, A. Roxin, Macroscopic Description for Networks of Spiking Neurons. *Phys. Rev. X* **5**, 021028 (2015).

60. R. Oostenveld, P. Fries, E. Maris, J.-M. Schoffelen, FieldTrip: Open Source Software for Advanced Analysis of MEG, EEG, and Invasive Electrophysiological Data. *Computational Intelligence and Neuroscience* **2011**, e156869 (2010).

61. S.-Z. Yu, Hidden semi-Markov models. *Artificial Intelligence*, 29 (2010).

62. D. C. Van Essen, *et al.*, The Human Connectome Project: a data acquisition perspective. *Neuroimage* **62**, 2222–2231 (2012).

63. S. N. Sotiropoulos, *et al.*, Advances in diffusion MRI acquisition and processing in the Human Connectome Project. *Neuroimage* **80**, 125–143 (2013).

64. Y. Zhang, M. Brady, S. Smith, Segmentation of brain MR images through a hidden Markov random field model and the expectation-maximization algorithm. *IEEE Trans Med Imaging* **20**, 45–57 (2001).

65. B. Patenaude, S. M. Smith, D. N. Kennedy, M. Jenkinson, A Bayesian model of shape and appearance for subcortical brain segmentation. *Neuroimage* **56**, 907–922 (2011).

66. J.-D. Tournier, F. Calamante, A. Connelly, Robust determination of the fibre orientation distribution in diffusion MRI: Non-negativity constrained super-resolved spherical deconvolution. *NeuroImage* **35**, 1459–1472 (2007).

67. J.-D. Tournier, *et al.*, MRtrix3: A fast, flexible and open software framework for medical image processing and visualisation. *Neuroimage* **202**, 116137 (2019).

68. T. Dhollander, D. Raffelt, A. Connelly, Unsupervised 3-tissue response function estimation from single-shell or multi-shell diffusion MR data without a co-registered T1 image in (2016).

69. B. Jeurissen, J.-D. Tournier, T. Dhollander, A. Connelly, J. Sijbers, Multi-tissue constrained spherical deconvolution for improved analysis of multi-shell diffusion MRI data. *Neuroimage* **103**, 411–426 (2014).

70. D. Raffelt, *et al.*, Bias Field Correction and Intensity Normalisation for Quantitative Analysis of Apparent Fibre Density in (2017).

71. J.-D. Tournier, F. Calamante, A. Connelly, Improved probabilistic streamlines tractography by 2 nd order integration over fibre orientation distributions (2009) (February 10, 2021).

72. R. E. Smith, J.-D. Tournier, F. Calamante, A. Connelly, Anatomically-constrained tractography: improved diffusion MRI streamlines tractography through effective use of anatomical information. *Neuroimage* **62**, 1924–1938 (2012).

73. R. E. Smith, J.-D. Tournier, F. Calamante, A. Connelly, SIFT2: Enabling dense quantitative assessment of brain white matter connectivity using streamlines tractography. *Neuroimage* **119**, 338–351 (2015).

74. R. E. Smith, J.-D. Tournier, F. Calamante, A. Connelly, The effects of SIFT on the reproducibility and biological accuracy of the structural connectome. *Neuroimage* **104**, 253–265 (2015).

75. R. Smith, D. Raffelt, J.-D. Tournier, A. Connelly, Quantitative streamlines tractography: methods and inter-subject normalisation (2020) https:/doi.org/10.31219/osf.io/c67kn (February 10, 2021).

76. M. Wildie, M. Shanahan, Metastability and chimera states in modular delay and pulse-coupled oscillator networks. *Chaos* **22**, 043131 (2012).

77. J. Cabral, *et al.*, Exploring mechanisms of spontaneous functional connectivity in MEG: how delayed network interactions lead to structured amplitude envelopes of band-pass filtered oscillations. *Neuroimage* **90**, 423–435 (2014).

78. N. Hansen, The CMA Evolution Strategy: A Comparing Review. 28.

79. F. Biscani, D. Izzo, A parallel global multiobjective framework for optimization: pagmo. *Journal of Open Source Software* **5**, 2338 (2020).

5 Conclusion & Outlook

5.1 Conclusion

This thesis focused on the dynamics of macroscopic neural coordination across the different cognitive stages of an associative memory recognition task. Specifically, I have sought to understand the association between the fundamental cognitive stages that are required to perform the task and the dynamics of neural coordination. To this end, I have used a twofold approach. On the one hand, a novel approach for the analysis of M/EEG data was used to unveil patterns of local and cortex-wide neural coordination that evolve along with the fundamental cognitive stages. This data analysis approach corroborated several hypotheses whose confirmation could not be established on the basis of traditional data analysis methods. On the other hand, a generative whole-brain model of macroscopic neural synchrony (GWBM) was developed to test *in silico* the neural mechanisms that produce the switches between empirical states of local and cortex-wide coordination at the onset of cognitive stages. The development of such a GWBM enables overcoming several limitations that have hampered the application of GWBMs to cognitive tasks. To validate the capability of the proposed GWBM to simulate the temporal dynamics of neural coordination, I resorted to neuroimaging data from resting state activity – the field in which GWBMs have been a valuable tool to date. Once the GWBM proved its ability to capture the phenomena of interest in resting state data, the GWBM was applied to model the neural coordination along the time course of the associative recognition task.

The **second chapter** of this thesis provided the first evidence of changes in local and cortex-wide neural coordination with each of the fundamental cognitive stages required to perform an associative recognition task. These changes happen in several frequency bands, in particular the theta and alpha bands. Specifically, these changes are observed in the local power, the inter-trial coherence of the phase of neural oscillations, and the phase-lag relationship between pairs of cortical areas. These results motivated the following chapters of this thesis. However, the temporal resolution of the analysis was not high enough to corroborate the hypothesis that a new state of neural coordination is established just at the onset of a cognitive stage [1,2]. Additionally, the EEG montage had low spatial resolution. Both limitations were overcome later in **Chapter 4** with an MEG data set of the same task and a novel analysis of neural coordination that provides high temporal resolution around the onset of cognitive stages. The MEG analysis showed that, as had been hypothesized [1,2], there were modulations of neural coordination across the cortex at the very onset of cognitive stages. These modulations were initially short and local – a transient change in the amplitude of the envelope of the theta-band analytic signal. Such local modulations represent changes in the local synchrony of neural activity. After the local change there was a switch between states of cortex-wide coordination – directed functional connectivity. Each state of directed functional connectivity lasted throughout a cognitive stage. A state of directed functional connectivity consist of significant phase-lag relationships between pairs

of cortical regions. This observation confirmed the hypothesis that local modulations of the theta-band phase synchrony mark a change in cortex-wide functional connectivity [3].

Chapter 3 showed that the GWBM developed in the same chapter, and extended in **Chapter 4**, is able to simulate the static and time-resolved functional connectivity (between-region co-modulation of the envelope of the analytic signals in the alpha band) observed during resting state. The similarity between simulated and empirical activity was similar or superior to state-of-the-art GWBMs. It was crucial to first demonstrate that the proposed GWBM was able to simulate patterns of resting-state activity as these models have been applied mostly to resting-state data. Furthermore, the results of **Chapter 3** indicated that the time-resolved functional connectivity results from three factors. First, interaction delays between nodes (cortical regions) due to spike-propagation velocity. Second, a balance between a tendency to desynchronize neural activity locally and a tendency to synchronize neural activity between cortical regions. Third, a different level of local connectivity strength within each cortical region, which was mediated by the anatomical coupling between cortical regions, affected not only the local synchrony within that same region but also the local synchrony in other regions and the patterns of functional connectivity. In general, regions with low local connectivity strength showed a tendency to engage in functional connectivity with other regions, while regions with high local connectivity strength were independent of, but can influence, other regions. Interestingly, some regions of the default mode network showed an inverse pattern – they had high local connectivity strength, and engaged in functional connectivity with other regions.

In addition, the results of **Chapter 3** showed that empirical functional connectivity emerges at a working point at which global and local metastabilities (the temporal variability of synchrony) are maximal at the same time. Interestingly, GWBMs with different configurations of local connectivity strengths may have different levels of local metastability, but similar global dynamics – global metastability, across-region averaged local metastability, and functional connectivity. This suggests that the brain has enough flexibility to be able to reach the same cortex-wide state of coordination from different local states of coordination.

The results of **Chapter 3** supported previous findings such as the relevance of time delays between regions for generating the observed patterns of functional connectivity [4,5], as well as the fact that resting-state functional connectivity emerges when global synchrony is highly metastable [4,6,7]. However, unlike previous studies, **Chapter 3** highlighted the importance of local metastability for emerging resting-state functional connectivity because functional connectivity was more similar to empirical data when metastability was simultaneously high at local and global scales. State-of-the-art GWMBs are not able to model modulations of local synchrony [8,9]. Thus, local metastability has been neglected, although metastability has been observed at multiple spatial scales [7]. Moreover,

modulations of local synchrony are observed in measurements of neural activity during cognitive tasks, but state-of-the-art GWBMs cannot capture such phenomena [9]. This was one of the reasons for developing a GWBM that captures modulations of local synchrony. The proposed GWBM treats local and global synchrony in the same manner while taking into account the most relevant differences. Other GWBMs have used a similar mathematical formulation – a network-of-networks of Kuramoto oscillators. However, in **Chapter 3** a mean field reduction over the subnetworks was applied for two reasons. One reason was to reduce the computational cost of simulations which made it feasible to optimize the parameters of local dynamics in a reasonable amount of time. The second reason was to avoid finite-size effects which affect the dynamics of the GWBMs and the simulations of resting-state functional connectivity [10].

Chapter 4 extended the GWBM proposed in **Chapter 3** to model the dynamics of neural coordination along the time course of a cognitive task. The measurements of cortical activity in **Chapter 4** showed that the transition to a new state of cortical coordination starts at the onset of a cognitive stage with a short modulation of local synchrony followed by a cortex-wide switch between states of directed functional connectivity. The GWBM aims at modeling both phenomena – the modulations of local synchrony as well as the switches between states of directed functional connectivity.

To explain how these changes in neural coordination are carried out, the GWBM of **Chapter 3** was extended to include the mechanisms that are thought to modulate cortical activity at the onset of cognitive stages. The GWBM in **Chapter 4** was extended in a parsimonious way to mimic bursts of thalamocortical activity that targeted either excitatory or inhibitory synapses at the onset of cognitive stages as the literature suggest [1,11–15]. These bursts were implemented as short modulations of local connectivity strength [16]. This GWBM was able to simulate with high accuracy the empirically observed changes in local synchrony at the onset of cognitive stages as well as the switches between states of directed functional connectivity observed in MEG data. These results indicate that such a mechanism – short modulations of local connectivity strength that could be due to thalamocortical bursts of activity – is enough to control the dynamics of cortex-wide coordination that appear during a cognitive task. These results support the hypothesis that the thalamus coordinates cortical activity at the onset of cognitive stages [1], as well as the hypothesis that local modulations of synchrony in the theta band mark the onset of new states of functional connectivity to enable a sequence of different cognitive functions [3].

Furthermore, **Chapter 4** explored the importance of individual regions for switching between the observed states of directed functional coordination. The importance of a region was determined by the interaction between the amount of change in the local connectivity

strength and the total strength of the anatomical connectivity with other regions. Therefore, a switch between states of directed functional connectivity depends not only on the bursts of thalamocortical activity that modulate local connectivity strength, but also on the anatomical topology that connects cortical regions. It is important to notice that the degree of functional connectivity of a region with other regions was not an indicator of the importance of the same region to set such state of functional connectivity. There were regions that were not functionally connected with other regions, but that were very important for reaching a state of directed functional connectivity. One example of this occurred during motor response in the left superior frontal region which has been related to cognitive control, attention, and decision making [17,18].

To derive the GWBM proposed in this thesis, several simplifying assumptions were made. Nevertheless the GWBM kept the most relevant properties of neural anatomy and dynamics. These assumptions simplified the equations and reduced the number of parameters so that the GWBM could be simulated and the parameters optimized in a reasonable amount of time. Several optimization algorithms were explored in **Chapter 3**. The best performance was obtained by Particle Swarm Optimization [19] and Differential Evolution [20]. The optimization of parameters in **Chapter 4** was carried out with the generalized island model for evolutionary optimization [21], and various flavors of the Differential Evolution algorithm. This optimization framework allowed for exploiting the benefits of parallel computing not only to speed up the computations but also to combine the results of simultaneously exploring and exploiting large areas of the parameter space.

5.2 Outlook

The findings and methods developed in this thesis pave the way for studying the dynamics of neural coordination during cognitive tasks, as well as the mechanisms that produce such dynamics of neural coordination. The outlook resulting from this thesis can be divided into two parts. One part is related to the methods to measure task-related activity. The other part is related to large-scale coordination with GWBMs.

The methods used to measure cortex-wide neural coordination result in a temporal resolution unprecedented for cognitive tasks. These methods will allow for deciphering which cortical regions coordinate their activity and when they do it, in relation to the elementary cognitive stages. This might contribute to further developing the theory of human cognition. Furthermore, this thesis has left unexplored the differences in neural coordination between task manipulations at a cognitive stage. Differences between task manipulations are at the core of experimental cognitive neuroscience. Therefore the results of this thesis are just the tip of the iceberg. In particular, one would expect differences in fronto-temporal functional connectivity between target and foil conditions during the memory retrieval stage [22,23]; differences in occipito-temporal connectivity and local

synchrony between word-length conditions during visual encoding; and differences between fan 1 and fan 2 words in several stages [24].

Furthermore, one could build upon the results of **Chapter 4** to disentangle two views on the cognitive functions of the motor response stage in tasks that require a decision-making stage. Both views acknowledge the presence of a decision-making stage prior to the motor response stage. However, one view says that the motor response stage is responsible only for executing a motor command, while the other view says that the decision is re-evaluated alongside the motor response [25]. In addition to executing the motor command, the motor response stage in the latter view involves other cognitive functions such as cognitive control and decision reevaluation [25,26]. The results of **Chapter 4** provide some evidence for the second view because there are traces of decision-making functional connectivity during the motor response stage, although a further experiment should be carried out to verify these results. Another issue highlighted by the results of **Chapter 4** refers to the systematic blurring of task-related neural activity introduced by traditional metrics of task-related activity as described in the introduction of this thesis (see Chapter 1, Figure 1). **Chapter 4** showed that local synchrony and the networks of directed functional connectivity change at a fast rhythm with sharp transitions between consecutive states of directed functional connectivity. Moreover, there were marked differences in the averaged strength of directed functional connectivity between stages. A traditional analysis would have merged functionally distinct networks of functional connectivity into a single metric. As a result, this metric would be dominated by the stronger connections or the connections with better temporal alignment across trials to the time-locking point, which might introduce an unwanted bias. This bias might distort the metrics related to the cognitive function of interest for the study. Therefore, the data of previous studies could be re-analyzed with the proposed method to avoid misinterpretations.

The GWBM developed in this thesis along with the optimization approach make it feasible to test *in silico* the mechanisms that generate the patterns of neural activity observed during resting state and cognitive tasks. In addition, the GWBM can be combined with the measurements of neural activity at specific cognitive stages to uncover the mechanisms by which neural stimulation methods, such as alternating current stimulation, affect neural dynamics and behavior. GWBMs are in their infancy, but there are promising use-cases in neuroscience and clinics. An example is the development of tools such as The Virtual Brain [27] and The Virtual Epileptic Patient [28]. In addition to being a valuable tool to understand neural dynamics, GWBMs have great potential to assist in the treatment of neurological conditions with personalized models of neural activity. These models would help to understand the effects of a local intervention or neurological treatment not only at local level but also at whole-brain level.

To easily build on the results of this thesis, further work could address the simplifying assumptions that were made to derive our GWBM. It is precisely these assumptions which open the door to plenty of possibilities to further investigate neural dynamics. For example, in the GWBMs of **Chapters 3 and 4**, it was assumed that the distribution of natural frequencies and the network topology within a region are identical for all regions. However, there is evidence that the power peak within a frequency band differs between regions [29]. Heterogeneous natural frequencies across regions will hinder global synchronization in a way similar to the time delays between regions. In addition, the dynamics of the GWBM might be affected by the relationship between the natural frequencies and the topology of the structural connectivity network. Manipulations of the network topology within regions affects the dynamics of the GWBM [30], and this can be used to model neurological disorders or the heterogeneity of cortical tissues [31,32]. Another simplifying assumption related to the GWBM in **Chapter 4** is the model of the thalamocortical signals that modulate cortical activity. Instead of pulses with the same temporal structure for all regions, the GWBM could be extended to account for the different temporal dynamics observed in the synapses targeted by thalamocortical signals [33].

In general, this thesis opens the door to understanding the mechanisms that lead to the dynamics of neural coordination observed throughout a task. Moreover, the thesis provides a method to uncover the dynamics of whole-brain neural coordination with high temporal resolution which will allow for understanding the relationship between neural coordination and each of the elementary cognitive processed involved in a task. Altogether, this thesis makes it possible to understand the roles of local and global neural dynamics as well as neural anatomy for achieving the states of neural coordination associated with specific cognitive functions and ultimately behavior.

References

1. Stocco A, Lebiere C, Anderson JR. Conditional routing of information to the cortex: A model of the basal ganglia's role in cognitive coordination. Psychol Rev. 2010;117: 541–574. doi:10.1037/a0019077
2. O'Reilly RC, Frank MJ. Making working memory work: a computational model of learning in the prefrontal cortex and basal ganglia. Neural Comput. 2006;18: 283–328. doi:10.1162/089976606775093909
3. Voloh B, Womelsdorf T. A Role of Phase-Resetting in Coordinating Large Scale Neural Networks During Attention and Goal-Directed Behavior. Front Syst Neurosci. 2016;10. doi:10.3389/fnsys.2016.00018
4. Cabral J, Luckhoo H, Woolrich M, Joensson M, Mohseni H, Baker A, et al. Exploring mechanisms of spontaneous functional connectivity in MEG: How delayed network interactions lead to structured amplitude envelopes of band-pass filtered oscillations. NeuroImage. 2014;90: 423–435. doi:10.1016/j.neuroimage.2013.11.047
5. Deco G, Jirsa V, McIntosh AR, Sporns O, Kötter R. Key role of coupling, delay, and noise in resting brain fluctuations. PNAS. 2009;106: 10302–10307. doi:10.1073/pnas.0901831106
6. Deco G, Kringelbach ML, Jirsa VK, Ritter P. The dynamics of resting fluctuations in the brain: metastability and its dynamical cortical core. Sci Rep. 2017;7: 3095. doi:10.1038/s41598-017-03073-5
7. Tognoli E, Kelso JAS. The Metastable Brain. Neuron. 2014;81: 35–48. doi:10.1016/j.neuron.2013.12.022
8. Coombes S, Byrne Á. Next generation neural mass models. arXiv:160706251 [q-bio]. 2016 [cited 9 Jul 2019]. Available: http://arxiv.org/abs/1607.06251
9. Byrne Á, Brookes MJ, Coombes S. A mean field model for movement induced changes in the beta rhythm. J Comput Neurosci. 2017;43: 143–158. doi:10.1007/s10827-017-0655-7
10. Peter F, Pikovsky A. Transition to collective oscillations in finite Kuramoto ensembles. Phys Rev E. 2018;97: 032310. doi:10.1103/PhysRevE.97.032310
11. Stewart TC, Bekolay T, Eliasmith C. Learning to Select Actions with Spiking Neurons in the Basal Ganglia. Front Neurosci. 2012;6. doi:10.3389/fnins.2012.00002
12. Saalmann YB, Pinsk MA, Wang L, Li X, Kastner S. The Pulvinar Regulates Information Transmission Between Cortical Areas Based on Attention Demands. Science. 2012;337: 753–756. doi:10.1126/science.1223082
13. Sherman SM. The thalamus is more than just a relay. Curr Opin Neurobiol. 2007;17: 417–422. doi:10.1016/j.conb.2007.07.003
14. Ramcharan EJ, Gnadt JW, Sherman SM. Higher-order thalamic relays burst more than first-order relays. Proc Natl Acad Sci USA. 2005;102: 12236–12241. doi:10.1073/pnas.0502843102
15. Kloc M, Maffei A. Target-Specific Properties of Thalamocortical Synapses onto Layer 4 of Mouse Primary Visual Cortex. J Neurosci. 2014;34: 15455–15465. doi:10.1523/JNEUROSCI.2595-14.2014
16. Maistrenko YL, Lysyansky B, Hauptmann C, Burylko O, Tass PA. Multistability in the Kuramoto model with synaptic plasticity. Phys Rev E. 2007;75: 066207. doi:10.1103/PhysRevE.75.066207
17. Cavanagh JF, Frank MJ. Frontal theta as a mechanism for cognitive control. Trends Cogn Sci. 2014;18: 414–421. doi:10.1016/j.tics.2014.04.012
18. Rajan A, Siegel SN, Liu Y, Bengson J, Mangun GR, Ding M. Theta Oscillations Index Frontal Decision-Making and Mediate Reciprocal Frontal–Parietal Interactions in Willed Attention. Cereb Cortex. 2019;29: 2832. doi:10.1093/cercor/bhy149
19. Marini F, Walczak B. Particle swarm optimization (PSO). A tutorial. Chemometrics and Intelligent Laboratory Systems. 2015;149: 153–165. doi:10.1016/j.chemolab.2015.08.020
20. Price K, Storn RM, Lampinen JA. Differential Evolution: A Practical Approach to Global Optimization. Berlin Heidelberg: Springer-Verlag; 2005. Available: https://www.springer.com/gp/book/9783540209508
21. Izzo D, Ruciński M, Biscani F. The Generalized Island Model. Parallel Architectures and Bioinspired Algorithms. 2012; 151–169. doi:10.1007/978-3-642-28789-3_7
22. Staresina BP, Wimber M. A Neural Chronometry of Memory Recall. Trends Cogn Sci. 2019;23: 1071–1085. doi:10.1016/j.tics.2019.09.011
23. Reinhart RMG, Nguyen JA. Working memory revived in older adults by synchronizing rhythmic brain circuits. Nat Neurosci. 2019;22: 820–827. doi:10.1038/s41593-019-0371-x

24. Borst JP, Ghuman AS, Anderson JR. Tracking cognitive processing stages with MEG: A spatio-temporal model of associative recognition in the brain. NeuroImage. 2016;141: 416–430. doi:10.1016/j.neuroimage.2016.08.002

25. Spieser L, Servant M, Hasbroucq T, Burle B. Beyond decision! Motor contribution to speed–accuracy trade-off in decision-making. Psychon Bull Rev. 2017;24: 950–956. doi:10.3758/s13423-016-1172-9

26. van Vugt MK, Simen P, Nystrom L, Holmes P, Cohen JD. Correction: Lateralized Readiness Potentials Reveal Properties of a Neural Mechanism for Implementing a Decision Threshold. PLoS One. 2015;10: e0132197. doi:10.1371/journal.pone.0132197

27. Sanz Leon P, Knock SA, Woodman MM, Domide L, Mersmann J, McIntosh AR, et al. The Virtual Brain: a simulator of primate brain network dynamics. Front Neuroinform. 2013;7: 10. doi:10.3389/fninf.2013.00010

28. Jirsa VK, Proix T, Perdikis D, Woodman MM, Wang H, Gonzalez-Martinez J, et al. The Virtual Epileptic Patient: Individualized whole-brain models of epilepsy spread. Neuroimage. 2017;145: 377–388. doi:10.1016/j.neuroimage.2016.04.049

29. Haegens S, Cousijn H, Wallis G, Harrison PJ, Nobre AC. Inter- and intra-individual variability in alpha peak frequency. Neuroimage. 2014;92: 46–55. doi:10.1016/j.neuroimage.2014.01.049

30. Skardal PS, Restrepo JG. Synchronization of Kuramoto oscillators in networks of networks. arXiv:12063822 [math, nlin]. 2012 [cited 9 Jul 2019]. Available: http://arxiv.org/abs/1206.3822

31. Demirtaş M, Burt JB, Helmer M, Ji JL, Adkinson BD, Glasser MF, et al. Hierarchical Heterogeneity across Human Cortex Shapes Large-Scale Neural Dynamics. Neuron. 2019;101: 1181-1194.e13. doi:10.1016/j.neuron.2019.01.017

32. Aerts H, Schirner M, Jeurissen B, Van Roost D, Achten E, Ritter P, et al. Modeling Brain Dynamics in Brain Tumor Patients Using the Virtual Brain. eNeuro. 2018;5. doi:10.1523/ENEURO.0083-18.2018

33. Cruikshank SJ, Lewis TJ, Connors BW. Synaptic basis for intense thalamocortical activation of feedforward inhibitory cells in neocortex. Nat Neurosci. 2007;10: 462–468. doi:10.1038/nn1861

Summary

This thesis investigated how patterns of neural synchrony emerge and dissolve alongside each of the elementary cognitive stages that are thought to constitute the building blocks of cognition and behavior. In particular, the neural activity from an associative memory recognition task was recorded noninvasively at a macroscopic scale with electroencephalography and magnetoencephalography

First, neural data was parsed into elementary cognitive stages with a method based on a machine-learning technique. This technique takes into consideration the variable duration of cognitive stages and across-trial consistencies in neural activity in order to identify the transition between elementary cognitive stages in a trial by trial basis. Next, local and cortex-wide neural coordination were measured with high temporal resolution within each cognitive stage and at the transitions between cognitive stages. This analysis revealed the existence of a switch between states of neural coordination at the transition between cognitive stages. The switch began with a local modulation of coordination and was followed by a change in cortex-wide coordination between pairs of brain regions. The new state of coordination lasted until the end of a cognitive stage. These results support two hypotheses that had not been confirmed due to limitations of traditional data analysis methods. These hypotheses stated that cortical activity is modulated at the onset of cognitive stages, and that local changes in synchrony mark the onset of changes in between-region synchrony to implement a cognitive function.

In addition to reporting neural measurements, this thesis developed a generative whole-brain model of macroscopic neural activity that accounts for the dynamics of macroscopic cortical synchrony, neural anatomy, and sub-cortical signals. This model allowed for testing *in silico* the mechanisms that generate the patterns of neural activity observed empirically. First the model was used to explain time-resolved neural synchrony during the resting state, as this has been the primary application domain of these models so far. The model was able to simulate resting-state time-resolved cortex-wide neural synchrony with high accuracy, and revealed the importance of local modulations of synchrony and heterogeneous local connectivity strengths to generate resting-state neural synchrony.

In the following chapter, the model was extended to include the sub-cortical signals that are thought to modulate cortical activity at the onset of cognitive stages. With this extension, the model was additionally able to simulate the patterns of local and cortex-wide synchrony measured during the associative recognition memory task. The model showed that short bursts of thalamocortical activity targeted at either excitatory or inhibitory local cortical synapses were sufficient to cause the switch between states of cortical synchrony measured at each cognitive stage. Furthermore, the model quantified the importance of individual

regions for producing each of the switches. The importance of a region was partly explained by the interaction between the magnitude of the incoming thalamocortical burst of activity and its anatomical connectivity with other regions.

The whole-brain model proposed in this thesis is the first one to allow for simulating the neural synchrony alongside each of the elementary cognitive stages in a task. Additionally, the method to measure neural synchrony provides unprecedented temporal resolutions at individual cognitive stages. Taken together, this thesis paves the way for understanding the states of neural synchrony associated with elementary cognitive stages in a task as well as the mechanisms needed to reach such states neural synchrony.